Micro-structures for morphology guiding and signal recording of neuronal cells: towards an integrated platform

Henrique Teixeira

Mestrado Integrado em Engenharia Física

Departamento de Física e Astronomia

2019

Orientador

Prof. Dr. João Ventura, Faculdade de Ciências

Coorientador

Prof. Dr. Paulo Aguiar, i3S

U.PORTO

FACULDADE DE CIÊNCIAS
UNIVERSIDADE DO PORTO

Todas as correções determinadas pelo júri, e só essas, foram efetuadas.

O Presidente do Júri,

Porto, _____/_____/_____

UNIVERSIDADE DO PORTO

MASTERS THESIS

Micro-structures for morphology guiding and signal recording of neuronal cells: towards an integrated platform

Author:
Henrique TEIXEIRA

Supervisor:
João VENTURA

Co-supervisor:
Paulo AGUIAR

A thesis submitted in fulfilment of the requirements
for the degree of MSc. Engineering Physics

at the

Faculdade de Ciências da Universidade do Porto
Departamento de Física e Astronomia

December 19, 2019

" So remember to look up at the stars and not down at your feet. Try to make sense of what you see and wonder about what makes the universe exist. Be curious. And however difficult life may seem, there is always something you can do and succeed at. It matters that you don't just give up. Unleash your imagination. Shape the future. "

Stephen Hawking, Brief Answers to the Big Questions

Acknowledgements

First and foremost, I would like to express my deepest gratitude to my supervisor Dr. João Ventura. His office door was always open whenever I ran into a trouble spot or had a question about my research or writing. Thank you for the help, keeping me on track, criticism and motivation and responsibility bestowed on me. I am also thankful to my co-supervisor, Paulo Aguiar for his help.

I am especially thankful to Dr. Catarina Dias for the enormous help throughout the course of my work. This included, depositing too many Al films, chapter and runsheets reviews, clean-room and electrodeposition tips, problem solving, helpful criticism, brilliant ideas and much, much more.

Thanks to Rita Carvalho Veloso for letting me use her SEM session and to Dr. Daniela Silva for the measurements.

I would like to acknowledge Csaba Forró for all the help with my numerous questions about the microfluidic fabrication and his sympathy in providing me the original CAD files for the stomach design.

I am also thankful to Paula Quitério for all the help provided in the Alumina laboratory.

I also want to refer Giuseppe Massobrio for answering my long emails with doubts about the circuits simulations and for providing the original SPICE code which helped me a lot with the simulations performed

Thanks to Mónica Cerquido, for her valuable input and help with the microfabrication procedures of the microelectrodes.

I also want to thank Prof. Paulo Marques for the cleanroom knowledge transmitted and to Ana Sofia Queirós for the help with cleanroom processes and DWL scheduling.

I am grateful to Cristina Furtado, José Paulo and Hugo Sousa for all the moments shared since the beginning of our journey in this course.

I thank Orfeão Universitário do Porto for all the experiences, voyages, life lessons and friendships proportioned. I specially thank Francisco Cardoso for all our moments together, for making me laugh and for the support in all the bad moments.

I am grateful to my parents for all the love throughout the years, the food, the knowledge transmitted and for putting up with my bad temper after the long days of study and research. I am deeply indebted to my wonderful sister Mariana for all the support she gave me since I was born, for providing me ease in the most stressful moments, for the wonderful food, and for loving me unconditionally.

I thank Gonçalo Carvalho for all our life experiences together, the joyous moments, the interesting conversations and for sharing and cultivating this spark in me for the continuous search of knowledge.

Finally, I want to thank my girlfriend Ângela Baptista for all our moments together, for putting up with me in my most stressful moments and providing me the sense of calm I needed, for making me laugh, for loving me and making my life a happier one.

Yours sincerely,
Henrique Teixeira

UNIVERSIDADE DO PORTO

Abstract

Faculdade de Ciências da Universidade do Porto
Departamento de Física e Astronomia

MSc. Engineering Physics

Micro-structures for morphology guiding and signal recording of neuronal cells: towards an integrated platform

by Henrique TEIXEIRA

Bioelectronics uses electrical signals to interact with biological systems. Sensors that allow for electrical read-out of important disease markers, and implants/stimulators used for the detection and treatment of pathological cellular activity are only a few examples of what this technology can offer. One of the major advancements in neuroelectronics was the invention of planar multielectrode arrays (MEA), which conferred the possibility of reading neuronal signals without destroying the cell. However, these MEAs are limited to the recordings of extracellular field potentials (FPs) rather than the entire electrophysiological signalling repertoire of the brain. Nevertheless, the enormous advances made over the last 50 years in materials science, microelectronics, and nanoelectronics, have prompted a number of laboratories to merge the advantages of planar MEA technologies (non-evasive and durable) with those of the classical sharp and patch electrodes for intracellular recordings. Unlike extracellular planar electrode-based MEAs, the new generation of three-dimensional (3D) vertical nanoelectrodes are designed to functionally penetrate the plasma membrane of cultured cells and operate in a similar manner to classical intracellular microelectrodes. In parallel, advancements in organic electronics or π-conjugated materials have been extensively explored regarding their use in bioelectronics applications. These materials are soft and flexible in nature, providing a better match with organic tissues and also have the electrical advantage of lower impedance and higher capacitance in comparison to common metals, such as gold. The prototypical material of organic bioelectronics is the conducting polymer poly(3,4-ethylenedioxythiophene) (PEDOT) doped with polystyrene sulfonate (PSS). This material has proved to greatly enhance the recording quality and the coupling between electrodes and neuron cells, by

just applying a coating of it in microelectrodes. In the present work we investigate an approach to tailor the fabrication of mushroom-shaped PEDOT:PSS microelectrodes and study their impact and performance. At the same time, we also explored the possibility of reproducing a common microfluidic design and a novel one in a clean-room environment through the use of a Direct Write System (DWS) for practical and economical reproducibility.

UNIVERSIDADE DO PORTO

Resumo

Faculdade de Ciências da Universidade do Porto
Departamento de Física e Astronomia

Mestrado Integrado em Engenharia Física

Micro-estruturas para orientação morfológica e registo de sinais de células neuronais: em direção a plataforma integrada

por Henrique TEIXEIRA

A bioeletrónica usa sinais elétricos para interagir com sistemas biológicos. Sensores que permitem leitura elétrica de marcadores importantes de doenças e implantes/estimuladores usados para a detecção e tratamento de atividade celular patológica são apenas alguns exemplos do que essa tecnologia pode oferecer. Um dos principais avanços na neuroeletrónica foi a invenção de matrizes de multieletrodos planares (MEA), que conferiram a possibilidade de ler sinais neuronais sem sacrificar a célula. No entanto, estes MEAs estão limitados às gravações de potenciais de campo extracelular (FP), deixando de fora todo o repertório de sinalização eletrofisiológica do cérebro. Contudo, os enormes avanços feitos nos últimos 50 anos em ciências dos materiais, microeletrônica e nanoeletrónica levaram vários laboratórios a combinar as vantagens das tecnologias planares MEA (não evasíveis e duradouras) com as dos eletrodos "*sharp*"e "*patch*"para gravações intracelulares. Ao contrário dos MEAs extracelulares baseados em eletrodos planares, a nova geração de nanoeletrodos verticais tridimensionais (3D) é projectada para penetrar de modo funcional na membrana plasmática das células cultivadas e operar de maneira semelhante aos microeletrodos intracelulares clássicos. Paralelamente, os avanços na eletrónica orgânica ou em materiais *pi*-conjugados foram extensivamente explorados em relação ao seu uso em aplicações de bioeletrônica. Esses materiais são de natureza macia e flexível, proporcionando uma melhor correspondência com tecidos orgânicos e também têm a vantagem eléctrica de menor impedância e maior capacitância em comparação com metais comuns, como o ouro. O material prototípico da bioeletrônica orgânica é o polímero condutor poli (3,4-etilenodioxitiofeno) (PEDOT) dopado com sulfonato de poliestireno (PSS). Este material provou melhorar significativamente a qualidade da captação de sinal e o acoplamento

entre eletrodos e células neuronais, apenas aplicando uma cobertura deste polímero na superfície dos microeletrodos. No presente trabalho, investigamos uma abordagem para adaptar a fabricação de microeletrodos PEDOT: PSS em forma de cogumelo e estudamos o seu impacto e desempenho. Ao mesmo tempo, também exploramos a possibilidade de reproduzir um tipo de design microfluídico comum e outro inovador, num ambiente de sala limpa através do uso de um sistema de escrita direta (SED) para reprodutibilidade prática e econômica.

Contents

List of Figures

List of Tables

Symbols

T	Temperature	^{o}C
t	Time	s
Z	Impedance	Ω
I	Electrical Current	A
I_i	Ionic Current	A
V	Potential difference	V
C	Capacitane	F
R	Electrical Resistance	Ω
P	Power	mW
α_T	Thermal Expansion Coeffiecient	$ppmK^{-1}$
f	Frequency	Hz

Abbreviations

AP Action potential

ARF Aspect Ratio Factor

CAD Computer Assisted Design

CC Coupling Coefficient

CP Conducting Polymer

CIL Charge Injection Limits

CMOS Complementary Metal-Oxide-Semiconductor

CNS Central nervous system

CSC Charge Storage Capacity

DIV Days *in vitro*

DWL Direct Write Lithography

DWS Direct Write System

EAP Extracellular action potential

EDL Electric Double Layer

EDOT 3,4-Ethylenedioxythiophene

ES Extracellular Space

gMμEs gold-mushroom microelectrodes arrays

HH Hodgkin – Huxley

IAP Intra-Celullar Action Potentials

LFP Local Field Potential

MEA Microelectrode array

NGF Nerve growth factor

NIL Nano-imprint Lithography

PDMS Poly(dimethylsiloxane)

PEDOT Poly(3,4-ethylenedioxythiophene)

PEDOT:PSS Poly(3,4-ethylenedioxythiophene)

PNS Peripheral nervous system

PSS Poly(sodium 4-styrenesulfonate)

RC Resistor – capacitor

ROI Region of interest

SEM Scanning Electron Microscopy

SNR Signal-to-noise ratio

TEM Transmission Electron Microscopy

UV Ultraviolet

WSP Writing Starting Point

Chapter 1

Introduction

1.1 Motivation

To understand how neuron cells in the brain function and communicate, scientists from various fields have coordinated interdisciplinary efforts. Through the years a multitude of advancements have been made which have shed light on the functional roles from specific regions of the brain, such as: genetic markers, optical and electro-optical methods, electrophysiology, and computational tools to identify neuronal types, explain their molecular workings and decipher principles of neural coding. The brain is a sophisticated system and its activity runs over various temporal and spatial scales that require a broad set of technologies to address these scales. Innovations in experimental methods to record and perturb brain activity and in computational methods to analyse acquired data are needed to understand the brain's complexity as well as advancing our understanding of its function. Tackling this multidisciplinary area, covering Physics, Biology, Chemistry and Electrical Engineering, is Bioelectronics, more specifically Neuroelectronics. This subject studies the interface between the human nervous system and electronic devices. Its main focus is to understand and describe how nervous cells interact and communicate in the nervous system. Although techniques like tomography can give a detailed overview of the morphological aspects and structure of the brain, they do not provide relevant information about the communication between different cells. In that respect, there are several techniques, named electrophysiological techniques, that allow access to the cell. These have allowed us to obtain important biophysical parameters of the cell membrane, like its capacitance and resistance, and record nervous signals. Furthermore, with the development of nano/micro technologies, it is now possible to create hybrid interfaces that enable

the recording of intracellular signals without being evasive. One of those devices is the gold-mushroom shape microelectrode array. Coupling these recording devices geometry with the recent advances in organic electronic materials, which benefit from a chemical structure that is rather similar to that of biological molecules, has "softer" mechanical properties than their inorganic counterparts, and the capability to conduct ionic charge, could finally provide complete access to the neuron messaging system without killing the cells.

1.2 Objective

The aim of this dissertation covers a wide range of domains related to Physics Engineering, Biophysics and Materials Science, specifically on neuroelectronic interfaces. We will explore in depth one of the novel designs in electrophysiological techniques, the gold-mushroom microelectrode arrays (gMμEs), proposing a new material for this microelectrodes: the conductive polymer PEDOT:PSS. We will also explore the possibility of reproducing common and novel microfluidic devices for neuronal studies.

To accomplish this, the following objectives were defined:

- To produce and optimize two types of microfluidic devices;
- To produce and optimize PEDOT:PSS-mushroom shaped electrodes;
- To characterize the morphological and electrical properties of the novel fabricated microeletrodes.

1.3 Document overview

This thesis is organized as follows.

- **Chapter 2** presents a review of the existing literature on the two main subjects with which this work is concerned: neuron electrophysiology and microfluidic platforms in cell culture research. It begins by introducing the neurophysiologic processes in Section 2.1 and continues on to review the proposed models of membrane communication in the neurons as well as confined in microfluidic environments. Section 2.2 presents the most common electrophysiological techniques used, comparing

them and analysing their advantages and disadvantages. Section 2.3 focuses on the gold-mushroom microelectrode arrays, giving a comprehensive review of its origin, fabrication process and principle of action. The equivalent circuit model of these electrodes is presented in two different ways and its differences explained. This is followed by an analysis of the impact of the main features of these devices on the signal quality by comparing the results from different studies, both experimental and theoretical. Next, a proposed explanation for the surprisingly superior experimental coupling coefficient (CC) over the simulated one is presented, followed by a review of the possibility of these devices being capable of acquiring synaptic potentials without penetrating the cell. Section 2.4 explains the advantages of using microfluidic platforms in cell culture research, specifically in the realm of neuroscience. A thorough review of past studies using microfluidic devices containing microelectrodes is given in this section to demonstrate the current state of this technology and provide some insight into the types of research questions being addressed using these devices. Ending Chapter 1 with Section 2.5, where a review of the conductive polymer PEDOT:PSS is presented, along with its method of fabrication and advantages.

- **Chapter 3** details the fabrication process of the microfluidic devices produced in this thesis. It begins by presenting the lithography problems and subsequent solutions common to both designs in Section 3.1, followed by the lithography optimizations made in Section 3.2. The last two sections (3.3 and 3.4), present the separate designs, as well as some of the problems inherent to each design. Section 3.4 depicts the complete process of the stomach design due to being the first time this structure was reproduced with a Direct Write System (DWS).

- **Chapter 4** presents the fabrication and analysis of the novel produced electrodes made of PEDOT:PSS. In Section 4.1 the optimization process is detailed, followed by Section 4.2 where voltammetry and deposition studies of the EDOT:PSS solutions are discussed. Section 4.3 describes the deposition steps and the characterization of the produced samples. Ending with some final remarks are made about the polymer growth mechanism inside these pores, the size of the electrodes impact on the neuronal coupling and a novel design of microelectrodes.

- **Chapter 5** the simulations of the equivalent electric circuit of the neuron-electrode interface are presented with the study on how the coupling coefficient varies with the change in biophysical parameters as well as with the features of the electrode. We show that PEDOT:PSS electrodes provide a better CC value, enabling the recordings of intracellular signals.

- **Chapter 6** summarizes the presented information and provides potential improvements and future work.

Chapter 2

Literature review

2.1 The nervous system: Information processing and communication

The nervous system is a complex system of organs responsible for a wide range of functions in the human body, including the voluntary and involuntary control of other organ systems and the detection of and response to changes to the environment. In vertebrates it consists of two main parts, the central nervous system (CNS) and the peripheral nervous system (PNS). The CNS represents the largest part of the nervous system, including the brain and the spinal cord. The PNS is constituted by the sensory organs, ganglia (clusters of neurons) and the nerves that connect this two subsystems. Together they are responsible for the control of communication between different body parts, with the PNS sending information from it's vast network of spinal and cranial nerves to the CNS via afferent sensory nerves. This information is then processed by way of integration of data which occurs only in the brain, after which, impulses are then conducted from the brain to the spinal cord to muscles and glands [1, 2]. As such, the brain is the central organ of the nervous system, responsible for receiving, processing and transmitting information. In order for the brain to communicate and receive information from the rest of the nervous system it needs a means of transport of information. This is done by excitable nerve cells (neurons) and the synapses that form between those. In Fig2.1 a schematic of a neuron is presented.

A neuron can be structurally divided into three parts: The *soma* containing the nucleus as the center of a neuron is the largest part and therefore is where most protein synthesis occurs. Multiple *dendrites* branch off from the soma, creating the *dendritic tree*,

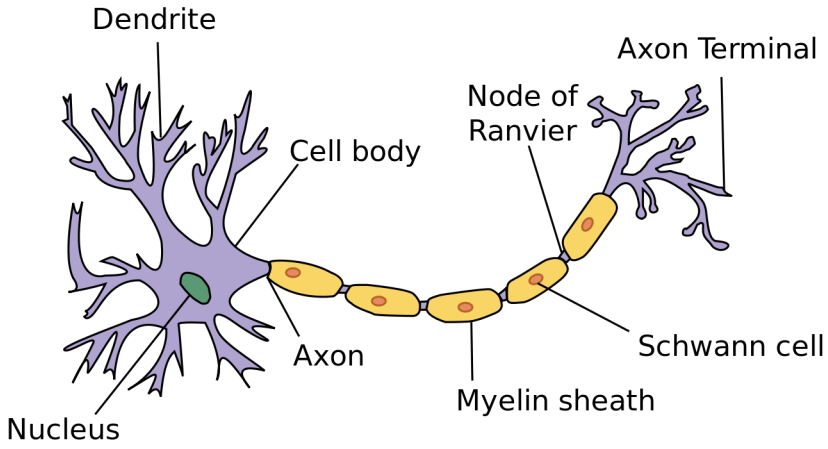

FIGURE 2.1: **Illustration of a typical neuron**. By Dhp1080 [Public domain], via Wikimedia Commons

which receives its input at *synapses*, the connections to other neurons. The third part is the *axon*, which is a fiber that is often thinner than the dendrites, but nevertheless can show quite complex branching as well. Many neurons have only one axon, but this axon may - and usually will - undergo extensive branching, enabling communication with many target cells. Apart from this common property, axons can show a wide range of variations among neurons. They may (as in Fig2.1) or may not be myelinated, i.e. insulated by a myelin sheath that is provided by a surrounding cell. In the first case, there exist periodic interruptions of the myelin sheath called nodes of Ranvier. In this nodes the underlying axon is directly exposed to the extracellular space (ES). The nodes usually contain a high density of ion channels, which provide for an active propagation of a travelling action potential (AP) by means of transmembrane currents that keep the AP alive. Between the nodes, at myelinated parts (or inter-nodes), the signal propagates passively, but significantly faster than in unmyelinated fibers, since virtually no charge is lost across the myelinated membrane. The established view is that axons are one-way paths, i.e. signals are always propagated away from the cell soma towards other cells, although there have been some hints that also propagation in the opposite direction may happen under physiological conditions [3]. This one-way conduction of nerve impulses in the neuron is very useful when trying to model it's behaviour using a circuit model.

The elementary unit of information in the nervous system is the action potential. Action potentials are generated at the axon initial segment close to the soma, and propagate down the axonal arbor, where they will eventually stimulate other neurons. When the excitation is below a certain level, the electrical response from the membrane does not propagate and the membrane is said to be in the passive state; conversely, a section of

membrane conducting an AP is said to be in active state. The question of how it's generated is still not completely answered, as many of the underlying processes are still being discovered. One way of trying to achieve a plausible answer is by simulations. It turns out that nature takes advantage of elementary electrodynamics, using ions as charge carriers and the axonal membrane as an electric circuit.

2.1.1 The Neuronal Membrane

A biological membrane of finite thickness and an electric permittivity has some important electric properties with influence on the two electrolytes it separates. An (electrically charged) membrane attracts oppositely charged counter-ions and repels equally charged co-ions. As a consequence, an electric double layer (EDL) forms: one layer of counter-ions directly at the membrane, and another layer of co-ions, which is attracted by the counter-ion layer. Helmholtz was the first to realize that such an EDL has the capacity to store electric charges and therefore acts as a capacitor. Gouy and Chapman [4] noted that this capacitance depends on the applied membrane voltage and the ionic concentrations; they were also the first to find that the ion concentrations decrease exponentially with distance from the membrane, which can be described by Maxwell-Boltzmann statistics. This added a diffuse layer, latter called the Debye layer [5], where electrostatic interactions close to the membrane are screened (i.e., decaying) exponentially over a characteristic spatial scale; the Debye length. It is obvious that a simple solid membrane will not be sufficient to yield some kind of excitation. As to allow the crossing of the membrane by charged carriers, ions channels must be implemented in the membrane. One such membrane that accomplishes this permeability is the neuronal membrane.

2.1.1.1 Ion Channels

The neuronal membrane is composed of a lipid bilayer with ion channels embedded in it. Ion channels are transmembrane proteins that selectively allow the passage of ions between the intracellular and extracellular spaces. The insulating lipid bilayer separating the two conductive fluid spaces acts as a capacitor, and the membrane capacitance is given by C_m. When the membrane is in the passive state, the ion channels offer an approximately constant resistance to ion flow, and because the ion channels are characterized by their selectivity for certain ion types, this resistance is different for each type of ion [6].

Ion flow through the membrane is governed by two phenomena: diffusion and electrical drift. In the case of the neuron, the concentration of potassium ions inside the cell is greater than that outside, and the opposite is true for sodium ions. Thus, sodium tends to diffuse into the cell, and potassium tends to diffuse out of the cell. However, the presence of other ions inside and outside of the cell that are selectively blocked by the ion channels generates a potential difference across the membrane that produces an electrical drift of the ions [7].* Thus, there exists a potential at which the net flux of ions due to diffusion is balanced with that due to their electrical drift. This potential is called the membrane reversal potential E_L with an proximate value of $-70mV$. The minus sign arises from the convention given that the membrane potential is conventionally defined as the intracellular potential with the extracellular potential as a reference. There also exists a reversal potential for each type of ion, which is defined based on the known equilibrium intracellular and extracellular concentrations of that ion. As such, each type of ion channel in the passive membrane can be modelled as a constant conductance in series with a voltage source and a capacitance representing the lipid bilayer of an infinitesimal patch of the passive membrane. Observing the fact that ion channels, in the membrane are connected in parallel with each other and their circuit elements are all constant, the model can be further simplified. Thus, using Thévenin's theorem, the passive membrane can be modelled as an equivalent circuit with only one conductance g_L and one voltage source E_L in series with the membrane capacitance C_m. This can be seen in Fig. 2.2, showing that the circuit is a simple resistor-capacitor (RC) circuit. From the general know derived equations for the RC circuit, this means that in the passive state, when perturbed by current injection or changes in the potential, the membrane potential will slowly decay to the new potential induced by the excitation and then back to the reversal potential once the excitation is removed.

Passive channels are also called leak channels, in contrast to active channels, whose conductance changes in time, depending on the membrane potential or the concentrations of certain compounds. The active channels which will be now presented are voltage-dependent ones, whose dynamic properties were described later in the seminal work by Hodgkin and Huxley.

*It should be noted that there are other ions involved in the electrical activity of the neuron, but sodium and potassium ions are the main drivers of AP generation; thus, the present conversation focuses on these two ions.

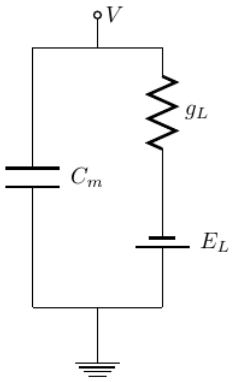

FIGURE 2.2: **Equivalent circuit for a patch of membrane.** A patch of membrane can be represented by a capacitance C_m in parallel with a series of a leak conductance g_L and a battery E_L representing the (Nernst) reversal potential.

The electrical potential generated across the membrane at electrochemical equilibrium, the equilibrium potential, can be predicted by a simple formula called the Nernst equation. The Nernst equation gives a formula for one ion species that relates the numerical values of the concentration gradient to the electrical gradient that balances it. For an X ion with given outside concentration X_0 and inside concentration X_i, the Nernst potential V_X is given by

$$V_X = \frac{RT}{zF} \ln(\frac{[X]_0}{[X]_i}) \tag{2.1}$$

Where R is the universal gas constant, T is the temperature in Kelvins, F is the Faraday's constant and z is the valence of the ion in question. As such, when using this equation for the sodium and potassium ions, the value of the equilibrium potentials obtained should equal to the resting potential. Interestingly, this was not observed experientially by Hodgkin and Huxley. Taking the values from their work [8, 9] and plugging them into equation 2.1, we obtain a value of 56 mV and -77 mV for the sodium and potassium equilibrium potentials, respectively. We now know that the reason for this discrepancy is because there are other classes of ion channels beyond the passive ones. Those are the active ion channels which can be classified by type of gating, i.e. what opens and closes the channels. The most common are: voltage-gated ion channels which open and close in response to membrane potential and ligand-gated ion channels which react to specific ligand molecules binding to the extracellular domain of the receptor protein [6]. The main difference when modelling this active ion channels in relation to the passive ones is that their conductance is not constant. In relation to the sodium and potassium channels we now know that these are regulated by ion pumps, more specifically

the $Na^+/K^{+0} - ATPase$ enzyme [10]. We also know now, that the potassium channel has a persistent conductance and the sodium an transient one. The persistent conductance involves a number of conformational changes (not know at the time of the HH experiments). In the case of the K^+ channel it consists of four identical subunits where all four have to undergo a structural change for the channel to open. This can be mathematically modelled by using the law of large numbers as such;

$$g_{ion} = n^k \tag{2.2}$$

where k represents the identical but independent events that are needed for a channel to open, and one of these events happens with probability n. If large numbers of channels are present, and if they act independently of each other (which experimental evidence suggests they do to a good approximation), then, the fraction of channels open at any given time is approximately equal to the probability that any one channel is in an open state [11]. The transient conductance only opens transiently when the membrane potential is depolarized because they are gated by two processes (subunits) with opposite voltage dependences. Thus one of the gates behaves just like the persistent one seen in eq. 2.2, and the other type of gate is denoted by h is the probability of not blocking the channel. For the transient conducting channel to be conducting both gates must be open, and if the two gates act independently, the probability of this occurring is

$$g_{ion} = n^k h \tag{2.3}$$

This can be seen in the scheme of Fig. 2.3

2.1.1.2 The Hodgkin-Huxley System of Membrane Excitation

In a series of five papers, Hodgkin and Huxley [8, 9, 12, 13] presented a mathematical model of the generation and propagation of the AP in a squid giant axon. They developed this model on the basis of electrophysiological measurements in which they isolated the behaviour of the sodium and potassium ion channels in response to changes in membrane potential. They did this by studying the ion channel kinetics in the squid giant axon, a fiber that can be up to 1 mm in diameter, providing a very accessible way for electrophysiologic measurements. They considered only three ion channel types: two voltage-dependent channels selective for sodium (Na^+) and potassium (K^+), respectively, and one (virtual) leak channel. This leak channel accounted for the movement of other

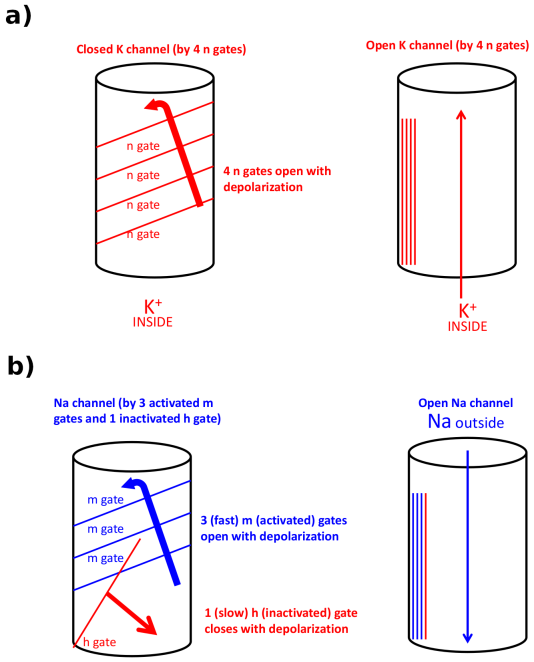

FIGURE 2.3: **Representation of the gating scheme for the ion channels first proposed by HH. (a)** Potassium ion channel gating mechanism; **(b)** Sodium ion channel gating mechanism. Taken from the Coursera online course *"Synapses, Neurons and Brains"*

less prevalent types of ions across the membrane. This results in the electric circuit of Fig. 2.4. Using Kirchhoff's current law for a parallel circuit, the equation for the current reads (when there's an applied external current):

$$C_m \frac{\partial V_m}{\partial t} - I_L - I_{Na} - I_K + I = 0 \tag{2.4}$$

Where the I_L, I_{Na}, I_K, are the associated currents of the three different conductances and I is the applied (or measured) current to the circuit. Thus, the total incoming current of a neuronal membrane patch can be expressed as (rearranging eq. 2.4):

$$I = C_m \frac{\partial V}{\partial t} + (I_L - I_{Na} - I_K) \tag{2.5}$$

The ion currents, for the ion i, are expressed as:

$$I_i = \alpha_i \cdot \bar{g}_i (Vm - E_i) \tag{2.6}$$

Where $\bar{g}_i$ is channel conductance of the ion i and α_i is the adimensional parameter that takes different expressions according to the type of channels as discussed above. For the leak channel this parameter equals unity, as for the other they follow eqs.2.2 and 2.3. HH

used this equations in conjunction with their analyses of the results obtained from the electrophysiological measurements and proposed that the channel conductance values for sodium and potassium were modelled as such:

$$\alpha_{Na} = m^3 h \tag{2.7}$$

$$\alpha_K = n^4 \tag{2.8}$$

where m, h and n time and voltage dependent gating particles – taking values from the interval $[0, 1]$ [12].

FIGURE 2.4: **Equivalent circuit for the Hodgkin-Huxley membrane patch model.** It consists of a membrane capacitance C_m in parallel with three branches, each consisting of a series of conductance and battery, representing the ionic current and reversal potentials, respectively. Note that the voltage-gated conductance are dynamic, while the leak conductance does not change over time.

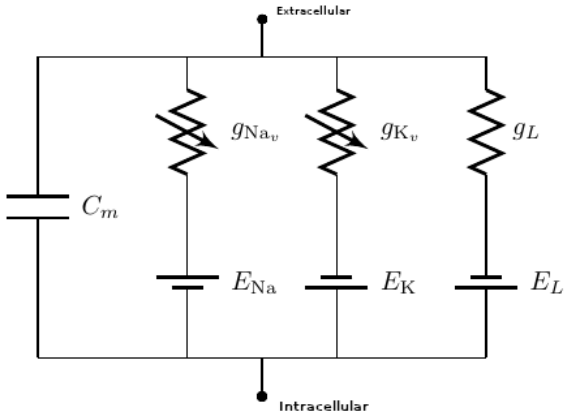

It's also important to note that the circuit in Fig. 2.4, still represents an RC-circuit. Thus, the circuit has time constant at which the capacitor discharges through the resistor to approximately 36,7% of it's initial charge voltage. Only in this case, it represents the decay of the spike produced by the neuron, which was measured by HH to be of about 20 ms for the giant squid [12].

Additionally, they proposed that each individual gate acts like a first order chemical reaction with two states, which can be written as: shut $\underset{\beta}{\overset{\alpha}{\rightleftharpoons}}$ open. The factors α and β are called transition rate constants, where the first is the the number of times per second that a gate which is in the shut state opens, while second one is the number of times per second that a gate which is in the open state shuts. They managed to write the dynamics equations for this rate constants, which must be incorporated into eq. 2.6 when simulating the HH model.

The HH model has revealed the temporal progression of ion movement across an patch of membrane during an AP to be as follows; When the membrane reaches a certain voltage, the sodium channels become activated, causing a sudden influx of sodium into the cell. This increases the membrane potential further, causing more sodium channels to open and producing a snowball effect responsible for the sharp increasing phase of the AP. When the membrane potential reaches its peak, the potassium channels begin to activate to repolarize the cell by producing an efflux of potassium. The response of the potassium channels to the voltage is slower, so the repolarization of the cell occurs more slowly than the initial depolarization. During repolarization, the sodium channels also inactivate, aiding in the repolarization. The activation of the potassium channels and inactivation of the sodium channels continues after the membrane has reached its reversal potential, causing it to dip below this value; this produces what is called the refractory period, during which it is more difficult for the membrane to produce a new AP.* This mechanism ensures that the signal does not propagate backward. Finally, at the end of the refractory period, the membrane potential decays back to its reversal potential [1, 2, 7].

Although the HH model is still widely used in simulations work, multiple corrections have been done to the original model to rectify some incorrect assumptions. In the simulation part of this work, a correction was introduced into the HH model to correct one of these assumptions. In the original model the leak current is referred to as a linear time-invariant conductance, while the currents of the sodium and potassium ions channels are referred to as linear time-varying conductances with associated activation and inactivation parameters. This assumption is now considered incorrect and leads to contradictions as "anomalous impedances" [14]. To compensate such drawback, the potassium activation parameter, and the sodium activation and inactivation parameters are considered as proportional to a state voltage-variable of a linear capacitor. As such, the I_K and I_{Na} can be reformulated as algebraic equations and the HH linear time-varying conductance of the sodium and potassium currents can be replaced and modelled by sub-circuits, as seen in Fig. 2.5 [15]. This permits a much easier code implementation of the HH model in a SPICE language.

It is important to note that the HH model just presented only represents a single patch of axon, as there is no spatial dependence. This corresponds to reducing the neuron to a

*The refractory lengths, were also measured by HH for the whole neuron and for each individual ion channel by the use of drugs

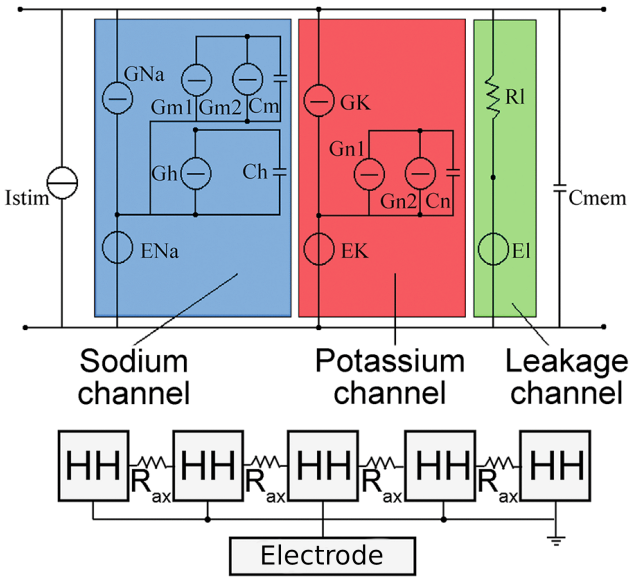

FIGURE 2.5: Top: HSPICE implementation of a single compartment HH model circuit. Bottom: schematic representation of the compartmental approach, connected to an arbitrary electrode interface. Adapted from [15]

point in space. In the real world, however, neurons can show quite complex morphologies, and channel types and densities can vary significantly across different parts of the neuron. In search of a mathematical model for this, neuroscientists have rediscovered cable theory – originally developed to study signal decay in underwater telegraphic cables by Lord Kelvin – to describe the potential spread in complicated neuronal morphologies.

2.1.1.3 The Cable Equation

To take into account the spatial spread of an injected current or perturbation to the membrane at a specific point x along the axon, the RC circuit presented in the previous section must be extended because of it's limiting point representation. To facilitate the modelling of the axon, it can be reduced to a one-dimensional model because of the large longitudinal extent of the axon relative to it's diameter [16]. In Fig. 2.6 a representation of the cable circuit model is shown.

In this scheme, we see the extension of the previous point representation RC circuit to a succession of this circuits, representing axon patches which are interconnect by a resistance r_i. This resistance is the parameter used for the intracellular cytoplasm which is assumed to be a purely ohmic resistor. To note that, in this representation of the model, it's assumed that the longitudinal conductance of the intracellular space is much greater than that of the extracellular space and thus all of the longitudinal current flows through the

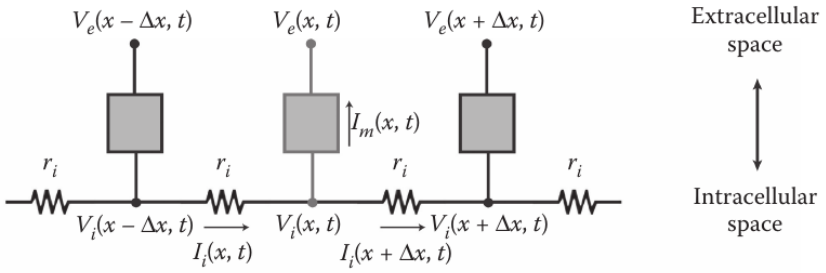

FIGURE 2.6: **Cable circuit model of the axon.** The axon can be modelled as a collection of point representations connected in series to form a two-dimensional cable-like structure. Adapted from [16].

axon. Using Kirchoff's law, the currents in the cable circuit model can be deduced. This is generally useful for simulations with interest in the propagation AP through the axon, however this is not the case in this work and as such this section will not be explored further. One important final note, is that in similarity to the HH temporal model, this model as also an important parameter connected to the AP; the length constant $\lambda = \sqrt{R_m/r_i}$. Where R_m is the inverse of the previously defined parameter, g_L. The length constant represents the spatial spread of the current.

2.2 Recording and stimulating neuronal activity using microelectrodes

A microelectrode when coupled with an electrode, can detect the changes in the extracellular field caused by the current flows from all ionic processes across the morphology of the closest neuron and from other nearby cells [17, 18]. The effect of the transmembrane currents on the electric field and the detected potential on a microelectrode depend on the magnitude, sign, and the distance from the recording site [19]. An AP is a biophysical event that occurs once the neuron's transmembrane potential reaches a threshold due to stimuli or other inputs (for example, synapses). On the other hand, we consider a spike to be the signal from a putative AP. For extracellular recordings, spikes are commonly identified as voltage signals that exceed a threshold. During an AP, the initial rapid Na^+ ion influx creates a sink and results in a large negative spike in the extra-cellular action potentials (EAP). Thereafter, the slow K^+ efflux produces a source resulting in a small positive spike. In contrast, intra-celullar action potentials (IAP) first shows a positive spike and

later a negative volley. EAPs are usually around tens to hundreds of microvolts in amplitude and $<$ 2 ms in duration, while IAPs are at tens of millivolts and around the same duration as EAPs [17]. If IAPs can only be detected by direct access inside the neuron, e.g., patch-clamp, EAPs can be identified when electrodes are placed at the vicinity ($\sim$100 μm) of the spike origin [20], usually around the soma or the axon initial segment. Aside from measuring single and multi-unit spiking activity, electrodes also sample local field potentials (LFPs). The LFP is assessed by the signal content in the low-frequency band of the recorded signal ($<$ 300 Hz) [17, 21], while EAPs are analysed after filtering the LFP out (300–3000 Hz [22].

2.2.1 Electrophysiological Techniques

To study the cell networks different techniques have been developed. In the following, a brief overview of the most relevant is presented.

Classical intracellular electrodes

The first genuine intracellular recordings were made by gaining direct access to the cell cytosol by piercing into the plasma membrane with a sharp glass electrode [Fig. 2.7 (a1),(a2)] or by mechanically "breaking" the plasma membrane by suction through a patch electrode along with the formation of a $G\Omega$ seal resistance between the glass wall of the electrodes and the plasma membrane [Fig. 2.7 (a3),(a4)] [23]. Both techniques have good coupling coefficients [24]. However, because of their working principle, an alteration of the ionic content of the cytosol and subsequent dilution of diffusible molecular entities into it causes an interference with the normal physiology leading to the death of the cell. To overcome this problem, Horn and Marty [25] developed the perforated patch configuration [Fig. 2.7 (a5)], where, rather then breaking the cell's membrane to gain Ohmic access to the cytosol, they introduced ionic channels such as nystatin or gramicidin into the patch electrode solution. These channels then integrate with the plasma membrane, which, together with the formation of high seal resistance between the plasma membrane and the internal wall of the patch pipette, form a perforated $G\Omega$ patch configuration. Its working principle permits recording of intracellular potentials whilst the electrode *per se* remains outside the cell.

The three electrode techniques here described all present the higher coupling coefficient values until today. However, the first two lead to cell destruction, all of them need

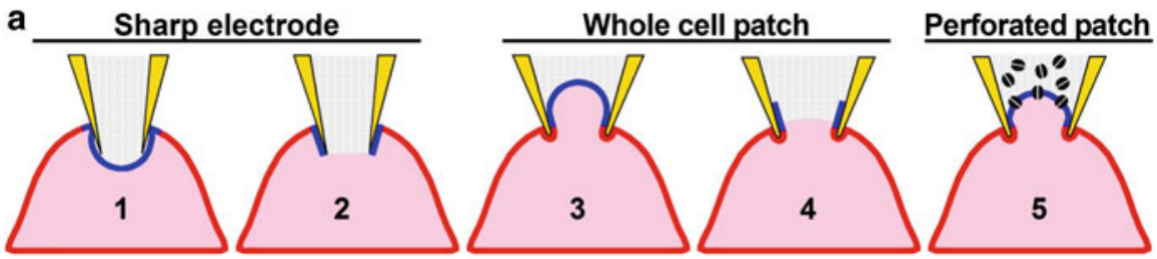

FIGURE 2.7: **Scheme depicting cell–electrode interfacings formed by classical intracellular electrodes.** When a sharp glass microelectrode is mechanically driven against the cell membrane it forms a "membrane dimple" *(a1, blue)*. An electroporating pulse breaks open the plasma membrane that faces the electrode tip and a seal is formed between the external side of the glass wall and the cell plasma membrane *(a2)*. In the whole-cell patch configuration a membrane patch is sucked into the electrode *(a3, blue)*. Application of additional suction breaks the membrane open and a $G\Omega$ seal is formed between the plasma membrane and the inner surface of the glass wall *(a4)*. Another electrode/cell recording configuration is the whole-cell perforated patch *(a5)* in which, after $G\Omega$ seal formation, ion channels within the patch electrode (black) integrate into the plasma membrane to lower the junctional membrane resistance. (Adapted from [26]

to be manually inserted into the cells, requiring extreme precision and expertise [24, 27]. Also, because of their configuration, they cannot be used in multisite recordings or incorporated into microfluidic devices, for example.

3D Vertical Nanowires

Vertical nanowires (Fig. 2.8) are very narrow structures grown usually by means of focused ion beam deposition or other common semiconductor manufacturing techniques. They've attracted a lot of attention in different applications, specially in neural interfaces due to their high aspect ratio. The common used configuration for this type of electrodes to perform intracellular recordings is by means of a nano-field-effect transistor (nano-FET) incorporated at the tip of this structures, pioneered by Tian *el al* [28].

The most promising works until now were the ones were a current pulse was used to electroporate the cell's membrane enabling the recording of intracellular potentials whilst the electrode remains outside of the cell [30, 31]. In fact, it still remains unclear whether after electroporation the tip of the nanoelectrodes pierces the plasma membrane or generates nano-holes in the junctional membrane. However, independently of the actual mechanism, the intracellulary activity access by electroporation only lasts a few minutes. This electrode insulation process is most likely triggered by membrane repair mechanisms. The best results achieved until now with vertical nano-wires to record intracellulary were

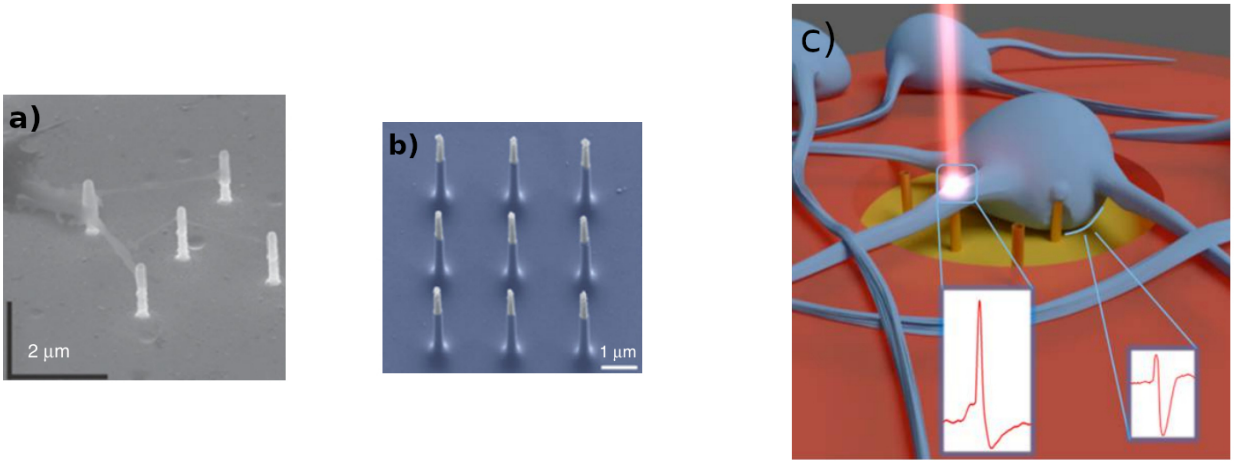

FIGURE 2.8: **(a)** Passive nanopillar electrode-based MEA constructed of five vertical nanoelectrodes on a common platinum pad. **(b)** Vertical nanowire MEA constituted by nine silicon nanowires on a common pad. **(c)** Schematic illustration of the plasmonic optical operation platform integrated with a hippocampal neuronal culture-system. Shown here is a representation of neurons on MEA with 3D nanoelectrodes. The 3D nano-electrode excited with laser records intracellular activity, while the rest of the electrode captures extracellular signals. Adapted from [26, 29]

made by Dipalo *et al* [29], where plasmonic optoporation was used to porate the junctional membrane without interrupting ongoing spontaneous AP activity. Unfortunately, despite this advantageous conditions, the intracellular recordings were only maintained by just over an hour, after which the electrodes were insulated too.

Microelectrode Array

Microelectrode arrays (MEAs) are devices that allow the measurement of many neurons through the incorporation of tens or hundreds of recordings sites in the substrate where the cells are grown. These devices can measure cells activity or deliver impulse signals to the cells to excite them, or commonly both (depending on the specific MEA type). When recording, the electrodes on an MEA transduce the change in voltage from the environment carried by ions into currents carried by electrons (electronic currents). When stimulating, electrodes transduce electronic currents into ionic currents through the media. This triggers the voltage-gated ion channels on the membranes of the excitable cells, causing the cell to depolarize and trigger an action potential if it is a neuron or a twitch if it is a muscle cell. With the need to increase the number of simultaneously measured neurons, the reliability of spike sorting and to allow for source localization coupled with the advances in lithographic techniques fuelled by the semiconductor industry, a huge growth in these multichannel devices was seen since the 80s with the first commercial applications

for *in vitro* and also *in vivo* becoming available as early as the late 90s [32]. The key advantage of integrating active electronic components on the same substrate as the actual electrodes is the possibility of a much higher electrode number and density. Due to the possibility of using active switches to time multiplex signals,integrated circuits make it feasible to transfer data from such high channel counts off chip and to overcome the connectivity limitation of passive devices. Additionally, such co-integration allows amplifying the signals with optimal quality, due to minimal parasitic capacitances and resistances [33]. The type of MEAS in current literature and commercial use are truly vast, and they can be distinguished by different categories. For example, emphasizing the type of transducers used (multi-transistor array, microelectrode array, multielectrode array, micro-nail array, capacitive-coupled array, 3D MEA), the type of substrate (active array, passive array, silicon array, CMOS array), the shape of the device (needle-type probe, polytrode, neuro dish), the channel count (multichannel array), the electrode density, or the application (implantable array, *in vivo* MEA, *in vitro* MEA) and more [32]. With such a vast catalogue, choosing the type of MEA is highly dependent on the type of recorded signals needed to obtain. Generally, an important goal in electrode fabrication is to achieve low impedance which becomes difficult with the ever decreasing size of these sensors. To overcome this, an increase of the effective surface area must be achieved by design (gold-mushroom electrodes, Carbon nano-tubes, etc.) or through modification of the surface properties with conductive polymers like poly(3,4-ethylenedioxythiophene) (PEDOT:PSS) [32]. In Fig. 2.9 we encounter some examples of MEA devices in existence.

Due to the non-invasiveness of most of these electrodes, with exception of the nanowire and carbon nanotube arrays [37], the acquired signals are of the extracellular type. Recordings of ”in-cell” type signal with MEAs have only been obtained using vertical arrays due to the electroporation of the cellular membrane and by gold-mushroom arrays which will be discussed at length in the next section.

With so many options available to record neuron activity, it might be difficult to choose the best. Table 2.1 summarises the most common techniques, with a comparison of the coupling coefficient and the recording stability for each one.

If the purpose is to study a network of neurons for an extended period of time to test the effects of a certain drugs, for example, one might lean into choosing Planar MEAs which have a stability of months. However, its coupling coefficient (CC) is very low hindering the possibility to study the intracellular signals which are of most importance. As

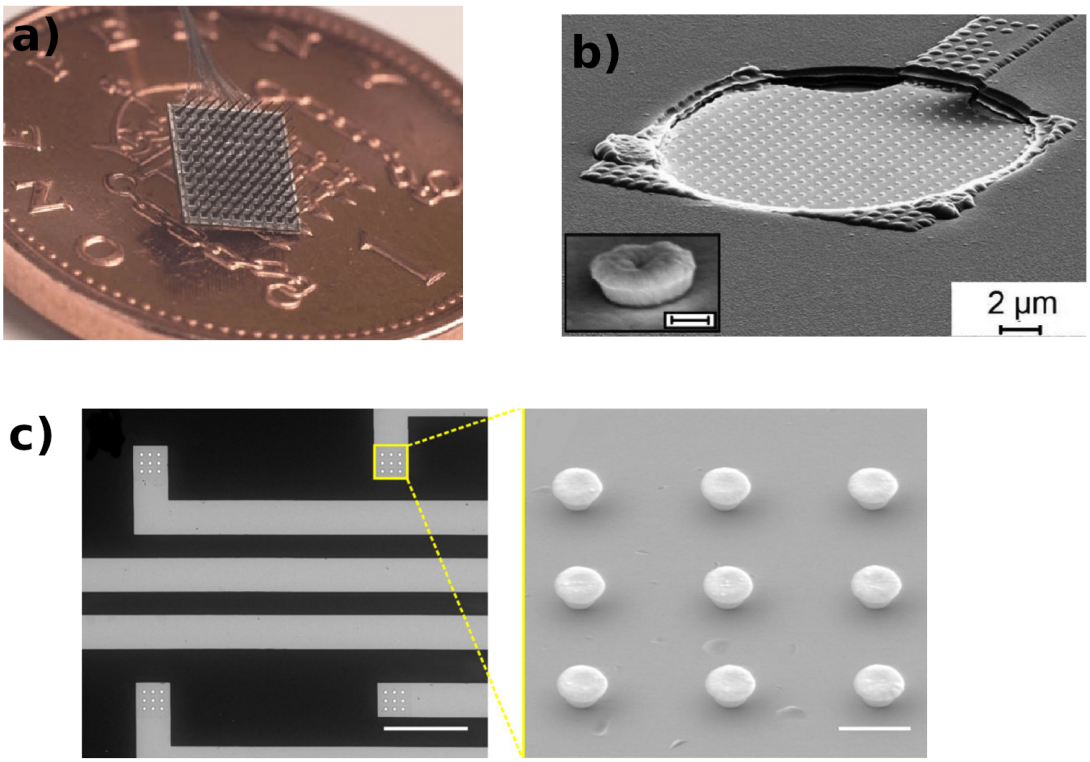

FIGURE 2.9: **(a)** A 100-electrode, $4 \times 4\ mm^2$ microelectrode array (BrainGate), shown on a UK one pence piece for scale. **(b)** SEM picture of a nanostructured MEA electrode with tube-like nanostructures, a stalk diameter of 400 nm and a pitch length of 1 μm(inset: magnification of a tube-like nanostructure, scale bar 200 nm). (c) SEM images of 3D-microstructured microelectrodes. (Left) Top view of the reading tracks and the islets where the micromushrooms are deposited (scale bar= $100\mu m$). (Right) Tilted image of a fabricated 3×3 islet of micro-mushrooms (scale bar= $5\mu m$). Adapted from [34–36].

Technique	Cell type Studied	CC	Stable Recording Time
Sharp-glass electrode	Multiple	1	Hours
Patch-clamp electrode (whole cell)	Multiple	1	Hours
Planar MEA	Multiple	0.001-0.01	$>$ months
GMμEs	Neurons	0.5	2 days
Vertical Nanowire electrode arrays (VNEA)	Neurons	0.3	10 min

TABLE 2.1: Characteristics of the methods available for recording and stimulation neurons. Adapted from [24].

such, at the present time the best option in terms of coupling coefficient and stable recording time is the gMμEs which will be discussed below.

2.3 Gold mushroom microelectrode arrays

One of the most emergent and promising extracellular method is the mushroom-shaped microelectrode arrays [Fig. 2.10 (a) and (b)]. To overcome the low coupling coefficient and subsequently the low value of the resistance seal, Spira *et al* developed a new method of fabricating 3D electrode structures that mimic neuronal structures in terms of their shape and dimensions [38]. Their strategy relied on the premiss that combining 3D electrodes with an appropriate surface functionalization could "trick" neurons to "see" these structures as neighbouring biological entities. This would, in turn, lead to a contact and subsequently internalization by endocyotic mechanisms [39].

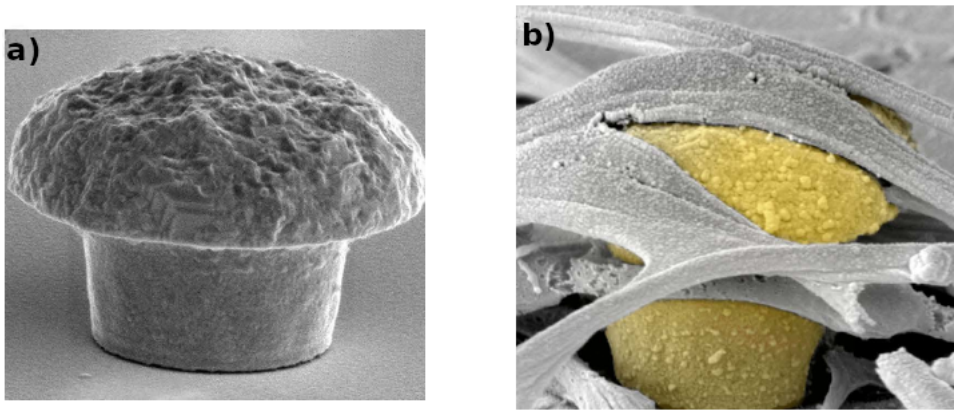

FIGURE 2.10: **Scanning electron microscope images of gold mushroom-shaped electrodes that were fabricated to examine the structural interface between cultured rat hippocampal neurons and the protruding microstructures**. (**a**) SEM image of the gMμEs, (**b**) Neurites engulfing a gMμEs, tightly adhering to the gold surface. Adapted from [40].

This leads to a high seal resistance value and to a reduced cleft between the neuron and the microelectrode, that allows increasing the value of the coupling coefficient. Contrary to the planar sensor based MEAs which are limited to recordings of extracelullar field potentials generated by propagation APs, gMμEs are also able to record sub-threshold inhibitory, excitatory and electrotonic synaptic potentials generated by individual neurons [39]. Enabling the use of this type of devices to study the fraction of cells that fire at very low rates or do not fire at all, as in some brain areas or cultured neuronal networks which are ignored when using planar sensors. Furthermore, with gMμEs it is possible to apply high voltages without damaging and record and stimulate cells during days [41]. This enables to perform effective "in-cell" recordings with excellent signal-to-noise ratio gathering advantages of the intra and extracellular electrophysiological techniques [41, 42].

2.3.1 Fabrication process

The standard method of fabrication for these type of MEA's follows the sequential steps used by Spira and his colleagues, which are: deposition [Fig. 2.11 (b)], spin coating [Fig. 2.11 (c)], exposure and development [Fig. 2.11 (d)], electroplating and photoresist strip [Fig. 2.11 (e)] [38]. This steps are summarized in Fig. 2.11 The first step of the process is the deposi-

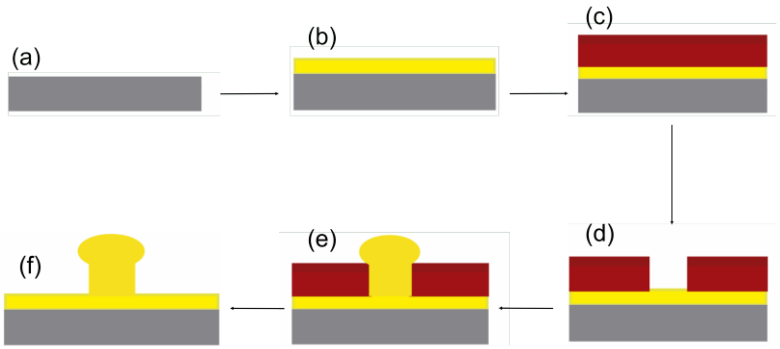

FIGURE 2.11: The sequential steps to produce the gMμEs: (a) silicon substrate; (b) gold thin film deposition; (c) spin coating of the photoresist; (d) exposure and development; (e) electrodeposition and (f) strip of the photoresist.

tion of a thin film of gold (Au) on top of the substrate (usually glass or silicon) [Fig. 2.11 (b)]. The thickness of this layer will influence greatly the electrodeposition step, so it must be chosen carefully. Next, the pattern cast for which the mushrooms will grow from is created by spin coating, exposing and development of the photoresist [Fig. 2.11(c,d)]. The exposure can be made with different methods such as Direct Writing using a laser source or the common way using a UV lamp though a mask aligner. Afterwards, electrodeposition of gold is used to grow the gMμEs [Fig. 2.11(e)]. Finally, the photoresist is etched leaving only the desired structures on the substrate. A more detailed information about the experimental methods and the fabrication process can be found in Chapter 3. Although these are the steps commonly followed by researchers in current literature [36, 38] there are other approaches used like thermal nano-imprint [35]. The fabrication process is of greatest importance, and it must be optimized to produce the desired features before focusing on trying to integrate a poor fabricated device in any cell culture. Generally this may take a long time when there are many parameters to optimize and external factors to compensate for. For example in 3 a detailed account of the fabrication process of the finished device produced in this thesis is presented, where it's possible to observe the influence of varying one or various.

One of the most important steps is the definition of the ring structures on the cast where latter the gMμEs will be grown through electrodeposition. This structures must be completely open in order to the complexed ions reach the surface of the substrate and start the electrodepostion reaction. There are different ways to perform this step and they can have different impacts latter on as well as the chosen diameters for this features. Briefly I'll review some techniques used to expose the rings for gMμEs grow and then present a short summary of the influence the diameter, size, and temperature in the electrodeposition step.

The design needed to produce a mask for growing mushroom-like structures is very simple and consists of rings, usually assorted in arrays to be used as individual electrode pads. The lithography tools used to go from Fig. 2.11 c) step to d) step are vast, however the chosen one generally depends on the available devices in one's laboratory and also on the limit resolution of the device. I'll review here three tools: Direct Write Systems, Nano-imprint Lithography (NIL) and Electron-beam Lithography. A direct write system uses a tabletop laser to directly write onto the desired substrate the designs created in CAD software's or others (depending on the machine) and usually has limiting resolution of $2\mu m$. Because it writes exactly the design provided it brings advantages when it's necessary to expose different layouts in a substrate or when adding,removing or resizing is needed. In Fig. 2.12 a) gMμEs made using such a tool are shown. They have a characteristic stalk which grows narrower from top to bottom, this is due to the fact that a laser as an Gaussian-like shape which will be present in all features written with tools that use laser systems. Nano-imprint lithography is a very simple tool which relies on mechanical deformation of imprint photoresist with a negative mask of the desired design, usually cured with heat or UV light. It has the capacity of fabricating nanometer scale patterns with extreme simplicity. Lastly, E-beam lithography works similar to the Direct Write System, however it uses a focused beam of electrons to draw custom shapes on the surface of photoresists. This technique is the most demanding at handling expertise of the ones presented here. Together with NIL they are able to produce high resolution structures up to the nanometer scale. In Fig. 2.12 b) and c) gMμEs made using E-beam and NIL (respectively) are shown, where the uniformity in the stalk diameter is observable.

However they cost more to use than a tabletop Direct Write system which will always produce a varying diameter stalk because of the intrinsic Gaussian-like shape of the laser and also cannot write features smaller than $2\mu m$. It's important to note here that NIL may

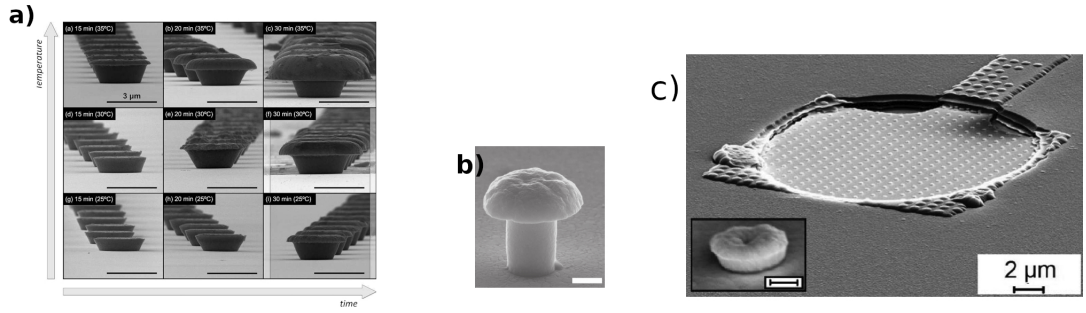

FIGURE 2.12: SEM images of GMμEs produced with different lithography techniques. **(a)** Direct Write System grown gMμEs for different temperatures and electrodeposition times; **(b)** E-beam, scale bar represent 500nm; **(c)** NIL produced gMμEs seen on the inset. Adapted from [35, 43, 44]

seem at first glance a very cheap solution, which it is if an existent cast is available, however producing a cast with resolutions at the nanometer scale requires expensive tools. The diameter chosen for the stalk of the gMμEs will not only influence their performances (see 2.3.5.2) but also the electrodeposition step and subsequently their height too. In classical electroplating, the height h of a deposited material can be given by

$$h = \frac{M \cdot j \cdot t}{z \cdot F \cdot \rho} \tag{2.9}$$

Where M represents the molar mass of the deposited material, j is the current density, t is the electroplating time, ρ is the density of the deposited material, z is the valence number of ions and F is the Faraday constant. From this equation (assuming 100% current efficiency), we see that the height of a patterned surface is proportional to the electroplating time and the local current density [35]. This proportionality of the height in respect to time is seen in Fig. 2.13 *a)* where Cerquido *et al* tested different electroplating times at three distinct temperatures at around $2\mu m$ in diameter. In another work by Decker *et al* a similar study was done but with smaller diameters ranging from 100nm to 600nm for two type of structures, tube (T) and pillars (P). In Fig. 2.13 *b)* we can observe again the relationship between electrodeposition time and height for different diameters. However, this time, the height of the structures with larger diameters raises faster than the height of structures with the smaller ones. This goes against the expected results in equation 2.9, where for narrower structures the field line density should be higher resulting in higher structures.

A possible reason for this phenomena lies in insufficient gold complexed ions being able to reach the surface of the substrate in structures with diameters smaller than 300nm

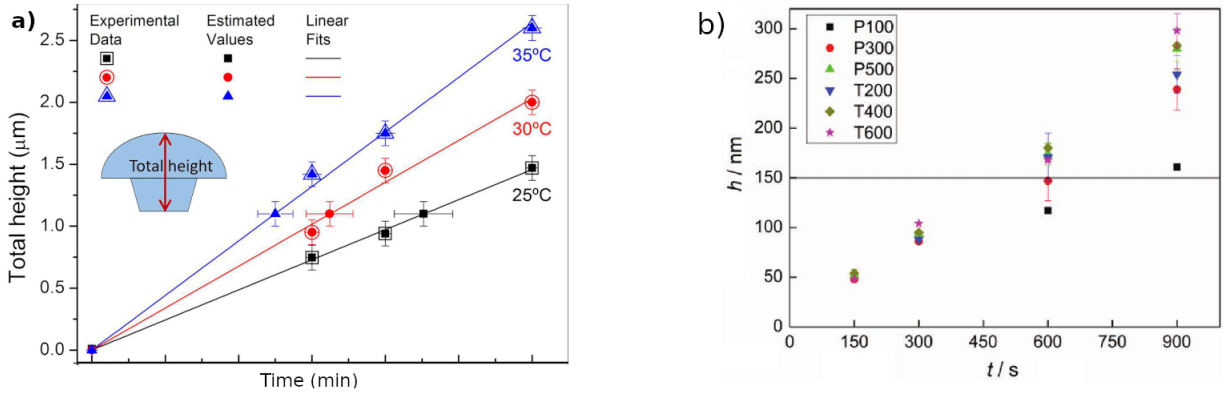

FIGURE 2.13: **Electrodeposition times for different heights and diameters. (a)** Variation of the gMμEs total heigh in respect to electroplating time for a diameter of $2\mu m$; **(b)** Dependency of the structure height on electroplating time separated into different structure types and diameters. Adapted from [43] and [35]

in consequence of their size. Because of this, the deposition rate is lower, thus the slower the structures can grow. For diameters above 300 nm, the experimental results match again the theoretical ones.

2.3.1.1 Functionalization of the gMuEs

After the gold-mushroom microelectrodes arrays are made, it is usually necessary to functionalize them. Functionalization is a surface treatment to convert the surface from hydrophobic into hydrophilic. This surface treatment is necessary because hydrophobic surfaces prevent cell growth [45]. The most common, effective and long lasting surface treatment method generally used is Protein Coating. This method involves sterializing first the region of interest and then it's placed in a concentrated protein solution (such as laminin, fibronectin, poly(D-lysine), etc) for a given time (usually 30 minutes). In this way, neuronal cells sense 2D protein patterns and develop axons and dendrites following the geometry of the patterned proteins.

2.3.2 Neuron guidance

Cultured *in vitro* neurons usually tend to grow in an unordered way, which leads to a non-uniform distribution of the cells in the substrate. To reduce this high entropy, its necessary to create a well-defined network of cells on MEAs by guiding the cells growth patterning. There are various ways to accomplish this using different techniques which have been developed in recent years such as: protein patterning, grooves, etc [46, 47]. These are usually applied to conventional planar MEAs. However, recent studies have

found that, in the case of gMμEs, the electrode pattern itself may be sufficient to greatly influence the neurite growth pattern [36]

2.3.2.1 gMuEs influence on growth pattern

* Since the development of this type of MEAs, there have been experiments that, instead of focusing on the larger signal acquirement quality, studied the effects of the surface topography on the growth patterning of nerve cells. The first evidence came from Panaitov *et al*, who reported that neurites of rat cortical neurons tended to follow the micro-mushrooms (spacing ranges of 3-5 μm)[48]. More recently [36], it was show that neurites grown on top of gMμEs tend to align preferentially at 0°, 45° and 90°, which are the angles formed by near-neighbour/adjacent micro-mushrooms, demonstrating therefore a preference on neurite elongation along the array topography.

2.3.3 Engulfment mechanism

In Fig. 2.14 an illustrated scheme of the engulfment mechanism is shown.

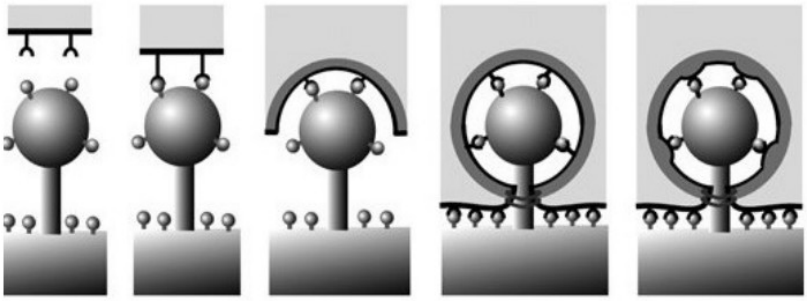

FIGURE 2.14: The engulfment of a mushroom-shaped microelectrode by a cell. Adapted from [42].

The engulfment of the gMμEs is based on the natural phenomenon of particle phagocytosis by living cells, which leads to internalization of large particles in the range of 0.5μm. This process is triggered when foreign particles get close to the cell, activating the initiation receptors present in the cell that will interact with the molecules present on the surface (which shows how important it is to first functionalize the surface of the gMμEs). Afterwards, the cellular membrane engaged receptors recruit a number of proteins that allow the plasma membrane to internalize the particle. Finally, the plasma membrane surrounds and tightens the particle, ending the internalization process when the head

*Taking in account only the studies performed with neurons from small mammalian and micro-mushrooms spacings in the range of ∼0.5-3μm

and stalk of the microelectrode are tightly surrounded by the plasma membrane. Which differs from the actual phagocytosis where the plasma completely engulfs the particles and detaches itself moving freely in the medium. The specific shape and dimensions of the 3D electrodes facilitates the whole process by mimicking the structure and dimension of "spines" that extend from the dendrites of vertebrate neurons [49], leading those to recognize the microelectrodes as physiological structures.

2.3.4 Equivalent circuit of the neuron-microtransducer interface

The performance of microdevices like gMμEs is inherently dependent on the nature of the interface (coupling) between the cell membrane and the sensitive active surface of the microtransducer. To better understand the electrical interface formed between the neurons grown on the substrate and the gMμEs, analog electrical equivalent circuits have been designed [15, 50, 51]. With this equivalent circuits it's possible to simulate various configurations and obtain valuable information, thus saving time testing different configurations to improve the coupling conditions before its fabrication.
Independently of the type of microtransducer, the performance of the device depends heavily on the nature of neuron-microtransducer interface. When an electrode and a biological membrane (such as the one of a neuron) are placed into an electrolyte, an electrified interface develops [52]. This leads to a specific charge distribution known as an Electric Double Layer (EDL) [Fig. 2.15]. As such, in the discussed interface, two EDLs are formed: one at the side of the microtransducer and the other at the side of the neuronal membrane [15]. An EDL can be divided into three different layers (Inner and Outer Helmholtz Plane and the diffusion layer), allowing to model it as an equivalent-circuit of a series of three capacitors, each corresponding to one of the layers. This can be further simplified by connecting a charge transfer resistor in parallel to the capacitors, simplifying the modelling of an EDL as a resistor and a capacitor in parallel.

This means that the neuron-microtransducer interface can be easily modelled by passive electrical components (i.e. resistors and capacitors). Various groups have made models for the neuron-gMμE interface. Here, focus on the one developed by Massobrio *et al* [15]. Which until now has the best implementation conditions because of its use of a Hodgkin Huxley neuron model to take into account the excitable properties of neurons. In Fig. 2.16 (b) a schematic representation of this compartmental approach is presented.

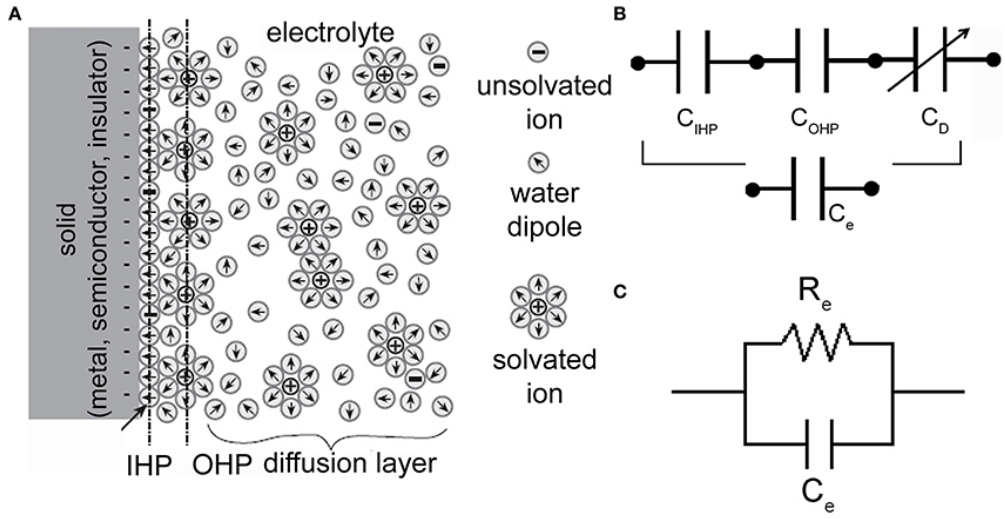

FIGURE 2.15: **Electrode-electrolyte interface and equivalent electrical circuits. (a)** Schematic representation of an electrode-electrolyte interface. **(b)** Series of three capacitors (corresponding to the inner and outer Helmholtz plane, and diffuse-layer) which models the charge distribution at the interface. **(c)** Electrical circuit of an electrode-electrolyte interface. R_e is the charge-transfer resistor and C_e is the double-layer capacitor. Adapted from [53].

The previously discussed EDL equivalent-circuits are seen here (Fig. 2.16 **c)**) as the *Protein-Glycocayx* EDL and the *μelectrode-electrolyte interface* for the neuronal membrane and microtransducer side, respectively. In between these circuits there's another one of great importance which represents the cleft effects, constituted by the seal and spreading resistance.

The original neuron-microtransducer equivalent-circuit developed by Spira *et al* (Fig. 2.17) is very similar to this one with the main difference being that they split the neuronal membrane into two compartments: one coupled to the microtransducer (R_j and C_j) and one uncoupled (R_{nj} and C_{nj}). The other components of the circuit maintain the same biophysical meaning but with different nomenclature [53]. Indeed, some of the parameters defined by Spira *et al* are used in the Massobrio *et al* simulations.

It is also important to note that the equivalent-circuit for basically any microtransducer-neuron interface will have the same components. However, the definition of them is generally much more complex for the neuron-gMμEs interface than for the planar electrodes, due to the complexity of the gMμE geometry.

The physical meaning and derivation of the model components for the specific case of the neuron-gMμEs interface will now be explained briefly, following [15] unless stated otherwise. The neuron stage model was already presented in *"The nervous system: Information processing and communication"* section 2.1.1.2.

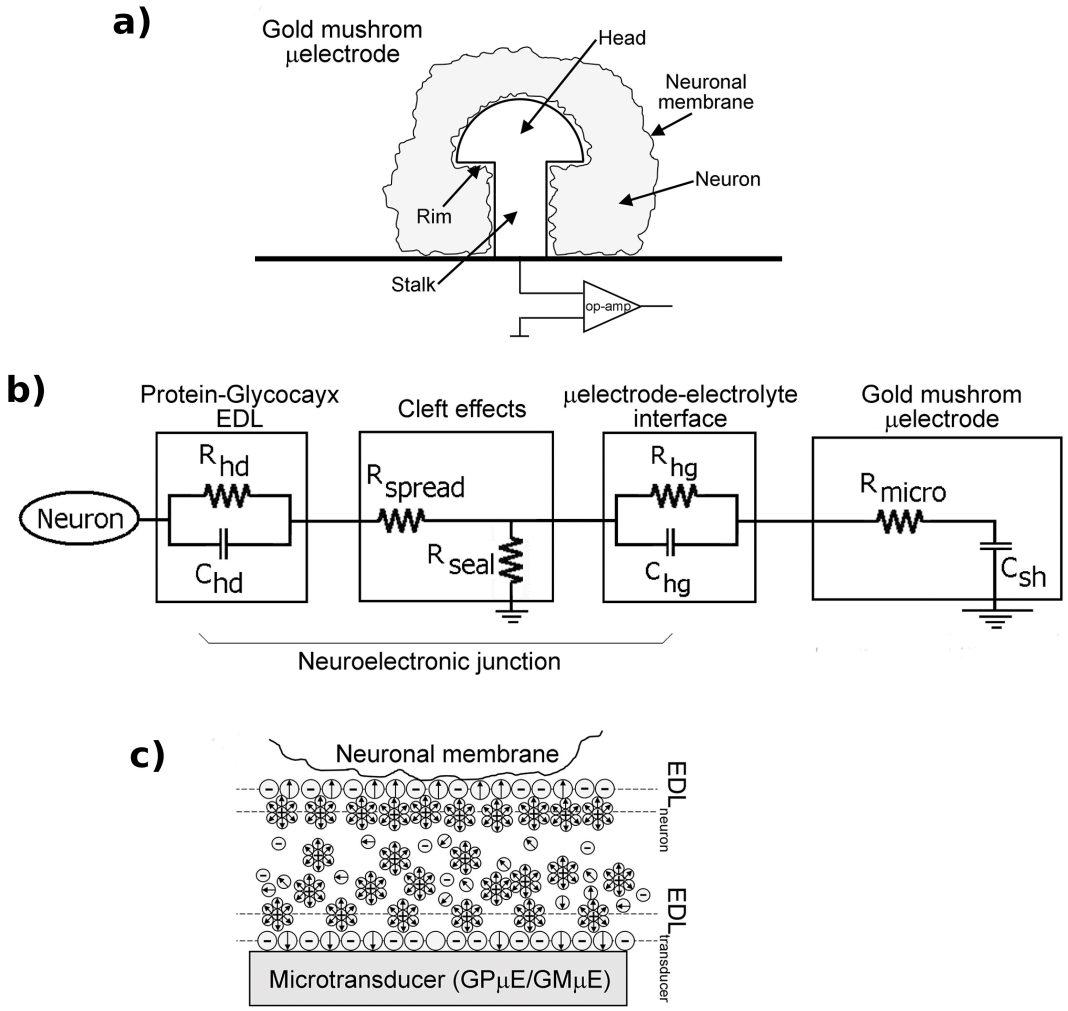

FIGURE 2.16: **(a)** Sketch of the neuron-gMμE interface. **(b)** Circuit of a neuron coupled to a mushroom-shaped microelectrode by a neuro-electronic junction. Each schematic component is explained and defined in the pertinent section. **(c)** Representation of EDL charge distribution in the neuron-gMμE interface. Adapted from [15]

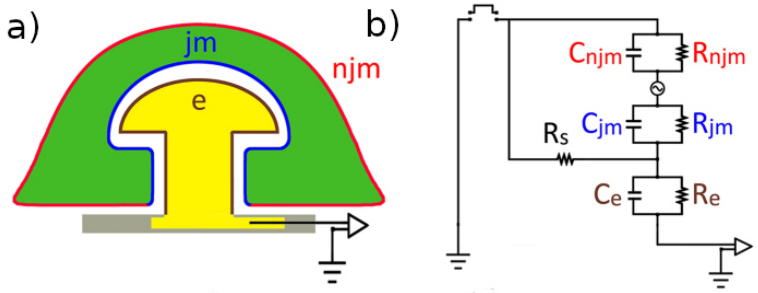

FIGURE 2.17: **(a)** Schematic drawing and **(b)** analog electrical circuits of a gMμEs (yellow) totally engulfed by a neuron (green). Non-junctional membrane - *njm* (red), junctional membrane - *jm* (blue), electrode -*e* (yellow). Adapted from [40]

2.3.4.1 Formation of Seal Resistance

The sealing resistance R_{seal} models how much the cell is attached to the microtransducer, generated by the solution within the gap between the surface of the gMμE and the engulfing cell membrane. This gap may extend from the center to the head of the gMμE to the point in the stalk where the tight engulfment is terminated. It can be represented by three resistors in series, by assuming the seal resistance has a starting point as an imaginary circle on the cap which divides the capacitance of the gMμEs into a,b,c equal parts [54]:

(a) The first is related with the resistor of the gap between the head surface and the cell.

Its derivation is based on the integration of resistors of concentric ring on the cap with α starting angle and ending at an angle of $\frac{\pi}{2}$, resulting in:

$$R_{seal-head} = \frac{\rho_s}{2\pi d_j}\{\ln[\tan(\frac{\pi}{4})] - \ln[\tan(\frac{\alpha}{2})]\} \cdot \delta \tag{2.10}$$

where ρ_s is the cleft solution resistivity and d_j is the cleft thickness which coincides with the electrolyte thickness.

(b) For the second, the resistor of the head bottom rim is given by :

$$R_{seal2-rim} = \frac{\rho_s}{2\pi d_j} \cdot \ln(\frac{r_{head}}{r_{stalk}}) \cdot \delta \tag{2.11}$$

(c) Finally the resistor of the stalk is defined as :

$$R_{seal-stalk} = \frac{\rho_s}{2\pi d_j} \cdot \frac{h_{stalk}}{r_{stalk}} \cdot \delta \tag{2.12}$$

As such, the seal resistance is given by the sum of the previous defined resistances, $R_{seal} = R_{seal-head} + R_{seal2-rim} + R_{seal-stalk}$. These definitions are almost identical to the ones derived by Spira *et al* [54] with the only difference being that each resistor contribution has a multiplicative term, (δ), which is a surface overlapping coefficient taking into account the percentage of the microelectrode sensitive area covered by the neuron [53]:

$$\delta = \begin{cases} \frac{A_{neuron}}{A_{gM\mu E}}, & \text{if } A_{neuron} < A_{gM\mu E} \\ 1, & \text{if } A_{neuron} \geq A_{gM\mu E} \end{cases} \tag{2.13}$$

The starting angle,α, value is estimated in [54] to be of 77.3^o. With it, all parameters are known and are taken from direct measurements, and the final value of R_{seal} may vary

depending on the used values. For example, in [54] the derived R_{seal} value is of 53 MΩ while in [15] it is of 40.16 MΩ.

2.3.4.2 Protein-Glycocalyx EDL Stage Model

To model the equivalent circuit formed by the EDL at the side of the neuronal membrane, Massobrio *et al* opted for using the general equation of resistivity, $\rho = R \cdot \frac{A}{t}$, which is valid both for a GMμE or a GPμE. Thus the resistance is defined by:

$$R_{hd} = \rho_{glyco} \cdot \frac{t_{glyco}}{A_{cont}} \cdot \gamma \tag{2.14}$$

where ρ_{glyco} is the resistivity of the EDL associated with protein-glycocalyx layer, t_{glyco} is its thickness and A_{count} is the portion of the surface area of the attached glyco-layer and microelectrode sensitive area. For the case of a GMμE this area is defined by:

$$A_{GM\mu E} = A_{stalk} + A_{head} + A_{rim} = (2\pi \cdot r_{stalk} \cdot h_{stalk} \cdot \beta) + (2\pi \cdot r_{head}^2) + \pi(r_{head}^2 - r_{stalk}^2) \tag{2.15}$$

where β is the parameter modelling the percentage of engulfment. Lastly, γ is defined as a "correction factor" related to the engulfing-process and to the local EDL induced bended-geometry shape which affect the number of available passive ion channels through which current can flow. For the case of the GMμE, the value of this parameter is equal to unity to best simulate real behaviour conditions.

The capacity then, may be evaluated as:

$$C_{hd} = \varepsilon_{glyco} \cdot \frac{A_{cont}}{t_{glyco}} \cdot \gamma \tag{2.16}$$

where ε_{glyco} is the permittivity of the EDL associated with the protein–glycocalyx layer. In the equations modelling this RC-circuit the parameters $\rho_{glyco}, t_{glyco}, \varepsilon_{glyco}$, where extracted from Thakore *et al* paper, were an optimization based study of equivalent circuit models for representing recordings at the neuron-electrode interface was performed by correcting the parameters used in the know neuron-microelectrode interface models from values taken from experimental results [55].

2.3.4.3 gMuE-Electrolyte EDL Stage Model

The equivalent circuit for this interface is also composed of a resistor, (R_{hg}), and a capacitor, (C_{hg}), in parallel. The definition of both parameters is directly taken from Hai *et al* work [56], which models the EDL interface formed between the gold-mushroom surface and the electrolyte solution. To estimate the value of the resistance they took the experimental value measured in [57] of impedance measurements of gold electrodes in a physiological solution ($\sim 1000G\Omega$) and normalized it by the gMμE surface area. This resulted in a value of $R_{hg} = 1500G\Omega$. For the capacitance, the estimation was performed again by using experimentally measured values, this time from [58], taking the specific capacity of the gold EDL to be $\sim 50\mu F/cm^2$ multiplied by the surface area of the gMμE. The estimated capacity has a value of $C_{hg} = 5pF$.

2.3.4.4 Spreading Resistance

The spreading resistance is the resistance encountered by the current spreading out from the microelectrode into the electrolyte and together with the seal resistance they model the clef effects. In similarity with the derivation of R_{seal}, the spreading resistance is also affected by the surface area of the gMμEs. Thus, it is obtained by integrating the series resistance of shells of solution outwards from the microelectrode. The equations that model this parameter are long to write here and coupled with the fact that this parameter has practically zero influence in the simulated signal it will be omitted. In fact it'll be later show in the simulations chapter that even in the extreme case of setting the R_{spread} value to zero the signal remains unchanged. Other relevant parameters for the simulations are present in the Simulations Chapter

2.3.5 Impact of gMuEs on signal acquisition and the coupling coefficient

The quality of the acquired signal and also the possible spectrum of different types of neuronal potentials captured is directly correlated to the coupling coefficient. This important parameter is defined as the ratio between the maximal voltage amplitude of a signal recorded by the device (electrode-amplifier system) and the voltage amplitude of the signal generated across the plasma membrane of a neuron [26]. The low surface area of this electrodes generates a high impedance which is responsible by the characteristic attenuated recordings by this type of MEAs, and also 3D vertical nanoelectrodes [26]. To counteract this, the CC value needs to be high enough such that the recordings of the neuron's

attenuated signals, especially those of low frequency which characterize the "in-cell" aspect of this devices, can be read without being attenuated to the noise levels of the system [40]. Its value varies as a function of the biophysical parameters and the engulfment level, which can be divided into three classes: *(a)* the innate cell biological mechanisms that limit the gMμE-cap diameter that can be totally engulfed by a mammalian neuron; *(b)* The cleft width formed between the neuron's membrane and the surface of the gMμE; *(c)* The size and material-dependent electrical parameters of the gMμE.[40]. Through simulations we can see how the value of this coefficient changes and then apply this information to the fabricate MEAs. Next, the influence of various different parameters on the CC value and signal acquisition is presented.

2.3.5.1 Seal Resistance

The signal-to-noise ratio (SNR) of neuro-electronic hybrids is mainly influenced by the seal resistance formed between the neuron and the sensing element of the electronic device. As previously discussed in section 2.3.4.1, this parameter needs to be sufficiently high to ensure a good CC. A low R_{seal} value permits that a large fraction of the currents generated by propagating APs to be shut into the ionic solution. Indeed, a noticeable improvement was made to this parameter from planar ($1.2 \pm 0.43 M\Omega$) to mushroom (67 $M\Omega$) geometry [42]. Despite almost an order of magnitude improvement, this value is still low for "in-cell" type recordings and the major culprit is that the contacting surface is between the cell and the substrate, which diminishes with smaller mammalian cells. Regarding this, a study by Cohen *et al* demonstrated, using *Aplysia* neurons, that when mechanical pressure was exerted in the axon, it was displaced towards the surface of a planar sensor, increasing the amplitude of recorded FP's. This was most likely caused by the increase in R_{seal} due to increased contact area and possible reduction of the cleft width. Even more interesting was the fact that further increases in the mechanical pressure led to a change of biphasic (extracelullar) recordings of FPs to positive monophasic ("in-cell"), revealing the importance of trying to achieve a high value for this parameter [59]. Regarding gMμEs, Hai *et al* [50] showed the variability of this parameter through recordings using high-density gMμEs MEAs with *Aplysia* neurons. The recordings showed that the APs generated by a single large *Aplysia* neuron coupled to a number of gMμEs with a 20 μm intra-spacing varied in amplitude from $\sim$ 2 to 30 mV, which reflects the variability in

the seal resistance formed between the neuron and various gMμEs [56]. This effect can be observed in Fig. 2.18:

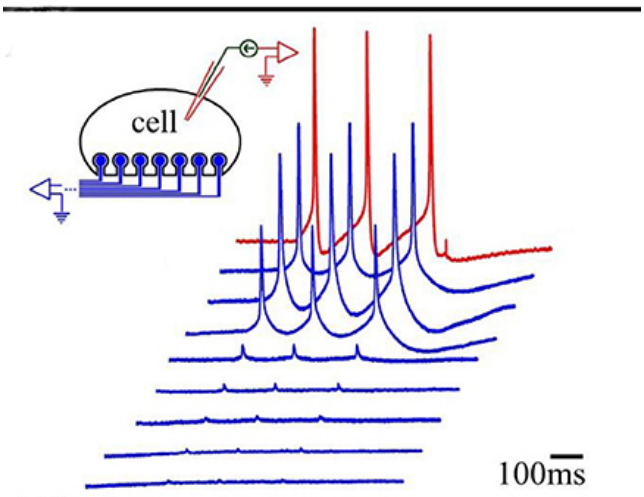

FIGURE 2.18: Differences in the levels of the seal resistance formed between a single *Aplysia* neuron residing on 8 gMμEs (insert) leads to differences in the "IN-CELL" recorded APs amplitudes. A cultured *Aplysia* neuron was intracellularly stimulated to fire 3 consecutive APs (red trace). Simultaneous recordings of these APs by 8 gMμEs (blue traces) revealed differences in the "in-cell" recorded amplitudes. Adapted from [39].

2.3.5.2 Geometry

GMμEs have a characteristic shape which gives origin to their name. They're shaped like mushrooms, being in the category of 3D nano-electrodes, the main difference is on the cap of this structures. Contrary to vertical nano-electrodes, which achieve "in-cell" type recordings in a very limited time window by electroporation (as seen in Section 2.2.1), gMμEs have been reported to form stable neuron-gMμE junctions which kept stability for approximately 2 weeks without alteration of passive or active membrane properties of the neurons and their synaptic functions [50, 56, 60]. Despite this large advantage, the variability on the shape and size of these devices also plays an important role. The variability of these parameters has been studied extensively through simulations by different groups.

A more recent study by Spira *et al*, investigated the effects of the shape and size of the gMμEs on the coupling coefficients. They started by simulating a gMμE with 1 μm high cylindrical stalk, a 0.5 μm high mushroom cap and a cap diameter of 1.5 μm. To evaluate the effects of the geometry on the coupling coefficient, two models of increasing the dimensions of the mushroom electrodes were created. The first one (Model-A)

kept the diameter of the cylinder stalk fixed at constant value while the diameter of the cap increased. The other model (Model-B) increased the diameters of the cylinder stalk and of the cap concomitantly, whilst keeping the cap's diameter always 1 μm larger than the stalk. This method of increasing the size mimics the method used to fabricate the gMμEs seen in the literature [40]. The simulations assumed a homogeneous membrane cleft thickness for the gMμEs (d_j) and were performed for an increasing value of d_j (10, 25 and 100 nm from left to right, respectively in Fig. 2.19).

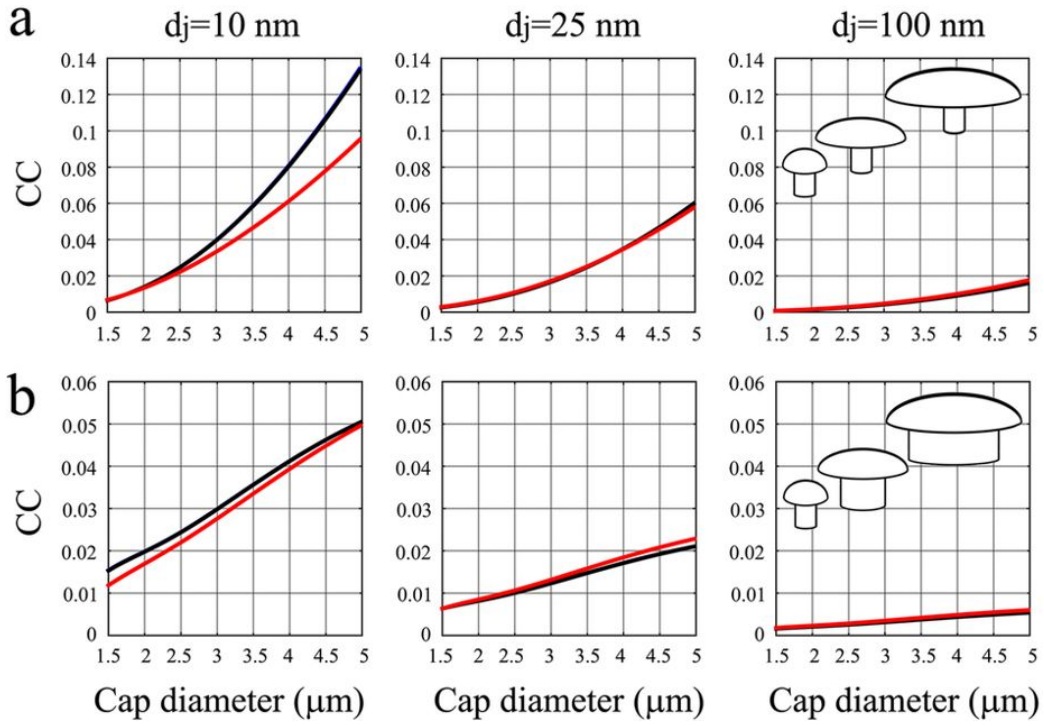

FIGURE 2.19: The electrical coupling coefficient between neurons and gold mushroom shaped microelectrodes (gMμEs) as a function of the mushroom cap diameters. Model-A was used in (**a**), and Model-B in (*b*). The black curves represent membrane (10 Hz) and synaptic potentials (100 Hz), whilst the red curves represent the action potentials (1 kHz), with a junctional membrane resistivity value of 80 Ωcm^2. Adapted from [40].

The first immediate conclusion is that for both models the CC decreased with increasing cleft thickness, as expected. For both models also, the CC increased with increasing cap diameter, althoug this values differ in Model-B with increasing stalk and cap diameter, an overall lower value of the coupling coefficient is obtained in comparison with Model-A. This may induce in a favouring of producing gMμEs with geometries of Model-A, but samples with cap's diameter considerably larger than the stalk may lead to a structure instability. More importantly, it is known that mushroom-shaped caps larger than 2-2.5 μm preclude engulfment by the relatively small mammalian neurons [40]. In Fig. 2.19, observing the values of the coupling coefficient in the range of 1.5 to 2.5 μm, one can

see that they are practically identically for both models or (more notably) even higher for Model-B. More specifically, the maximal simulated CC value expected using favourable theoretical conditions of a totally engulfed gMμE is at best about 2.2% for action potentials (1 kHz frequency), which is sufficient for recordings using intracellular passive nanostructures devices. However, the CC value obtained for sub-threshold potentials (1-100 Hz) is 2.47%, which means it's insufficient for recording synaptic potentials and membrane oscillations with source amplitudes in the range of 1-5 mV, making these signals attenuated to the noise levels of the system or below it. Whilst this size range is the best for optimal neurite coupling of small mammalian neurons, it pays a price by highly limiting the junctional membrane conductance and significantly increasing the impedance and noise level. Coupling this with the fact that a better seal resistance than that formed by a cleft of 10 nm cannot be achieved, Spira *et al* examined the prospects of improving the coupling coefficient by varying the value of the junctional membrane resistance. Furthermore, results of real-life situations of the impact that the size of the gMμEs has on the engulfment level and cleft thickness were also presented. Three sizes of gold mushroom-shaped protruding micro-structures were made with cap diameters of 1.5-2 μm (small), 3-3.5 μm (medium) and 4-5 μm (large). To define the largest gMμEs size that can be engulfed by mammalian neurons, they cultured dissociated 17 DIV rat embryonic hippocampal neurons on matrices of these electrodes. From scanning electron microscope images they were able to estimate the engulfment level and average thickness for the different gMμEs sizes: for the small case a 90% engulfment and (44$\pm$61) nm cleft thickness were reported, for the medium one the values were 31% and (57$\pm$87) nm, and finally for the large one a 24% engulfment level and (22$\pm$54) nm cleft thickness were obtained. This again confirms that the optimal cap diameter of gMμEs for small mammalian neuron must be smaller than 2-2.5 μm.

Another study by Giuseppe Massobrio *et al* [15] investigated the effects of the stalk geometry, more concretely the relationship between its heigh and diameter, by introducing an aspect ratio factor (ARF), defined as $ARF = \frac{h_{stalk}}{d_{stalk}}$.*

In Fig. 2.20 its possible to observe that, by increasing the ARF parameter, the gMμE signal response amplitude increases and approaches the "in-cell" type shape. Also, a linear relation between the ARF parameter and R_{seal} is shown at the right inset. Another interesting result is the relationship between each of the gMμE parts contribution to the

*Assuming a full engulfment; other parameters used can be consulted on [15].

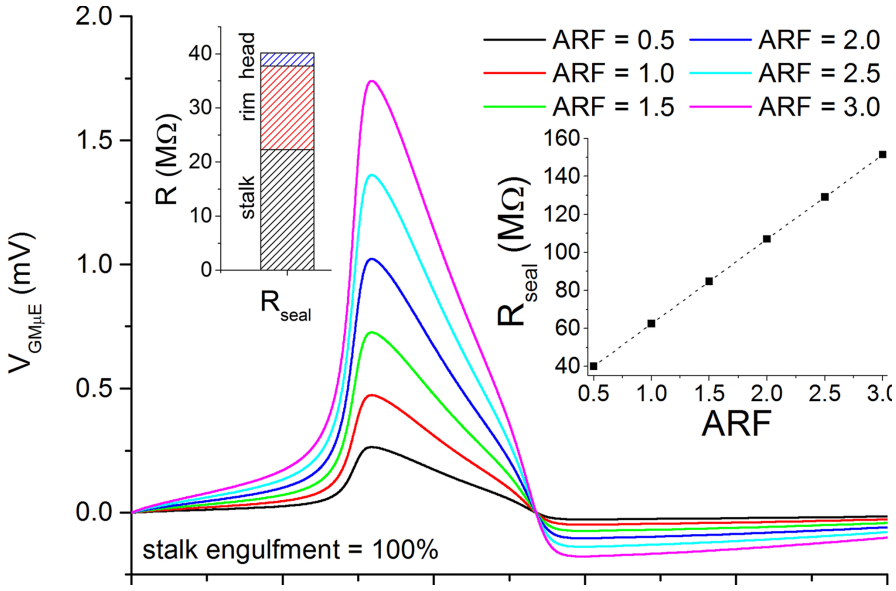

FIGURE 2.20: Simulations showing the influence of the ARF parameter on the gMμE signal. Left inset shows the "weight" of each component of the gMμE R_{seal} under the "reference simulation" conditions. The right inset shows the linear relationship between the ARF parameter and the value of the gMμE R_{seal}. Adapted from [15].

value of R_{seal}, showing that the stalk is responsible for approximately 50% of it's value (left insert of Fig. 2.20).

2.3.5.3 Engulfment Level

One of the known advantages of using these devices is the way they interact with the cells, being engulfed by them and forming a perforated patched clamp-like interface enabling the recording of "in-cell" potentials. However, various papers have shown, through transmission electron microscopy (TEM) images, that a complete engulfment is not always possible, and various factors may contribute to this, such as the geometry of the electrode or the type of cell used. Spira *et al* simulated the impact the engulfment level has on the coupling coefficient value [40]. These calculations were made for gMμE cap diameters of 1.5 and 2.5 μm and stalk diameters of 0.5 and 1.5 μm ,respectively, for different frequencies pertaining membrane oscillations, synaptic potentials and action potentials in two case scenarios of high (80 Ωcm^2) and low (8 Ωcm^2) R_{jm}. Also, for both situations a 25 nm cleft thickness was assumed.

These results are depicted in Fig. 2.21, revealing a rapid decline of the CC value as a function of the electrode surface exposed to the solution. Observing the case for $\leq$ 50% engulfment (dashed black lines) in the high junctional resistance regime ($R_{jm} \sim 1G\Omega$), it is clear it does not enable recordings of any type of signal since the estimated CC is as low as

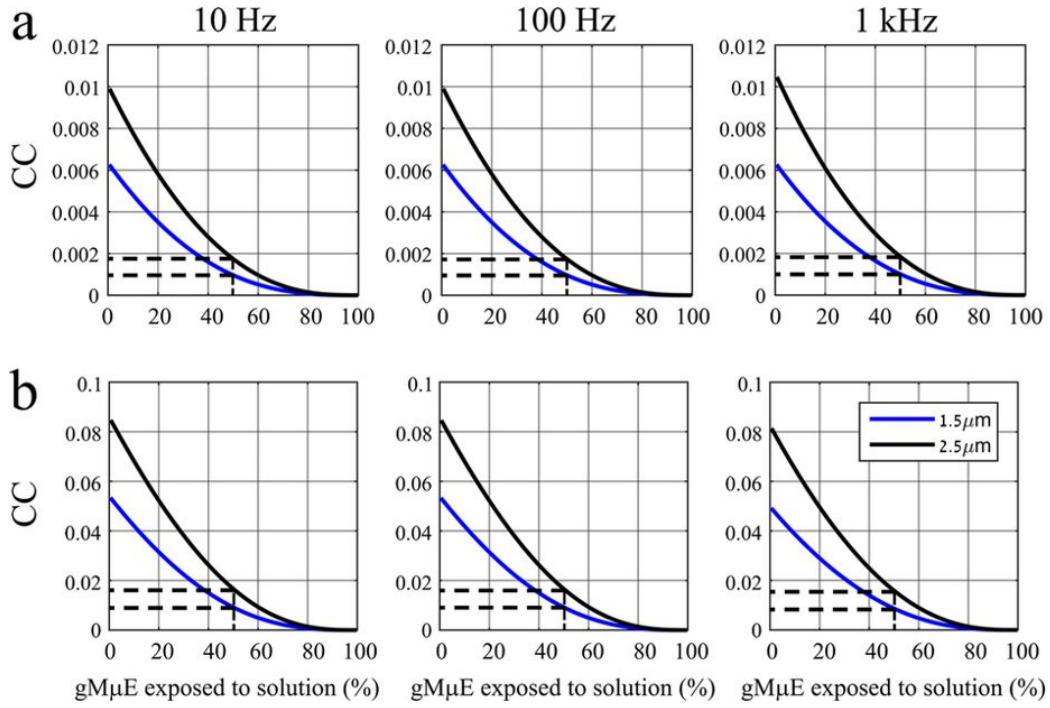

FIGURE 2.21: **CC as a function of the neuron-gMμEs engulfment levels.** The simulation was performed for two case scenarios of (a) high and (b) low junctional resistance. The dashed black lines represent the case of 50% engulfment in each case. Adapted from [40].

0.0001-0.002%. Under identical circumstances, but for the case of low junctional resistance ($R_{jm} \sim 100M\Omega$), the CC value obtained permitted recordings of action potentials, but not of synaptic potentials or membrane oscillations. In another work by G. Massobrio *et al*, they also simulated the impact of the engulfment percentage on the shape and amplitude of recorded signals [15]. In Fig. 2.22 we can see the influence of varying these parameters (assuming an ARF value of 1), demonstrating a linear correspondence between the attenuation of the signal and the area of the exposed electrode.

Another important aspect is that, although a low engulfment lowers significantly the amplitude of the signal, no significant variation in terms of shape is seen, continuing to resemble the intracellular action potential.

2.3.5.4 Junctional Membrane Resistance

Hai *et al* and Spira *et al* have published various paper on this matter [24, 26, 40, 60]. In their first works they studied the impact of R_{seal} and the R_j on the coupling coefficient. For this simulation they used values from direct measurements and calculations of physical parameters that fitted the specific geometry of the gMμEs and the neuron-gMμEs interface. In particular, values for the junctional membrane resistance ranging from 10MΩ to

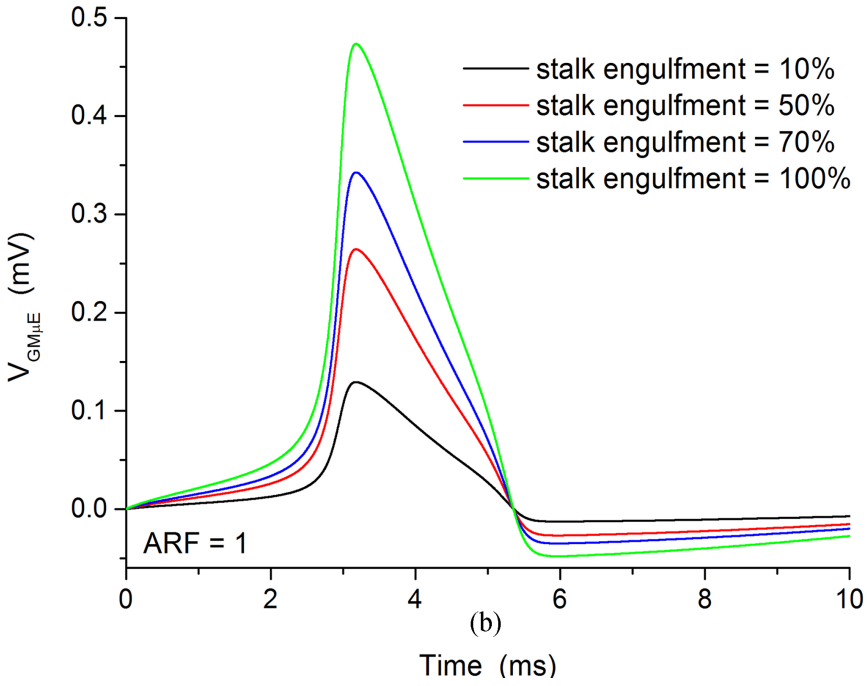

FIGURE 2.22: Simulation results of the signal amplitude by varying the stalk engulfment percentage. Adapted from [15].

100 GΩ and for the seal resistance from 1MΩ to 1GΩ were used [42]. The values obtained from these simulations are depicted in Fig. 2.23. On the left, high frequencies (100 Hz) depict synaptic potentials behaviour, while on the right, low frequencies (1 Hz) simulate membrane oscillation activity.

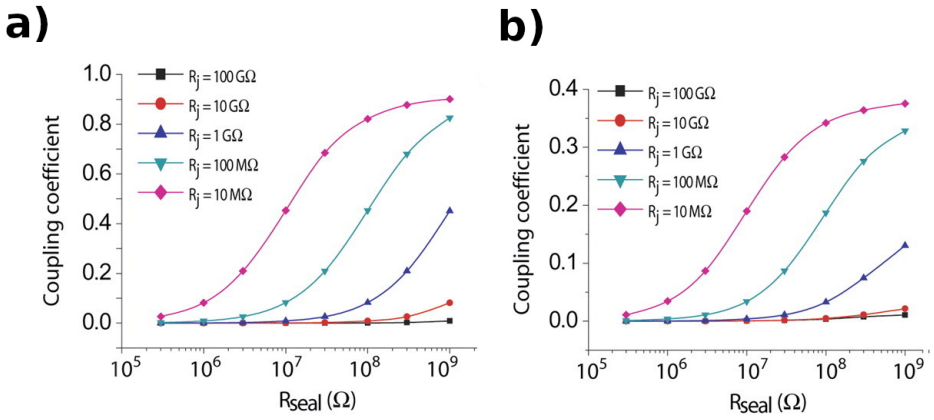

FIGURE 2.23: Simulation of the electrical properties of the interface between a neuron cell and a gMμEs: **(a)** coupling coefficient as a function of the seal resistance for high (100 Hz) and **(b)** low frequencies (1 Hz). Adapted from [50]

It is clear that the coupling coefficient increases with R_{seal} and decreases with R_j. Analysing Fig. 2.23 and focusing on the estimated value of the seal resistance (67 MΩ), for

low frequencies (1Hz) the coupling coefficient increases $\sim$ 20% between the highest value of the junctional resistance ($100G\Omega$) and its lowest value ($10M\Omega$). For higher frequencies (100Hz) the increase is even more notorious reaching $\sim$ 50% increase [50]. It's important to note that calling 100 Hz "high" frequency may induce in the assumption that these simulated signals represent action potentials. It's important to keep in mind that APs are in the range of 1 kHz and the "low" and "high" frequency signals depicted in these simulations represent membrane oscillations and synaptic potentials, which are the type of signals researchers are trying to acquire with MEAs representing the "in-cell" signals. Therefore, these simulations also show how hard it gets to record this type of signals with decreasing frequency.

Using more realistic parameters values as a 25 nm cleft thickness and a fully engulfed electrode cap diameter of 1.5 and 2.5 μm (Model-B), Ojovan *et al* concluded that a R_j value of 100 MΩ was insufficient to record synaptic potentials and membrane oscillations and could hardly couple a 1 mV high synaptic potential. However, lowering the value of R_j from 100 MΩ to 50-80 MΩ was sufficient to increase the CC enough to allow recordings of "in-cell" signals (Fig. 2.24)[40].

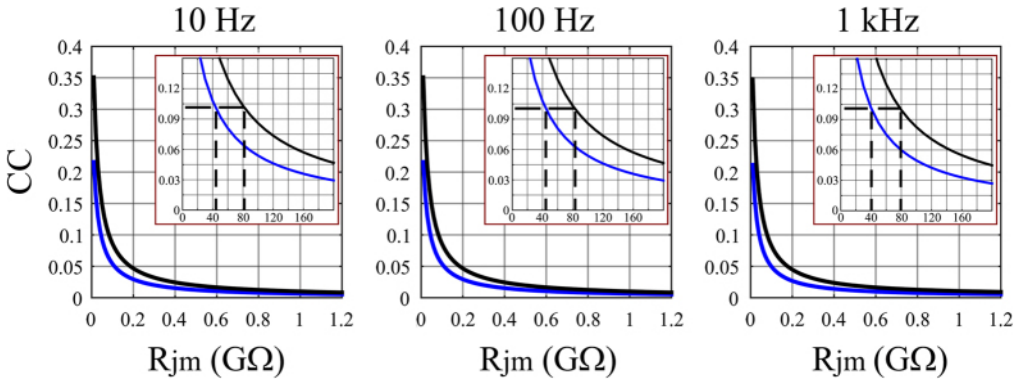

FIGURE 2.24: CC as a function of the junctional membrane resistance (R_{jm}) for gMμEs with cap diameters of 1.5 μm (lower curve, blue) and 2.5 μm (upper curve, black), cleft thickness of 25 nm. Inserts: enlargements of the relationships between the CC and R_{jm} in MΩ. The dashed lines in the inserts indicate that at $R_{jm} \leq$ 40–80$M\Omega$ the CC levels reach values $\leq$ 10%, enabling to record sub-threshold synaptic potentials. Adapted from [40].

The junctional membrane resistance not only modifies the amplitude of the recorded signals, as just shown, but it also modifies their shape. This was demonstrated by Shmoel *et al* through simulations of single action potentials using SPICE [51]. The effects of varying R_j from high to low values is seen from Fig. 2.25 (c) to (g), where the signal's amplitude and it's shape is observed, changing from a biphasic type signal characteristic of extracellular recordings to a positive type signal associated with "in-cell" recordings. It is also

clear that the signal shape using a high R_j value resembles a time derivative of the simulated input AP, as seen by comparing the output signal (red) to the actual time derivative of the input signal (blue). Since an high junction resistance value indicates a loose seal, this element can be approximated to a capacitor [Fig. 2.25 (a)], whilst a low value provides a high CC value and it can be said to be working in an Ohmic regime [Fig. 2.25 (b)].

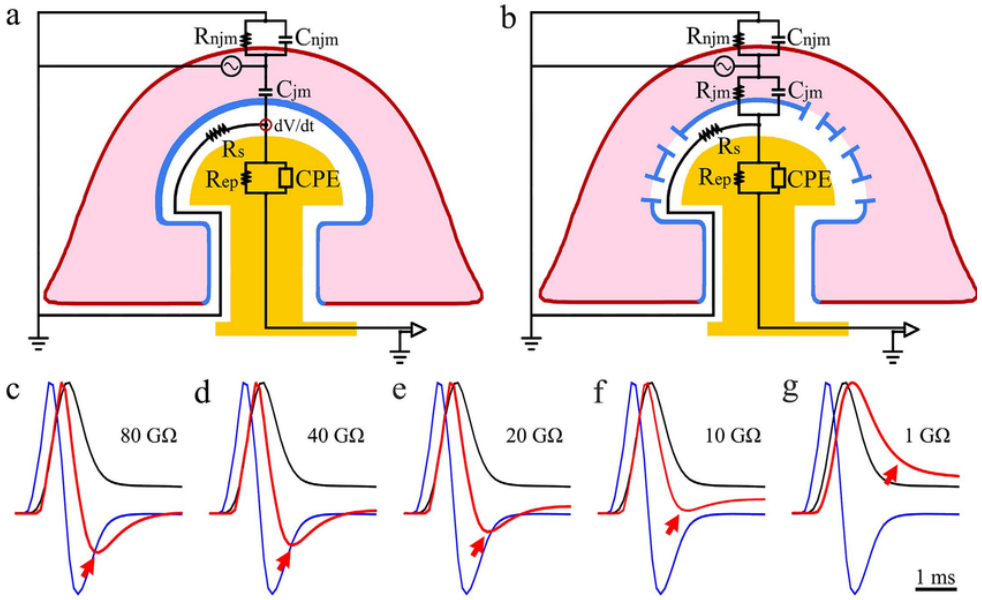

FIGURE 2.25: **The analog electrical circuit of a neuron-gMμE junction, and an estimate of the impact of the junctional membrane properties on the input/output relationship of the junction.** The neuron's (pink) plasma membrane is subdivided into a non-junctional membrane (*njm*, red) that faces the culture medium, and a junctional membrane (*jm*, blue) that faces the electrode **(a,b)**. Both the *njm* and the *jm* are represented by a resistor and capacitor in parallel R_{njm} , C_{njm}, R_{jm} and C_{jm} respectively. The cleft formed between the plasma membrane and the gMμE (white) is represented by a resistor (R_s). The gMμE is represented by a constant phase element (CPE) and a resistor in parallel (R_{ep}). **(c–g)** Simulation of the shape, amplitude, AP width, and AP peak time as a function of the junctional membrane resistance. The normalized input AP (black), its calculated time derivative (blue) and the simulated output (red) for the indicated R_{jm} values 80–1 $G\Omega$. The shape of the output APs (red) changes (red arrow) from being similar to the time derivative of the input AP **(c)**, to an intracellular recording **(f,g)**

In fact, the changes in the relationships between R_{jm} and C_{jm} are expected to generate a continuous spectrum of outputs ranging from extracellular to "in-cell" recording modes as illustrated by the simulation of the analog electrical circuits of Fig. 2.25.

2.3.5.5 Type of neurons

The first studies conducted on gMμEs by Spira *et al* and *Hai et al* used cultured *Aplysia* neurons and vertebrate cell lines in which the cell bodies that engulf the gold mushroom's cap and stalk also tightly adhere to the flat substrate in between the microelectrodes [38, 42].

However, in more recent studies, cultured rat hippocampal neurons have been used [51]. In this case, the dissociated hippocampus cultures extensive growth of branches mechanically interfere with adhesion of the cells to the substrate and also because of the small diameter of hippocampal neuron cell bodies (15–20 μm), the probability of a neuron to be positioned optimally to engulf a gMμE and form a high seal resistance junction is lower than for the large diameter *Aplysia* neurons [26]. This affects the recording signals acquired from this type of neurons, namely the variability in the shapes and amplitudes of the recorded potentials is significantly larger in comparison to cultured *Aplysia* neurons. In Fig. 2.26, recordings of spontaneous activity by 60 gMμE-MEA from cultured hippocampal neurons at 17 DIV show concretely the effects of using these type of cells. The signals ranged from biphasic extracellular FPs with amplitudes of 100 μV to positive monophasic 1-5 mV APs with characteristic features of juxtacellular recordings. It's also possible to observe from these recordings that the signals acquired resemble a time derivative of an input action potential, characteristic of a capacitive regime suggesting that the junctional resistance R_{jm} is high.

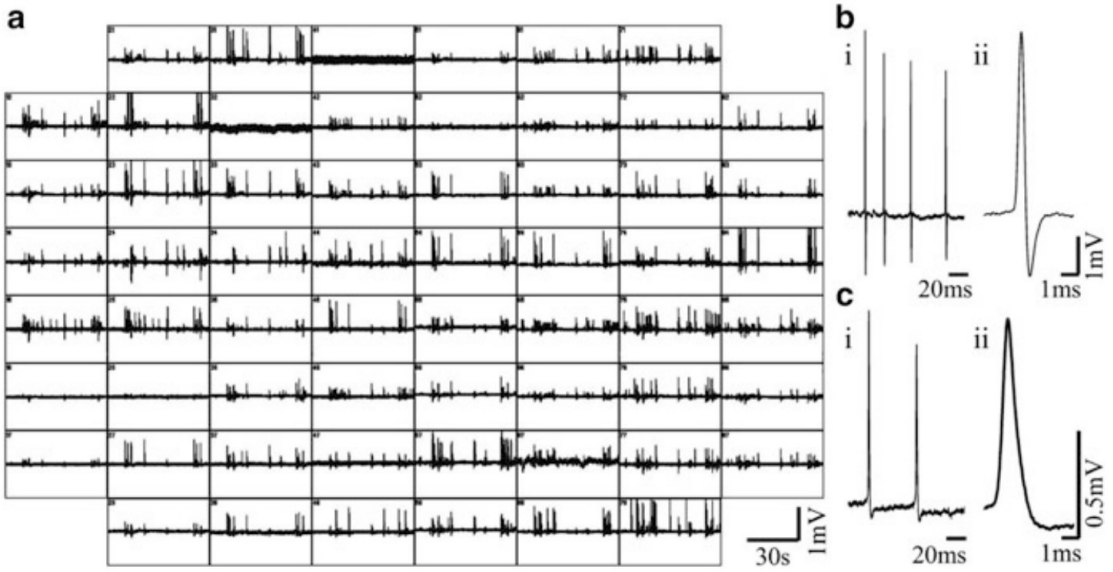

FIGURE 2.26: Spontaneous activity recorded by 60 gMμE MEAs from cultured hippocampal neurons 17 DIV **(a)**; Each box represents 30 s of recording from a single gMμE. Note that the majority of the gMμEs recorded monophasic positive action potentials **(b–c)**; Enlargement of recorded APs by two gMμEs. Whereas in **(b)** the AP features are of loose seal-like configuration, those of (c) are of IN-CELL recordings. Adapted from [51].

In a more recent work by J C Mateus *et al*, the authors recorded the activity of rat cortical neurons at 24 DIV from single-channel gMμEs. Both spontaneous extracellular and intracellular-like firing activity of the cells were also reported [36].

2.3.5.6 Cleft thickness

Optimization of the neuron-gMμE coupling coefficient is intrinsically related to the cleft width formed between the neuron's membrane and the surface of the electrode (that in turn plays an important role on the seal resistance). The value of the cleft width can be obtained by advanced imaging techniques such as transmission electron microscopes and is in the range of 10 to 60 nm for cultured hippocampal neurons of rats [26, 43, 61].

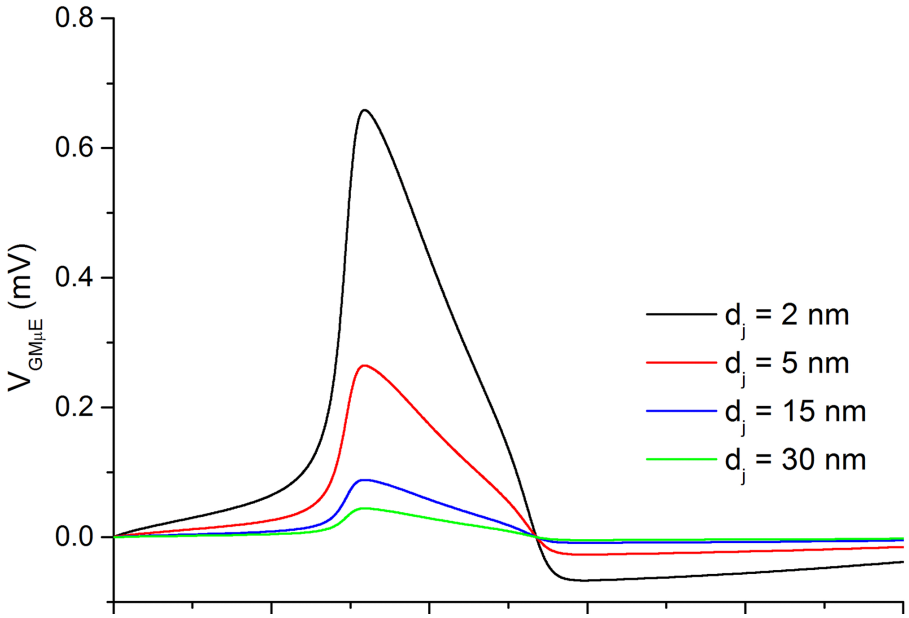

FIGURE 2.27: **Simulations.** Results obtained by sweeping the neuron-to-microelectrode top-surface distance. Adapted from [15]

In Fig. 2.27 we can see a simulation that the impact these parameters have on the recorded signals [15]. By varying the clef thickness from a strong-coupling condition (d_j = 2 nm) to a weak-coupling condition (d_j = 30 nm), demonstrates a great attenuation of the "in-cell" signal, which is caused by a decrease of the value of R_{seal} from 0.10 GΩ to 6.7 MΩ, for the case of strong-coupling to weak-coupling respectively.

2.3.6 Explanations for better CC and reduction of the junctional parameter

Apparently, independent of the precise geometry of the 3D structure but limited by the dimensions and pitch [40], the seal resistance around vertical nanostructures is generated by cell-biological mechanisms that actively engulf 3D vertical nanostructures, yielding almost an order of magnitude larger seal resistances than that observed for planar electrodes (as discussed in section 2.3.5.1). This contributes to the higher coupling coefficient found between the neurons and these type of structures in comparison to the CC of planar

electrodes. However, this fact alone is not sufficient to explain the large increase in the CC value. It is known that in excitable cells, the current generated by a given patch of plasma membrane is limited by the number of active voltage-dependent ion channels embedded in the plasma membrane and that the density of voltage-gated ion channels throughout the plasma membrane is finite [42]. Therefore, using gMμEs which have a considerably smaller surface area in regards to planar electrodes must result in a drastically reduced number of passive ion channels facing the electrode through which current can flow, leading to a high value of the junctional membrane resistance. This creates a paradox between the experimental and the simulated results. As discussed in section 2.3.5.4, the theoretical R_j value derived (in various works) is consistently too high to allow the recording of "in-cell" type signals and greatly attenuating synaptic potentials, in contrast with experimental results. However, when the junctional membrane conductance is increased, sometimes up to 2 orders of magnitude, the simulated results mimic the experimental ones.

If the experimental R_{seal} value is in fact correct, this means that something is missing in the simulation equations to provide the correct value of the junctional membrane resistance. Until now, two possible mechanisms have been proposed to sufficiently attenuate this parameter to match the experimental results: the recruitment of voltage-independent ion channels to the junctional membrane and the formation of nano-holes in the junctional membrane. The first mechanism has two possible explanations. One is the recruitment of voltage-independent ion channels to the junctional membrane by chemical functionalization of the gMμE [50], with peptides (see section 2.3.1.1). This peptides could facilitate the physical contact of the plasma membrane and the electrodes, and the binding of the peptide to receptors on the plasma membrane could lead to structural reorganization of the sub-membrane skeleton. This in turn might be followed by changes in the density and possibly the type of ionic channels at the junctional membrane. The needed recruitment of this type of channels to sufficiently attenuate R_j is relatively low. In fact in [56] a real example is discussed where the recruitment of voltage-independent potassium channels with a channel conductance of 10 to 100 pS to the junctional membrane would only need a concentration of 10-100 channels in the surface area of a gMμE (14 $\mu\ m^2$), this implies a channel density of 0.5 to 10 channels/ $\mu\ m^2$ which as been experimentally documented in a number of cell types [62]. This has also been demonstrated by Massobrio *et al* by

simulating a change in the conductance of voltage-dependent ion channels and also of the leakage-channel density. More specifically, if the potassium ion-channel density is decreased, or the sodium ion-channel density is increased or also if the leakage-channel density is decreased, each one of this situations impacts negatively in the quality of the recorded signal, which changes from monophasic to biphasic (from a ohmic regime to a capacitive one). This can be seen in Fig. 2.28.

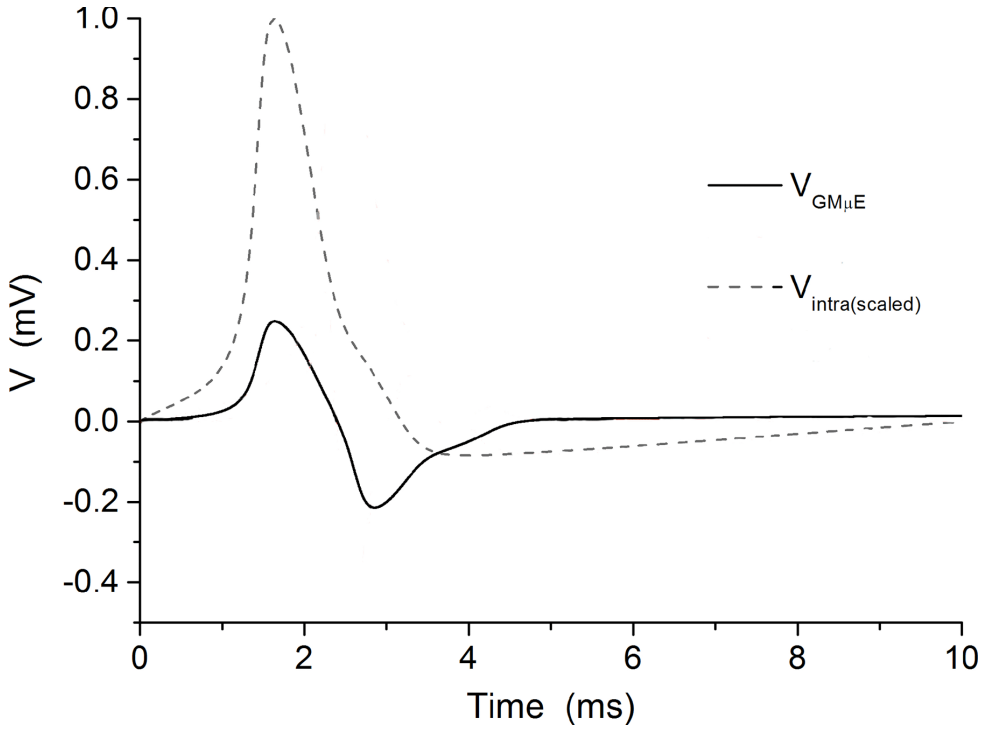

FIGURE 2.28: Simulation of an increase (four times) of the sodium voltage-dependent channel densities leading to a characteristic extracellular type signal. Adapted from [15].

The other explanation is the imposed curving of the plasma membrane around the vertical electrodes. Membrane curvatures have been shown to trigger molecular cascades that could underlie local changes in the expression and density of membrane proteins including ion channels. Until recently, it was known that clathrin-mediated endocytosis produce an inward budding of the plasma membrane, by which cells regulate both the distribution of membrane proteins and the entry of extracellular species. However, it has been shown [63], that the curving of the plasma membrane by external means (i.e. curved electrodes) induces reciprocal regulation of endocytic proteins activity. Moreover, the cytoskeletal element actin was also shown to concentrate around curved membranes [42] and because actin and its associated proteins are involved in diverse cellular functions

these results may suggest that membrane curvature might affect among other cellular processes the recruitment of ion channels.

The second proposed mechanism attributes the attenuation of the junctional membrane resistance to the generation of nano-holes in the junctional membrane due to the curvature of the gMμE [39]. However, this seems more unlikely because the generation of nano-holes on the membrane would lead to cell repair mechanism and this would result in only about an hour of good-quality signal acquisition or even "in-cell" acquisition. Since, after that the acquired signals would be greatly attenuated by the insulation process of the membrane repair mechanism, which goes against the reported stable neuron-gMμE junction of approximately 2 weeks [42, 50, 56].

2.3.7 Recordings of Synaptic Potentials by Gold Mushroom-Shaped MEA

One of the most promising features of the gMμEs is the theoretical possibility of recording synaptic potentials due to their importance to *in vitro* drug screening for the development of personalized medicine [39]. In fact, in 2010, Spira and his team showed the recordings of synaptic potentials [56]. However, in 2014, Weir et al demonstrated that FPs decay to a third of their amplitude within a distance of approximately 100 μm [64]. The decayed FPs have a very similar amplitude and frequency to actual synaptic potentials. Therefore, it is very difficult to distinguish FP's generated by remote neurons from actual synaptic potentials. The most favourable results know to date on this matter were by Shmoel *et al*, that used a pharmacological method to see if the low amplitude signals acquired were indeed synaptic potentials or remote FPs [51]. This was performed by the application of GABAzine, a GABAergic postsynaptic blocking reagent. In Fig. 2.29 we can see the effects that this drug had on the signals acquired. It transformed the firing pattern into discrete regular bursts [Fig:2.29 (f)] and also made disappear the slow negative potentials seen in Fig:2.29 e).

This suggests that the low amplitude potentials recorded are indeed excitatory or inhibitory synaptic potentials. In fact, if the the slow low amplitude potentials had been generated by synchronized bursts of APs generated by remote neuronal clusters, the frequency and amplitude of the negative potentials could have increased rather than disappeared. Although this are promising results, more precise confirmations need to be made.

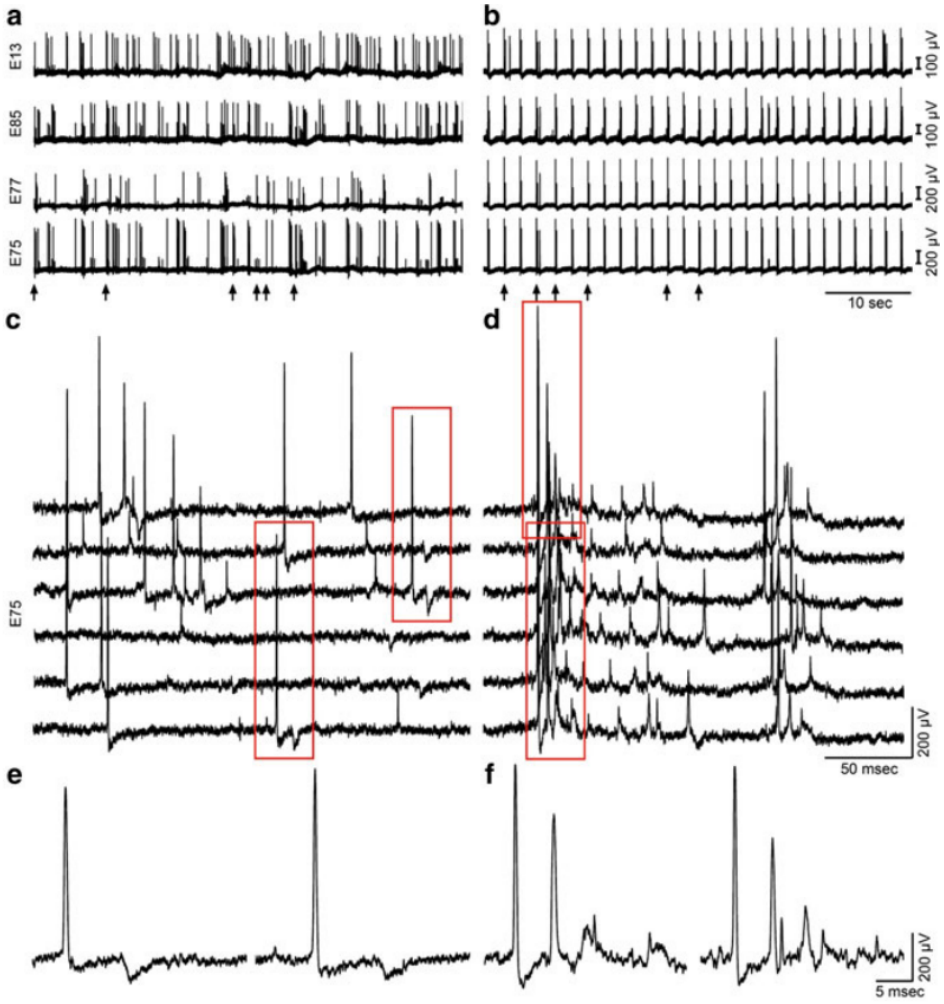

FIGURE 2.29: **The effect of GABAzine on spontaneous spike patterns and the recorded electrophysiological signalling repertoire**. **(a)** Spontaneous firing as recorded by 4 gMμEs from neurons at 19 DIV. **(b)** Recording from the same electrodes 10 min after the application of 10 μM GABAzine to the culture medium. **(c,d)**Enlargements of the bursts indicated by arrows from electrode E75 in **(a,b)** respectively. Note that electrode E75 recorded large and small spikes **(a)**. **(e,f)** Enlargements of the potentials enclosed by red boxes in **(c,d)**, respectively. Note that GABAzine application changed the firing pattern to bursts in which the large and small spikes are more synchronized. **(e)** Low amplitude, long duration negative potentials recorded before GABAzine application. These potentials disappear after GABAzine application, and positive, low amplitude, long duration potentials appear **(f)**. Adapted from [51].

2.4 Microfluidics in cell culture

In 1959 Richard Feynman's *"There's Plenty of Room at the Bottom"* [65] well-know speech, he speaks with wonder about the intricacy that many biological systems, such as cells, have despite their small size. He then, poses the challenge "Consider the possibility that we too can make a thing very small which does what we want – that we can manufacture an object that manoeuvres at that level!" [65]. Since then, this challenge, is ever more

reachable of being attained with the ongoing evolution of tools to manipulate and analyse small volumes of biomolecules such as the DNA. In this work, a compartmentalized PDMS microfluidic structure, which forced cell's unidirectional growth, was integrated in the micro-electrode device developed. The use of microfluidics in neurobiological studies provides a way to mimic the 3D interconnected network of populations of neurons of the human brain through the use of compartmentalized structures, offering a more realistic *in vitro* environment. In this chapter I'll review some of these devices used in cell cultures and more also integrated with microelectrodes which is of the most relevance to the work developed in this thesis.

2.4.1 Microfluidic devices in cell culture

Cell culture's were first conceived as a method to study the behaviour of animal cells at the start of the 1900s by Rose Harrison [66]. Since then, cell cultures evolved to more complex techniques, with use of compartmentalized structures and means of controlling the cells population number and environment, coming a long way from the first ever microfluidic device developed in 1979 by Terry *et al* [67]. This is all possible through the use of microfluidic platforms which involves manipulation of volumes of fluids in the order of 10^{-9} to 10_{-18} L inside channels with dimensions on the order of tens of micrometers [68]. The use of this devices brings various advantages such as, enhanced portability, lower power consumption by minimizing the number of need components and because of enhanced thermal dissipation, improved separation efficiency, less sample and reagent consumption and most importantly separations and detections can be rapidly conducted with high resolution and sensitivity, and cells can be analysed and manipulated with a high degree of spatial and temporal resolution, with control extending even to the level of single cells [69, 70]. With such tools it is possible for a researcher to control the locations of cells in a culture which is of great interest in neuro-biological studies. This confinement can be done in two ways: **(1)** the promotion of selective adhesion to the desired areas on the substrate by laying down a thin adhesive template composed of metal, polymers, or proteins to which the cell preferably adheres, and **(2)** the provision of a physical barrier that confines cells to within an enclosed space [71].

2.4.1.1 Fabrication Methods

The common methods to produce such devices are photolithography and soft lithography which will now be presented. Photolithography involves exposing a substrate coated with a photo-sensitive material, called a photoresist, to light such that the selectively developed regions can be shielded from (or subjected to) subsequent fabrication processes such as etching or deposition. Leaving onto the substrate the patterned exposed via a photomask. This method requires access to a clean-room facility to ensure a even application of photoresist and prevent contamination and also expensive and difficult to operate machines to obtain the desired pattern by exposing and subsequent etching and/or other advanced deposition techniques. The other referenced method, soft lithography, offers a way of producing various replicas through a master support with great ease, rapidity and low costs. This method also have the characteristic that routine access to a cleanroom is not necessary when producing most structures relevant to microfluidics (20-100 mm). However, the reproducible cast must be made first, and it needs the same requirements as the photolithograpy ones. A more in-depth explanation of the common used fabrication procedures follows. As seen in Fig. 2.30, to make the master support a mold most be made first using photolithography. The chosen substrate is typically silicon or glass (which is more affordable) and the chosen photoresist is normally a negative one forming a negative mold. This photoresist is spun in a cleanroom and then the desired pattern is exposed. The required machine to expose it depends on the wanted resolution. After exposure, the photoresist is developed leaving the negative mold on the substrate. Then to cast, an elastomer is poured over the mold, typically it's polydimethylsiloxane (PDMS), filling the regions left open by the mold.

The PDMS must then be cured in an oven, after which it can be peeled of from the mold and cut as desired. Then, the PDMS surface must be treated first to reduce it's hydrophobicity [73] as it will not stick to other surfaces if untreated. Then finally it can be placed in the desired substrate of choice.The choice of this elastomer is based on its mold-release properties and ability to replicate features down to the nanoscale, with low shrinkage during cure (around 1%) and excellent elastic properties, making it the most preferable choice in soft lithography[69]. With the appropriate fabrication methods these devices have become the main choice for creating realistic *in vitro* conditions to study biological applications, of which the neurological ones are of interest in this work. Devices made with PDMS are the most used by experimenters because of the inherent advantages

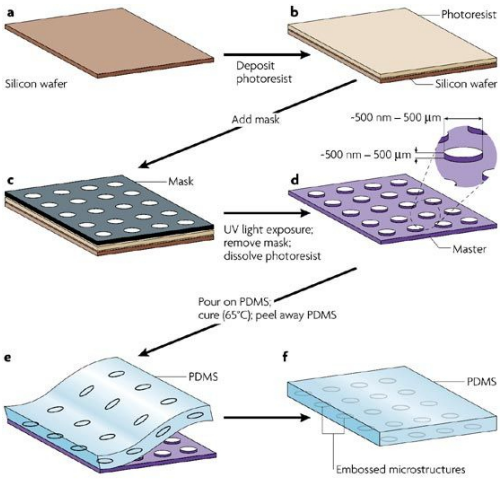

FIGURE 2.30: Schematic representation of PDMS casting using a silicon master mold with features fabricated using photoresist. Taken from [72]

of using a transparent material for microfluidic construction providing ease of optical characterization and stimulation techniques.

2.4.1.2 Neuro-biological Applications

Isolated primary neurons are widely used for experimental investigation and have served an important role in the understanding of mechanisms governing diverse neuronal functions. However, in contrast with other cell types, neurons usually have polarized morphology with distinct cellular compartments (axon, dendrites and soma) that can cover a wide range of scales; and they are also very sensitive to environmental cues, temperature, growth conditions and can alter their behaviour in response to their microenvironment thus making it difficult to achieve results similar to those obtainable from *in vivo* experiments [74]. When working with neurons, another major difficult in culturing is that adult neurons do not undergo cell division [75]. To overcame this challenge two types of cells can be used: immortalized cell lines derived from neuronal tumours or primary cell cultures. The first ones have various advantages such as unlimited proliferation, simpler culturing than primary neuronal cultures and low variability among cultures. However, because they are derived from tumours, they show significantly differences from neurons. As such, it's preferable to use primary cell cultures to best mimic the *in vivo* behaviour of neuronal cells, despite the difficulty of isolating the desired cell type in this cultures [74]. Another unique feature of neurons is that they develop elongated and specialized processes that become highly branched over the course of their development. In the final stage of neuronal polarization (about 7 days from the initial stage), neurons present a fully

mature extended axon and a developed dendritic tree [76]. If this culture is done within a culture plate with an isotropic environment the control of the growth of neurons in a spatially and temporally well-controlled manner is very difficult because the outgrowing features have a random orientation. All these difficulties can be overcome by the use o microfluidic devices where the control of the environment of the cells can be monitored and changed as needed and also through the use of compartmentalization to enable spatial segregation of this neuronal cell features, improving visualization and a more detailed investigation that is otherwise not possible with conventional means.

The first major advancement in using microfluidic devices with multicompartments in neuroscience research was made in 2003 by Taylor *et al* [77] using soft lithography. The device purpose is to separate the somata from the axons via the physical partition separating the two chambers in the PDMS device as seen in Fig. 2.31 a). The bottom of the barrier that isolates the chambers as 120 micro-sized grooves, which were uniformly spaced apart to prevent any structural collapsing on assembly. The embryonic neurons placed in the growth compartment were seen extending through the groves and into the adjacent compartments, within 4 days. The separation of the somata and axon parts was demonstrated by using hydrostatic pressure from adding a slightly higher volume to one chamber than the other, inducing a slow unidirectional laminar flow through the microchannels. The same lab later published a protocol for the fabrication of this type of devices [78], and this protocol has been widely used in studies employing microfluidic neuronal culture as well as with commercial versions available [Fig. 2.31 b)] [70].

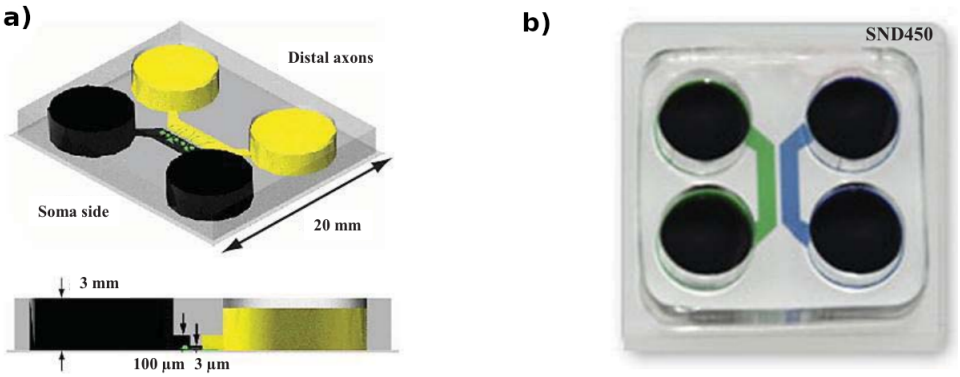

FIGURE 2.31: **(a)** Schematic of a two chamber compartmentalized microfluidic device; **(b)** Commercial Microfluidic Compartmentalized chamber (Xona Microfluidics LLC). Adapted from [76]

As mentioned above, the ability to control to size of the micrufluidic channels permits the experimenters to separate somata from axon. This is possible because of the

dimensions of this cells, in mammals soma cells tend to to be on the order of tens of micrometers in diameter, whereas axons are approximately 1 micrometer in diameter or even smaller [77]. The control and separation of neuron cultures is of great importance to study the effect of drugs and neurodegenartive diseases. Since the first compartmentalized microfluidic device designed by Taylor *et al*, many variations have sprouted from this fundamental design with the appropriate modifications depending on the aims of the study in question. Some of these variations are; three or more chamber designs, circular layouts, growth oriented layouts, and most importantly devices containing electrodes which will discuss in more detail now [76].

2.4.2 Microfluidic devices containing microelectrodes

A microfluidic-microelectrode (μEF) device is a device consisting of a microfluidic platform integrated with a MEA such that the microchannels of the micrufluidic device platform align with the rows of microelectrodes. The use of such devices brought great advances in the study of extracellular axonal potentials, for two main reason. First, the physical constraints imposed by the platform and any substrate patterning that is performed enable the isolation and targeting of individual axonal populations with low numbers of axons and ensures the axons are sufficiently close to the electrodes to record extracellular signals. Second, the small size of the microchannel causes the conductance inside the channel to be very low and thus amplifies the extracellular voltage signal received by the recording electrodes [79]. This signal amplification is crucial to permit the measurement from axons using traditional micro-electrodes (i.e. planar MEA's), as this signals tend to be very low due to the poor coupling between axon-electron contact. The mechanism underlying this phenomena has been studied and even modelled, and will be now briefly discussed.

2.4.2.1 Circuit model of an axon enclosed in a microchannel

In a 2008 paper, FitzGerald *et al* [80], presented an explanation for the mechanism of this signal amplification as well as modelling and simulating it. In Fig. 2.32, a scheme of circuit model of an mylenated axon enclosed in a microchannel is seen. The propagation of an AP can be considered as the successive depolarization of adjacent nodes in a mylenated axon, as seen in Fig. 2.32. This circuit model is very similar to the cable model discussed previously with the inclusion of the extracellular resistance R_{ecf}. As such, it holds true for

unmyelanted axons. However to simulate each type of axons, different parameters must be used: Modified Hodgkin-Huxley model and Sweeney model; for the unmyelanted and myelanted axon. The membrane potential V_m is defined as $V_m = V_{in} - V_{out}$. In the propagation of an AP, the membrane potential differs along the axon as shown in the figure, meaning the potentials inside and outside of the cell also vary spatially. This membrane potential difference is quantified as $\delta V_m = \delta V_{in} - \delta V_{out}$, taking into account the internal and external potentials. In the loop between the depolarized and resting nodes (the left and right nodes in Fig. 2.32, respectively), the currents through the extracellular (culture medium) and axonal resistances R_{ecf} and R_{axon} are equal in magnitude, and thus the differences in the internal and external potentials at the two nodes of the cell can be accounted for as drops across these resistances: $\delta V_{out} = iR_{out}$ and $\delta V_{in} = iR_{in}$. This yields the relationship between the changes in the internal and external potentials that occur during the propagation of an AP for both neuron types as [80]

$$\frac{\delta V_{out}}{\delta V_{in}} = -\frac{R_{out}}{R_{in}} \tag{2.17}$$

From the equations described above, changes in the external potential seen by a recording electrode can be increased by increasing the extracellular resistance, which can be achieved in the *in vitro* case by either increasing the resistivity of the culture medium or reducing the volume of the medium. The former option is possible by changing the composition of the medium, but this would also impact the culture conditions.

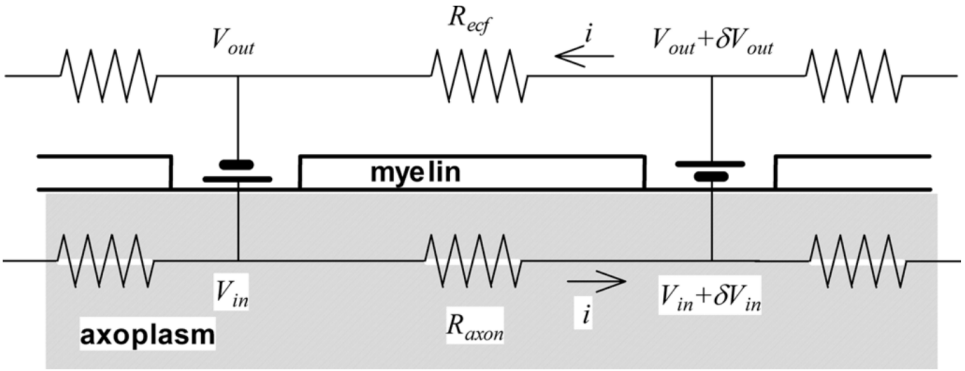

FIGURE 2.32: Local currents during depolarization of an axonal membrane. Reproduced from [80]

Thus, the confinement of axons in microtunnels in a μEF device is a simple and effective method of increasing the recorded extracellular potential. FitzGerald *et al* also

showed important differences between the two types of neurons through their simulations; for unmyelinated axons, the extracellular potential during AP propagation is amplified roughly uniformly throughout the microchannel except near the entrances; that is, the amplitudes of the spikes recorded by electrodes within a microchannel would be uniform along the length of the microchannel except those positioned near the ends of the microchannel. Wang *et al* [81] have described this phenomenon, which they call the phase-cancelling effect, in more detail. Also in unmyelinated axons the propagation velocity of an AP was proved to be much slower and thus stretching in space much less in comparison to an myelinated axon. More importantly to the work on this thesis, it as also proved that for myelinated axons the amplitude V_{out} changes smoothly along the microfluidic channel with no evidence of dependence on position with respect to nodes of Ranviers. Thus, using a microchannel structures frees experimenters from the need to bind the axon to the electrode and worrying about placing the electrodes near a node of Ranvier. To support the simulations done in this papers, there are also experimental studies done with μEF devices. For example, Pan *et al* [82], demonstrated that the impedance of the recording electrodes beneath the axons in the microchannels of their μEF device increased as the culture matured and more axons grew through the tunnels up to 14 DIV; this increase in impedance was correlated with an increase in the amplitude of the recorded spike. More concretely, they measured the spikes amplitudes for the microchanells to be generally in the range of 1-3 mV, whilst the ones recorded in culture chambers were generally less than 50 μV. Another important aspect of their experiment was that the signal-to-noise ratio in the microchannels were significantly higher (450) than the one in the chambers (80). As such, the increase SNR and amplification of μEF devices can bring even bigger advantages to neuro-biology when the electrodes used are gold-mushrooms. Another experiment done by Habibey *et al*, where PDMS tunnels were attached on top of an high-density MEA (HD-MEA) with cortical neurons cultured on each side of the tunnels (see Fig. 2.33), demonstrated that the recording of spontaneous activities from axonal signals were amplified by a factor of 20-150 [83].

2.4.3 Axon velocity propagation

μEF devices have been used to measure the propagation velocity of APs travelling along axons in culture. This is done by positioning multiple electrodes along the microchannels through which the axons grow and calculating the propagation velocity from the arrival

times of spikes determined to be from the same AP recorded at each electrode and the distance between the electrodes. As discussed above, increasing the extracellular resistance leads to an increase of the recorded extracellular potential. However, FitzGerald *et al* also showed through their simulations that this extracelullar resistance increase is expected to produce a decrease in the conduction velocity due to the decrease in the length constant [80]. More specifically a general decrease of 5% and 1% for myelinated and unmyelinated axons, respectively. As such, this can bring disadvantages when trying to build *in-vitro* networks of neurons. Indeed some studies done with μEF devices proved the aforementioned results on the slowing of the AP's propagation velocities along the microchannel [84, 85]. However, this studies were done with young axons at a few days *in vitro*. Interestingly, in more recent experiments, Habibey *et al* demonstrated that increasing culture age is correlated with an increase in both activity level and propagation velocity. The set-up used in their experiment is shown in Fig. 2.33. Their results indicate that older cultured neurons (95 DIV) are associated with a increase in conduction velocity and also that burst activity is correlated with it. Another study supporting the increase of conduction velocity with culture age was done by Hong *et al* [86]. In their study they took measurements between 9 and 28 DIV, where they also determined an increase of the propagation velocity with the culture age.

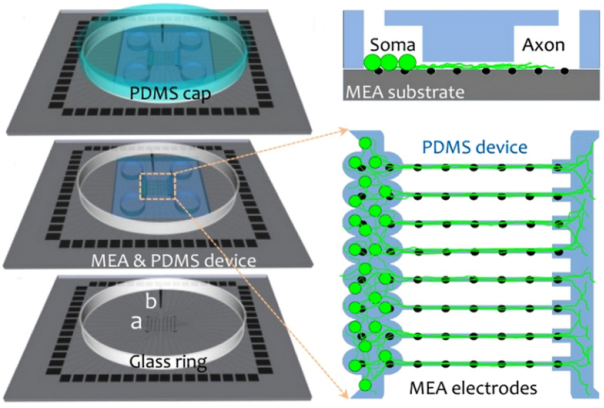

FIGURE 2.33: Illustrative example of a μEF device. **(a)** Schematic of PDMS device mounted on a 60-electrode MEA chip. The somata are localized in the somal culture chamber, and the axons extend through the microchannels to the axonal compartment. MEA electrodes are regularly spaced beneath the microchannels. Adapted from [83]

2.4.3.1 Axonal guidance

As discussed previously, Taylor *et al* [77], was the first to prove the capability of using μEF devices to control the growth direction of cultured neuron's axons or dendrites. The

importance of this is tremendous when trying to replicate the brains complex systems *in vitro*. Sporns *et al* [87] have shown that among the connectomes of primates, regular and small (3, 4 or 5 nodes) structural motifs* form characteristic network building blocks that, when assembled computationally, resemble real brain networks, including small-world attributes. Other works also support the idea that information processing circuits are organized in this modular, node-based structures that exhibit adaptive intra-network and inter-network functional connectivity [88]. To create this networks using *in-vitro* cultured neurons, one has to have control over the connection between this population of neurons. This can be achieve by surface modification, or by 3D structural confinements. Using the latter option, one can aim for reproducibility testing by directing the structural motif and connectivity of a network, achieving higher fidelity of signal transmission of evoked network responses. The problem with creating this type of μEF devices is that the probability of a fully successful network decreases with increasing number of nodes. As such, the need of finding a 3D pattern that counteracts this phenomena is of great importance. In 2018 Forró *et al* [88], published a paper addressing the above mentioned problems. In their work they tested 10 different channel geometries from previous reports in the literature scaled down to smaller sized nodes and also several novel designs, where the preferred growth direction is from right to left, which can be seen in Fig. 2.34 a).

From this 10 types, the Arches and Stomachs rely on the tendency of axons to avoid following sharp turning angles. The Arches, Kites and Side-Kite structures were taken from previously investigated works and were included to test against the novel designs, more specifically the Stomachs one's. Other channels are stochastic in nature in that they rely on a higher probability for a particular axon to choose a forward leading path than backwards. Finally, straight channels were included as a comparison benchmark. To test their efficacy, PDMS structures of this different geometries were separating chambers were placed on top of the channels and fluorescent protein encoding adeno-associated viruses (AAV) were delivered selectively; alternating between red and green fluorescence for consecutive chambers. This provided the ability to visually distinguish between backward and forward growing axons (Fig. 2.34 b)) The trials were performed at 6, 12 and 18 DIV and were analysed by a trained convolutional neural network which segmented data into red and green axons and cell bodies. The results are presented in Fig. 2.35, where median growth (forward and backward) is plotted for various DIV for every channel.

*All networks, including biological ones, can be represented as graphs, which include a variety of sub-graphs. Network motifs are sub-graphs that repeat themselves in a specific network

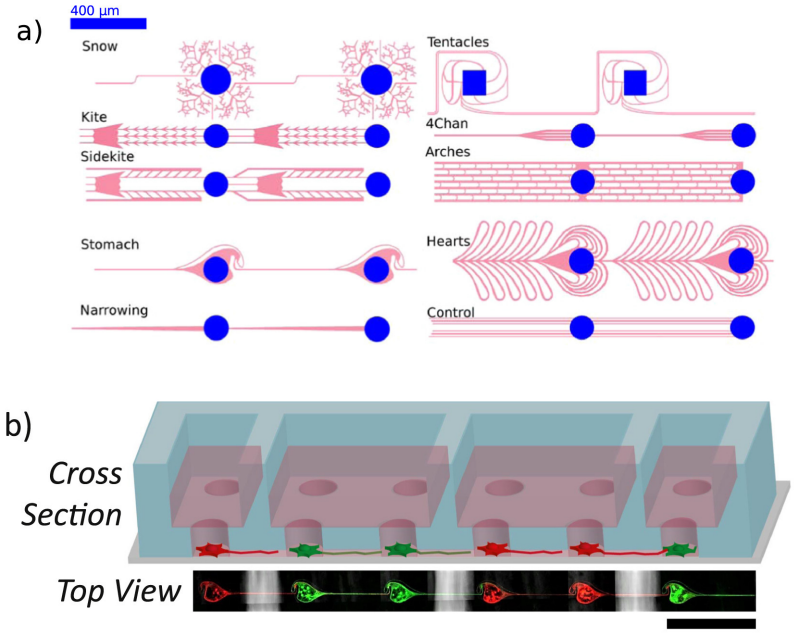

FIGURE 2.34: **(a)** The 10 different PDMS channel structures investigated. Neurons can only land into the blue compartments. The channels (red) are shallow (4 μm) so that cell bodies cannot move into them. The preferred growth direction is expected to be from right to left; **(b)** PDMS microstructures of different architectures with separating compartments, were hippocampal neurons expressing either red or green fluorescent proteins were seed into alternating compartments to provide a better visualization of the axon guidance. Adapted from [88]

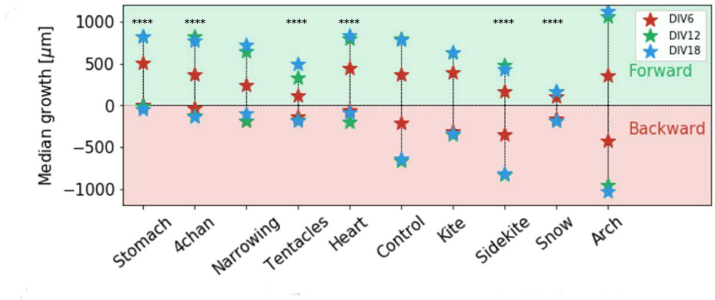

FIGURE 2.35: **Median growth forward and backward.** Stomachs had the least backwards growth. Every datapoint is a median evaluated over more than 160 replicas. Adapted from [88]

From this data, the most successful channel design is the Stomach one, due to causing consistently the shortest backwards growth and comparable forward growth in relation to other structures. This structure type far exceed previous reported results, achieving a 95 % proportion of forward-only connecting structures at 12 DIV, where in other reports the efficiency rarely exceed 60-80% and deterioration started to appear at 10 DIV. Also remarkable, was that at 18 DIV the percentage dropped only to 83%, which is important given that mammalian neurons are typically more active at later dates *in vitro*, as discussed above.

2.4.3.2 Study of specific diseases

Most studies to date have served to demonstrate the concept of compartmentalization, although there have been some which have demonstrated directly the utility of compartmentalized devices for the study of neuropsychiatric disorders. The prime attribute of neurodegenerative diseases such as Alzheimer's and Parkinson's has been defect in axonal transportation and/or synaptic deficits due to aggregation of extracellular amyloid plaque, or intracellular neurofibrillary tangles or Lewy bodies [89]. The use of traditional culture dish is not suitable for studying these mechanisms given the random orientation of the axons, overlapping synapse formation and difficulty in recovering the axonal material for analysis. Compartmentalized microfluidic devices enable localization of individual neuron with spatial segregation of the soma and growing axons, as well as limited background noise from other neurons which coupled with a powerful imaging system it has been possible to study axonal trafficking. Modifying the original two channel compartment design initially developed by Taylor group [77], other groups have demonstrated single-molecule imaging of retrograde axonal transport of NGF [90] and dendrite-to-nucleus signalling of BDNF [91, 92]. More recently, such compartmentalized devices have also been used to investigate the defects in axonal transportation caused by the two pathophysiological molecules β-amyloid peptide (Aβ) and Tau protein, crucial to the study of Huntington's Disease [93, 94]. There have been also studies done with μEF devices where they can cause chemical [95] or physical injury [96] to the growing neurons and as such study central or peripheral nervous system injuries. All this studies highlight the key experimental approaches that would be difficult or impossible in non-compartmentalized devices.

2.5 PEDOT

In efforts to achieve ideal microelectrode properties, research has been invested in electrode modification with conducting polymers (CPs). Conductive polymer coatings can be used to modify traditional electrode recording sites with the intent of improving the long-term performance of cortical microelectrodes. This polymers can drastically decrease recording site impedance, which in turn is hypothesized to reduce thermal noise and signal loss through shunt pathways [97]. The most common biocompatible conductive polymer used for neural interfaces is Poly(3,4-ethylenedioxythiophene) or PEDOT, which is

the most electrochemically stable [98]. Conductive polymers generally have lower conductivity than most metals, but other advantageous properties make them popular for coating electrode sites. PEDOT has an extremely large conductivity, which means that it can reasonably be referred to as a synthetic metal, and is also being used as an electrode in electrolytic capacitors. Its large hole mobility means that it can be used as a hole-injection layer at an anode, or even a synthetic anode itself [99]. However, PEDOT itself is insoluble in water and therefore of limited use due to the difficulty of processing such polymer. To overcome this, the synthesis usually takes place with polystyrene sulfonic acid (PSS) to ensure solubility in water [100]. The hydrophobic PEDOT molecules have a tendency to aggregate and so the surrounding polystyrene sulfonic acid stabilizes the dispersion and creates a solid colloid dispersed in water. The addition of the PSS to the PEDOT polymer, decreases the overall conductivity of the compound (although it remains much higher in comparison to metals) and also induces an anisotropic effect on the conductivity, where the lateral conductivity is three times higher than the vertical conductivity [101]. This difference is due to film morphology, as PEDOT - rich particles, of about 20-25 nm in 23 diameter and 5-6 nm in height, are separated by PSS lamellas, which have weak electrical conduction.

2.5.1 Synthesis of PEDOT:PSS

There are two main types of synthetic routes of PEDOT:PSS; chemical polymerization and electrochemical polymerization – both initiate an oxidation reaction of the monomer EDOT. Both have been widely used in biomedical applications, and the application often dictates the choice of fabrication method. Electrochemical polymerization and deposition occur simultaneously, whereas chemically-polymerized PEDOT:PSS results in a aqueous dispersion, which can be deposited in a great variety of ways. The chemical approach is more expensive, because it needs additional compounds to oxidise the EDOT and more laborious; the solution needs to me filtered and the resulting PEDOT:PSS then needs to be applied to the substrate by spin coating or electrochemical deposition. The method adopted in this work was the electrochemical polymerization, thus will review this method here.

2.5.1.1 Electrochemical Approach

Electrochemical polymerization is an easy and fast technique for depositing PEDOT:PSS on conductive surfaces such as gold. It also allows selective deposition on specific areas where a metallic film is present. This a convenient method to pattern PEDOT:PSS, as opposed to multi-step photolithographic techniques, but also requires a conductive substrate, which can limit its use in some devices. This process is typically performed in an electrochemical cell with a three-electrode configuration. A working electrode, reference electrode and counter electrode are submersed in a solution of the monomer EDOT and PSS in deionized water. EDOT monomers are oxidized by the metal electrode and form a cation. These cations combine together to form oligomers which form long chains of carbon-carbon bonds of monomers. During the reaction, the monomers are first converted into activated radical cations. These activated species react with each other and with other oligomers, increasing the molecular weight and as the reaction continues, the higher order oligomers become more and more insoluble, and the PEDOT product is precipitated onto the working electrode (cathode) [101, 102] (Fig. 2.36. Polymerization can be

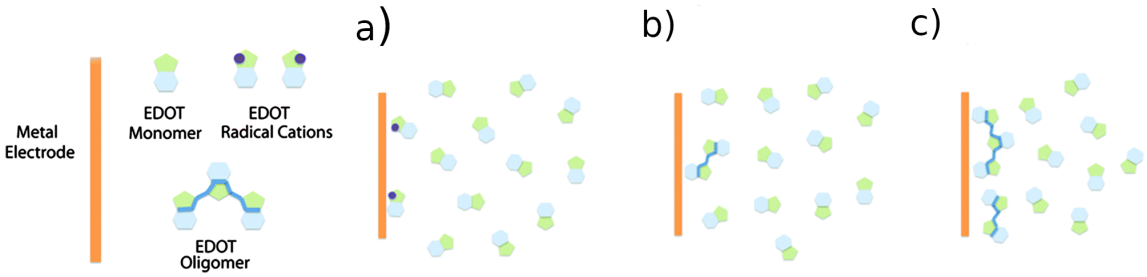

FIGURE 2.36: **EDOT polymerization.** Electrical polymerization process (a); The metal electrode oxidises the EDOT monomers creating radical cations (b); These radical cations combine, creating dimers, trimers, and higher oligomers (c); As the molecular weight of the polymer chains increase they become insoluble, precipitating onto the metal electrode surface. Adapted from [103]

done in potentiostatic (constant potential), galvanostatic (constant current) or potentiodynamic modes.

2.5.2 Advantages

The main advantages of incorporating CPs into MEAs is the improvement of charge storage capacity and the reduction of microelectrode impedance. The last one is of greatest important to overcome the current limitation of increasing impedance of microelectrodes with decreasing diameter and was put to test by Bartsch *et al* recently [103]. In their work

they tested the possible advantages of the impedance change on thick PEDOT film microelectrodes with diameters below 250 μm. This is work is very relevant because until then previous works only focused on electrodes with large areas, leaving to question the capability of miniaturization of PEDOT electrodes. Bartsch *et al* reported astounding result of impedance decrease in relation to same diameter gold-electrodes. The PEDOT coating also offer a more rough surface structure which in turn is assumed to increase the effective electrode are contributing to this decrease.

Other advantages of using PEDOT films is the improvement of charge storage capacity (CSC) and charge injection limits (CIL); producing recording electrodes with high SNR and more effective stimulating electrodes [104].

Electrodeposition of CPs can also control corrosion. PEDOT is especially promising due to its stability in oxygen-rich, hydrated environments, since oxidation further polymerizes the CP rather than corroding the metal [98]. Coating thickness is also an important consideration, with thicker PEDOT coatings displaying lower impedance measurements on average compared to thinner coatings. Of great importance, in particular to neuronal recordings, is that PEDOT:PSS coatings are known to dramatically decrease the impedance of metallic electrodes, especially the low frequency [1-500Hz] range (by 2 orders of magnitude) [105, 106].

The versatility of CPs is evident in many reports as they can be doped with various counter ions, including biological moieties, to improve cellular compatibility and neuronal recording [107]. For example, different dopants used with PEDOT can influence the final impedance results. Mandal et al. showed PEDOT doped with tetrafluoroborate ($BF4_{-}$) had impedance approximately one order of magnitude lower than PEDOT:PSS electrode coatings at 1 kHz (which is the typically frequency used for acquiring neuronal activity) [108].

Future work surrounding CP coatings should be carried out with a focus on improving long term *in vivo* stability, which remains a limiting factor for implantable MEA systems.

Chapter 3

Fabrication of microfluidic neuronal networks of defined functional connectivity

In this thesis, two different microfluidic neuronal networks of defined functional connectivity were fabricated. Both designs have a common characteristic; two distinct layers of different thicknesses. As such, the method adopted to produce these features was the "single developing step". This method uses multiple coating and exposure steps with a single developing step, which allows for low cost rapid prototyping of microfluidic devices. In this work, only two SU-8 layers were needed. However, using this method it is possible to process various layers as reported in the literature [109, 110], demonstrating its usefulness to produce complex multi-level microstructures that may be difficult to achieve by coating SU-8 layers over existing high-aspect-ratio topographies. In the next two sections, the optimization processes needed and the problems and subsequent solutions of the lithography steps will be discussed. Because the two designs are fabricated using the same SU-8 type layers and have identical thicknesses, these two first sections are valid for both designs (except when mentioned).

3.1 Microfluidic Designs

The microfluidic channels here replicated have the same principle of work: separation of the cell body from its dendrites or axons. This is possible by utilizing layers with different thickness, where at least one of these layers is made such that it's thickness (4-15 μm)

only allows for dendrite or axonal propagation. An example of such segregation can be observed in Fig. 3.1.

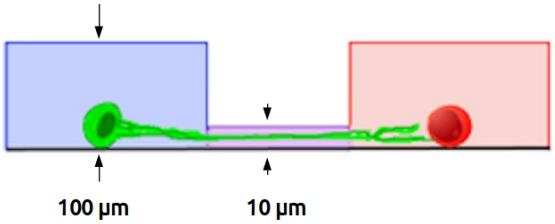

FIGURE 3.1: Representation of a microfluidic device for cell morphology guiding. Adapted from [76]

3.1.1 uEF Chamber

This microfluidic design was the first of its kind to be made to study axonal growth, as it is detailed in section 2.4.1.2. It is design to have a large area where the neuron cells will be deposited, as depicted in Fig. 3.2 (a), once deposited the cells will follow the paths leading to the center of the structure where they will encounter the micro-channels. In this area, the thickness of the structure reduces by a factor of ten, which only allow axons to pass through these channels onto the other side, whilst the body of the cell stays in the other due to its dimensions. The design used in this study was modified slightly to compensate the tolerance associated when choosing the WSP (Writing starting point) for the second layer. The reason was that, in contrary to the Stomach design, where the area to be exposed is very minute in comparison to the substrate, in this case its size is very large and takes almost the entire width of the substrate. Therefore, it was not possible to use the method described later in the stomach design (section 3.4.2.5), so to compensate, we overshoot the length and number of the axon guiding channels of layer 1. Our design can be seen in Fig. 3.2 (a). It is important to note that it is not prudent to use a DWS machine to expose this type of design with large features, as it takes a considerate amount of time to write. Such design should be made with a projection lithography tool. Nevertheless, it was a good starting point to ease our way to make the microfluidic stomach structure. A image of the produce μEF Chamber design can be seen in Fig. 3.2 (b).

3.1.2 Stomach Design

The stomach design which was discussed in section 2.4.3.1, is a much more complex design than the common compartmentalized chamber design. Nevertheless, the concept is

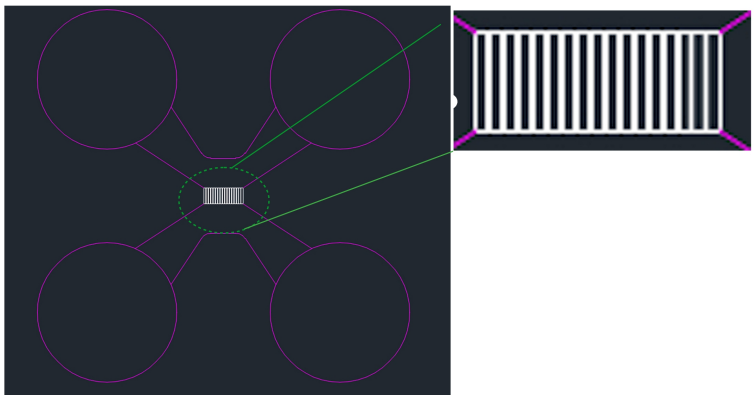

(A) Complete CAD design. The inset shows the zoomed view of layer 1

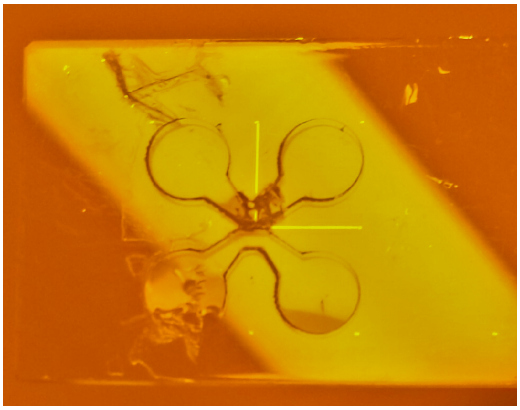

(B) Final result of the lithography process.

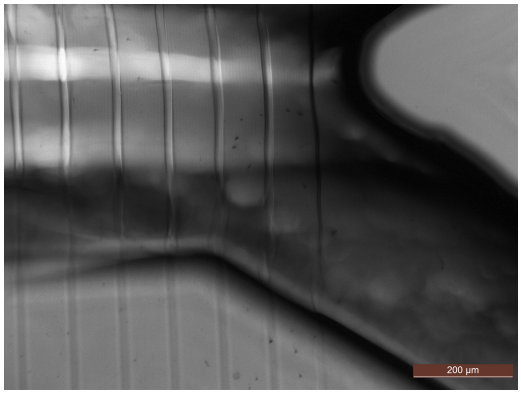

(C) Microscope view of the micro-channels

FIGURE 3.2: **μEF chamber design** (a) The complete CAD of the μEF chamber design, (b) the reproduced pattern in the photoresist and a (c) microscope view of the micro-channels region

similar to the μEF design for the growing and guidance of axons. In this case the cells are deposited in the pillars seen in Fig. 3.3 c) which lie at the center of each stomach structure. The area outside this pillars is much thinner and therefore only axons can permeate the outside of the pillars while the cells body is confined there. The rest of the circuit is designed in a way such that the axons will be guided forward along the circuit walls to the next structure, with the only a very minute probability of growing backwards. It was proposed and made by Forró *et al* [88] in 2018 and was never reproduced by other groups. The design used in this work is adopted from the original design with modifications to smooth out some edges and better lead the propagating axons. In Fig. 3.3, a visualization of the CAD design is shown. The Stomach mold fabrication depicted in Forró *et al* paper uses projection lithography trough photomasks to expose the desired design, which makes the alignment steps relatively easy compared to using a DWS machine and also knowing *a priori* which exposure intensity and dose to use, due to the the datasheet of the

photoresists providing such information.

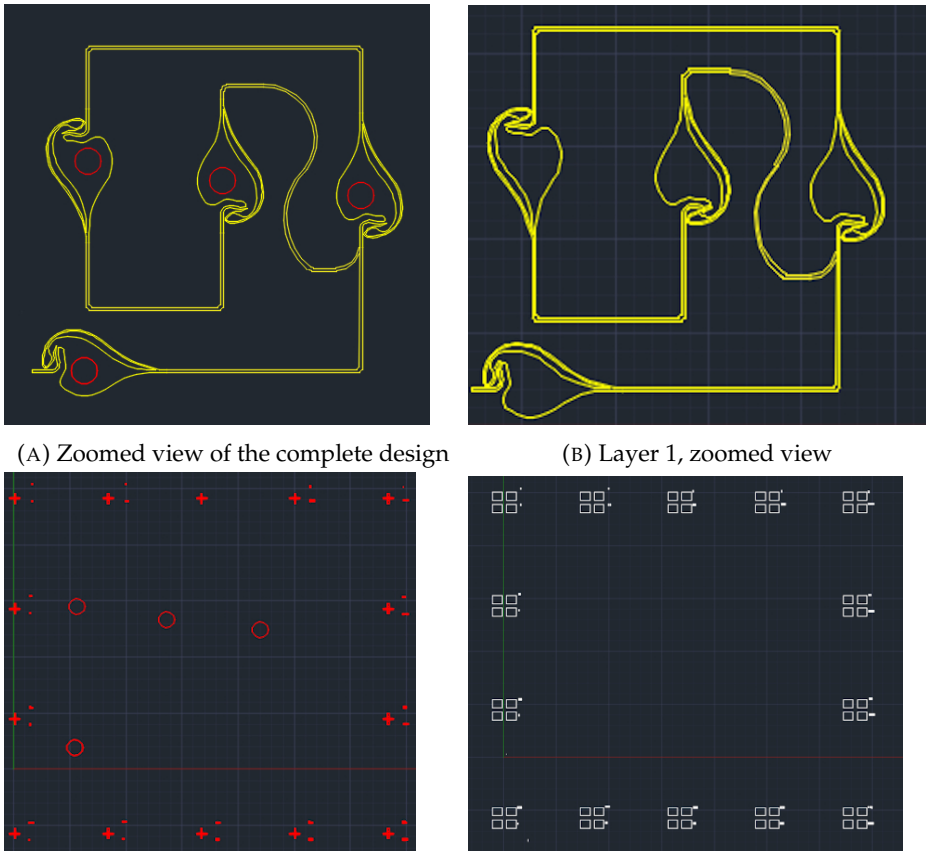

(A) Zoomed view of the complete design (B) Layer 1, zoomed view

(C) Zoomed view of layer 2 (D) Alignment marks

FIGURE 3.3: **Stomach CAD design.** The complete design (a), and it's two layers (b) zoomed image of the CAD design of layer 1 (without the alignment marks due to image size constrains), (c) layer 2 (with its alignment marks) and the alignment marks (d). The alignment marks are not shown due to image size constrains

For versatility reasons, the method opted for exposing our design was with the μmPG 101 tool from Heidelberg Instruments, which was the first time the Stomach design was reproduced with a Direct Write System giving us the advantage to modify the design at will but bringing the drawbacks just mentioned when compared to the projection lithography.

3.2 Lithography problems and solutions

As previous mentioned, both designs have two different heights, more specifically 10 μm and 100 μm. To obtain these features, SU-8 3005, which is capable of producing thicknesses between 5-10 μm, was chosen for the first layer and SU-8 2100, which produces layers with thicknesses ranging from 100 to 250 μm, was choose for the second layer.

Due to the microfluidic device features, alignment marks were written in the substrate to enable the alignment processes of the two layers. These marks were created by coating the substrates with positive S1818 photoresist, exposing with the desired mark design and subsequent development. After these steps, the substrates were then placed into an IBD machine (Commonwealth Scientific IBD System) where a thin film (100 nm) of Al was deposited. After placing this substrate in an acetone bath to remove the developed photoresist, it was left with the alignment marks. The fact that both SU-8 photoresists are very transparent to visible light and the Al thin film is very reflective, enables a good view of the alignment marks in the alignment processes throughout, as seen in Fig. 3.4.

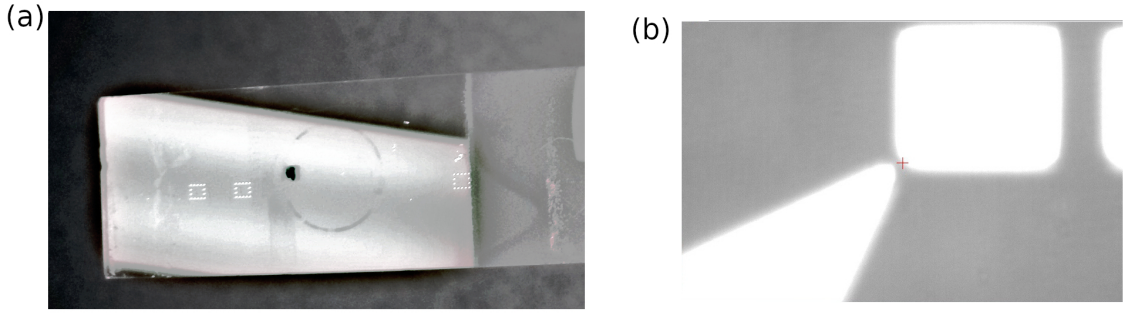

FIGURE 3.4: **Alignment Marks**. Photo of the alignment marks on the substrate (the image treatment was done to provide a better visualization of the marks) **(a)**; Starting writing point viewed trough the DWS machine camera with layer one deposited **(b)**.

The next problem faced was how to properly align both exposed designs with the alignment marks. The main problem was that the moving stage of the DWS machine is built to accommodate circular substrates, while the ones used in this work are rectangular. As such, between exposures it was impossible to ensure that the substrate was placed at the exact same site and without any variation in its angle position. The first approach tried to overcome this problem was by using the machine's in-built alignment tools, which would give the X, Y and theta offsets. However, this proved insufficient as well as very time consuming. The desired solution would have to ensure that the writing position of substrate on the DWS's stage for all layers (the alignment marks, the first and second layer) was the same. To do this, we used the setup seen in Fig. 3.5 where through, the use of the alignment pin's and two other glass substrates, we were able to maintain the middle substrate in roughly the same position for every exposure session.

Using this setup, it was now possible to use the DWS machine in-built camera to manually search for the point of origin of the offset coordinates, Fig. 3.4 (b), to successfully expose each layer.

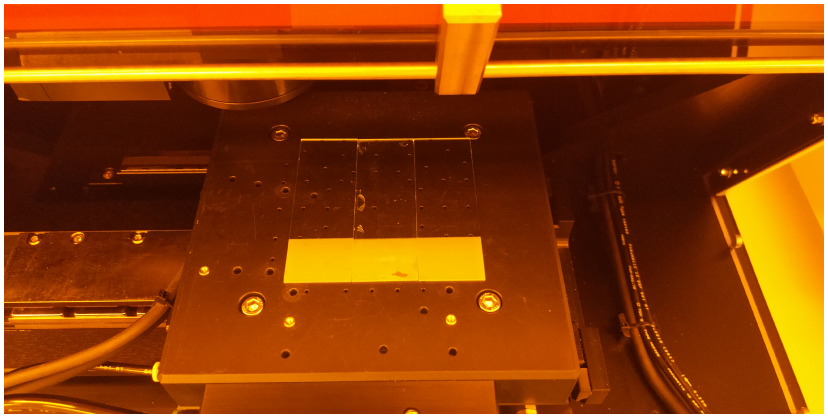

FIGURE 3.5: **Alignment solution.** With this setup it was possible to maintain an almost identical position for the substrate to be written.

Another problem encountered during this work, which was not possible to overcome, was the impossibility of using the optical microscope or the profilometer machine at the clean-rom, between lithography steps. This was due to both machine's using visible light with no UV filter. Because of this, it was not possible to use the microscope to confirm if each layer was properly aligned with the alignment marks. Another important drawback was associated with the development step, without the possibility of using the profilometer to know if the development time was enough to achieve the desired thickness or to use the microscope to confirm if the sample was properly developed. Thus, because of this drawback, the optimizing process was much more laborious and time-consuming than desired. With UV-filters in both machines, it would have been possible to detect, between steps, a bad alignment, the thickness of the deposited layers and also the correct development time by observing our sample after removing it from the develop bath at different time intervals. Instead, all this must be observed at the end of the entire fabrication process, which lasts about 5 hours, slowing gravely the optimization process.

3.3 Lithography Optimization

Choosing to use a DWS machine for the exposure process brings advantages and disadvantages. The possibility to change any time our design to test different features and/or correct details and also the costs reduction over projection lithography, which is always present in any research field, are the key advantage factors. In the opposite spectrum, the majority of paper/books about microfluidic techniques and also the photoresist's

datasheets are optimized and tested only on projection lithography systems. This, coupled with the ease that this technique has in the alignment procedure (in comparison to the available DWS machine, specially when using rectangular substrates) form the disadvantages of using the exposure option we choose.

3.3.1 Exposure energy dosage

As such, one of the difficulties found was what power intensity to chose in the DWS machine for the different thicknesses. The optimization was done by performing test exposures for the two different thickenesses ($10\mu m$ and $100\mu m$). For that, we optimized the exposure energy dosage by performing an energy series in the μPG 101 tool from Heidelberg Instruments. In the Direct Write System (DWS), the user can choose the laser power, in mW (from 1 to 70 mW), and the pixel pulse duration (PPD), in percentage (from 1 to 100 %).

SU-8 3005 photoresist

For this photoresist, the thickness obtained after spin coating it with the parameters of Table 3.2 was of $10\mu m$. From the previous work done on this same machine by M. Cerquido [112] and also confirmed by us, we knew that for very thin S1818 photoresist layers of around $2\mu m$, the optimal exposure power was of 10mW and a PPD of 18%. With this prior information, we knew that the values for our layers must be much higher, just by comparing the exposure energy values from the datasheets between the S1818 and the SU-8 3005 and 2100. As such, we did exposure energy series from 20mW with 100% of pixel

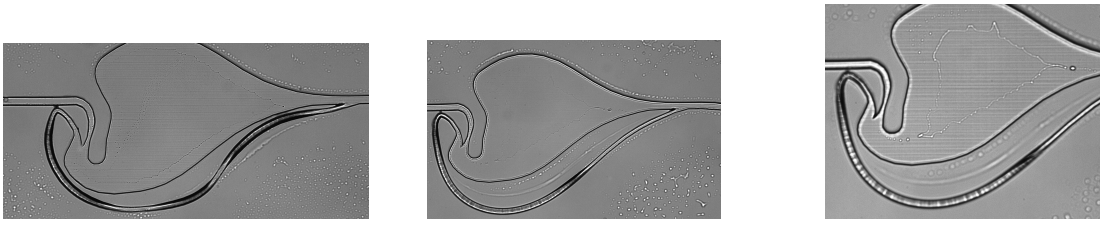

(A) 20 mW at 100% (B) 30 mW at 100% (C) 35 mW at 100%

FIGURE 3.6: **Microscope view of the pattern of layer 1 of the stomach design exposed in the SU-8 3005 photoresist.** The main influence of insufficient laser power is in the definition of the more thinner structures, as seen in these images.

pulse duration to 70 mW with 100% and found that a power of 40mW was sufficient to successfully imprint our desired pattern. In Fig. 3.6, the results of insufficient laser power are presented. The next step was to optimize the PPD percentage by doing a test exposure

at 40mW from 10% to 50%, concluding that a 40% was the ideal one. From this tests, we also found that a 30mW at 40% was the minimum exposure parameters to successfully expose the total thickness of the photoresist, however we opted for a security margin and choose the previous mentioned parameters. Fig. 3.7 shows the pattern transferred to the sample using the optimized parameters.

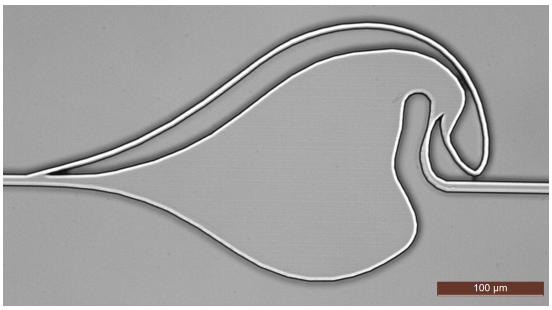

FIGURE 3.7: Optical microscope image of the exposed patterns produced in SU-8 3005

SU-8 2100 photoresist

This photoresist was choose to produce the second layer of both the stomach and chamber designs to enable a thickness of around $100\mu m$. Combining the previous information on the exposure parameters of SU-8 3005 layer, with the fact that this layer is 10 times thicker, we knew that it would need a larger power and PPD. As such, we did an exposure energy series from 40 mW with 100% of pixel pulse duration to 70 mW with 100% and found that a power of 50mW was ideal to successfully imprint our desired pattern. Next, a PPD study was done at 50 mW from 40% to 60%. We then concluded that the optimal exposure parameters were a 50 mW power and a PPD of 60%. The use of this parameters enabled the successful pattern imprint of the second layer seen in Fig. 3.8.

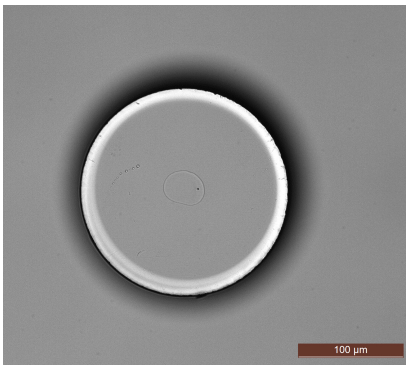

FIGURE 3.8: Optical microscope images of the exposed patterns produced in SU-8 2100

3.3.2 Spinner and hot-plate parameters optimization

The parameters we were using for the bake times and the spin coating were extracted directly from the manufacturer datasheets [113, 114]. However, as previous mentioned in the exposure section, the information there did not apply correctly to our fabrication methods.

3.3.2.1 Spinner parameters

The initial parameters used were the ones from the recommend program of the datasheet, which were producing adhesion and thickness variation problems as well as not resulting in the desired thicknesses. In order to correct this, we followed the reports of Mata *el al* [109] in which the study and fabrication of multi-level SU-8 (2010 and 2100) microsctructures using multiple coating was performed. From this study, the photoresist thickness versus the spin velocity were extracted and we then updated the spin cycle value to that of the paper to obtain a 100μm layer with the SU-8 2100 photoresist, and also updated the spread cycle parameters for both layers to the ones refereed in the paper. The only information left was, what correct velocity of the spin cycle to use for the SU-8 3005 photoresist.

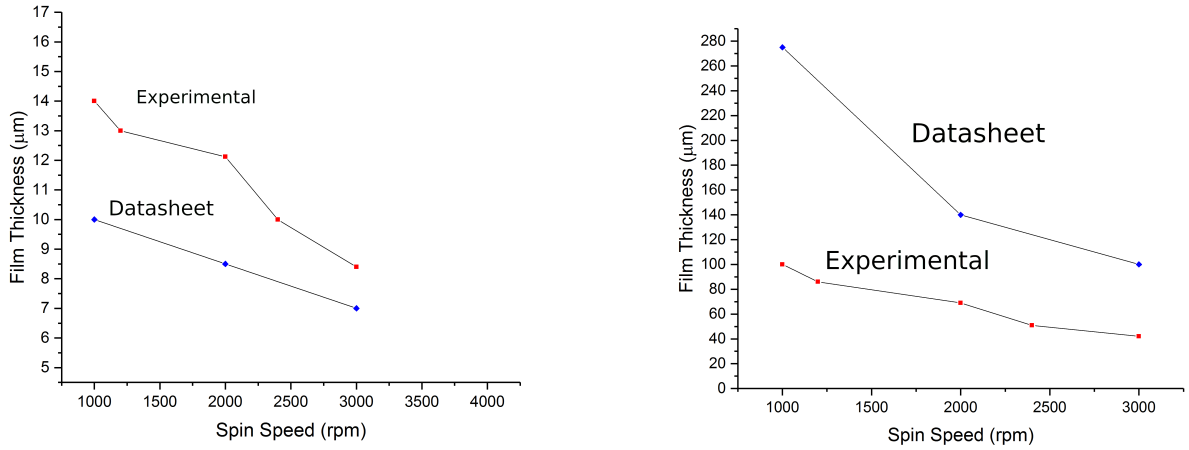

(A) SU-8 3005

(B) SU-8 2100

FIGURE 3.9: **Photoresist thickness versus spinner velocity.** Comparison between the photoresist thickness obtained in the clean-room and the reported thickness of the datasheet, for (a) SU-8 3005 and (b) SU-8 2100.

The needed information was found in a paper by Bohl *et al* [110], where the authors stated that spinning SU-8 on top of SU-8 requires a larger speed, approximately 1.2 times

higher, than spinning on silicon. With this new information we updated the spinner parameters to the ones in Tables 3.2 and 3.3. By examining the layer thicknesses with the profilometer for various spin cycle velocities, seen in Fig. 3.9, we concluded that the optimal velocity should be of 1000 rpm to obtain a thickness of $100\mu m$ with the SU-8 2100 photoresist and a velocity of 2400 rpm for a thickness of $10\mu m$ with the SU-8 3005 photoresist, which confirms that many different parameters influence the lithography processes.

3.3.2.2 Hot-plate parameters

Once again, we started by using the parameters obtained from the datasheet which were optimized for single layer on a silicon substrate. By using these parameters, various problems occured like the ones reported in section 3.3.2.1 and also poor pattern resolution, specially of the first layer, as seen in Fig. 3.10. To overcome this, we used the hot-plate parameters for the pre- and post-exposure bakes from Mata *el al* [109]. The bake temperatures were the same, however their times were much longer. Specially the longer pre-bake time for the SU-8 2100, helped to ensure a greater mobility of polymer molecules letting gravity lead to the annihilation of the edge bead and other possible variations of the layer thickness. However, this proved not enough and the solution came by combining the bake temperature and times from the just mentioned paper with the information from Bohl *et al* [110], which led us to introduce ramping steps. This is not necessary for single SU-layers were the glass transition temperature avoids stress from being induced in the layer. However, this is not true for multilayer processes, were the mismatch between the thermal expansion coefficients of the cross linked SU-8 (52 $ppmK^{-1}$) and the glass substrate (8.5 $ppmK^{-1}$) can cause adhesion problems. As such, temperatures ramps of $10^oC/min$ were introduced in the pre- and post-exposure bakes to mitigate these effects. Another important parameter which was changed, was the PEB (Post-exposure bake) of the first layer, from 65^oC for 1 minute and then at 95^oC for 5 minutes to just a short bake at 65^oC for 1 minute. The justification is that the long pre-bake of the next layer induces further polymerization of the exposed photoresist areas below and the short PEB prevents diffusion of the solvent from the subsequently spin-coated layer to the previously deposited one.

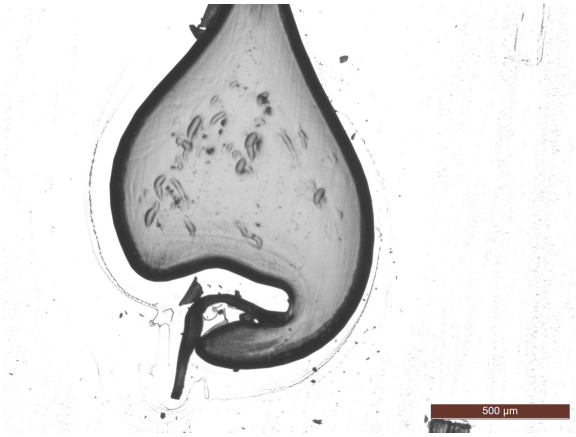

FIGURE 3.10: **Microscope view of the layer 1 of the stomach design transferred to the SU-8 3005 photoresist.** Here we can see how the effects of insufficient baking (15 minutes of post-baking) affect the resolution of the transferred pattern.

3.4 Stomach design fabrication

Being the first time this microfluidic design was manufactured using a direct-write machine it was considered of importance to write here the whole procedure in the eventuality that other people may want to use this technique to replicate this or similar designs. However, before describing the fabrication steps, some problems intrinsic to this design and the proposed solutions are presented.

3.4.1 Stomach design: Problems and Solutions

The alignment between the first and second layer must be very precise, the reason being that the second layer is comprised of pillars of $100\mu m$ in diameter, which must be exposed in the center of the stomach structures (which have a diameter of around $200\mu m$). As such, entering the correct values of the X and Y offsets in the machine is imperative. With the first layer, the WSP is easy to see and find as can be seen in Fig. 3.4 (b). However, when using the DWS's camera to search for the alignment marks on a thick layer of photoresist, such as layer 2, diffraction of the light going trough the layer causes the image of the marks to be heavily distorted. This effect can be seen in Fig. 3.11 (a), which leads to a major uncertainty of choosing the right WSP coordinates and results in a bad alignment of the two layers, as reported in Fig. 3.12. To mitigate this effect, a new alignment mark (Fig. 3.4) was made. The design of the new mark was composed of three whole marks where the designs of layer 1 and 2 were to be confined inside. The particularity of this

new design was that the first mark had its origin at the (0,0) coordinates, whilst the other two marks were displaced horizontally from the origin by 3.2 and 3.9 centimetres.

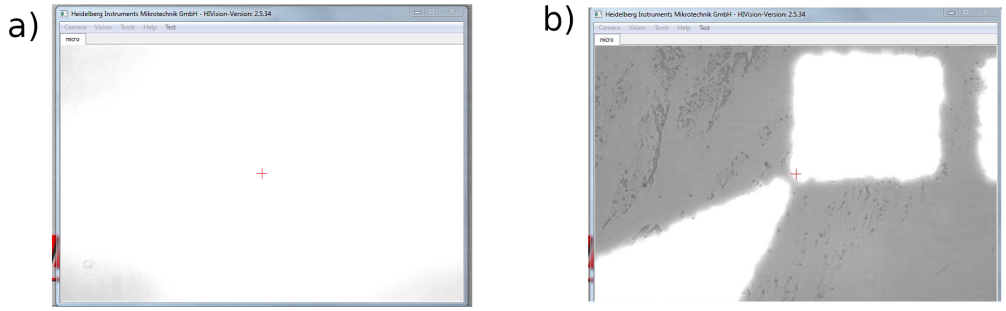

FIGURE 3.11: (a) Comparisons of the DWS's camera view Sample with thick SU-8 layer; (b) Sample with the photoresist removed from the area of the WSP (b)

This enabled a safe distance between the first and the other two marks, to be able to remove the photoresist around the first mark with acetone. With the removal of the photoresist in that area, it was now possible to see in the DWS's camera the WSP.

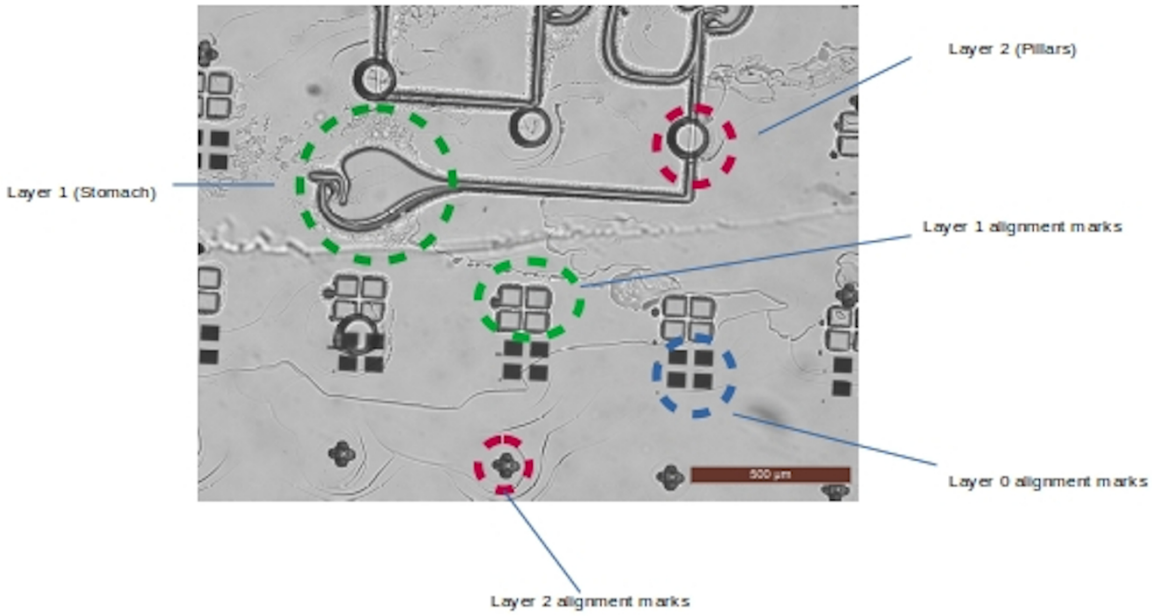

FIGURE 3.12: **Microscope view of the stomach design.** Result of bad alignment, due to choosing the wrong WSP coordinates for the second layer

However, after removing the photoresist in the desired area we are left with a substrate with two very distinct profile areas, as seen in Fig. 3.16, which may damage the laser's

writing head while moving through the sample. To prevent this, the following steps must be taken :

1. Center the stage
2. Move the laser head to the area where the photoresist was removed
3. Automatic Focus
4. Search and enter the WSP coordinates
5. De-Focus
6. Move the laser head to the area where there is photoresist in the substrate
7. Automatic Focus
8. Write

It is important to note that, in order to save time, the CAD files of layer one and two do not have any design to expose in the first mark. This was done to shorten the DWS's machine writing time, as anything written in the area of the first mark was removed and also because, if the design of the second layer had any feature in that area, it could damage the laser's head by making it expose with such high power the area without photoresist.

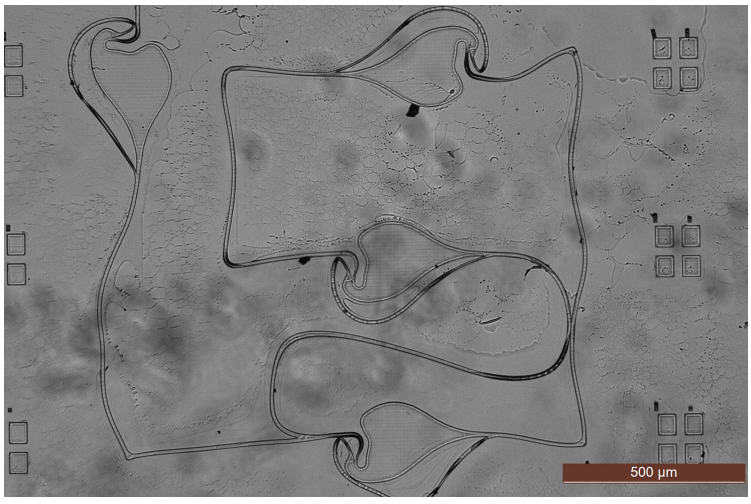

FIGURE 3.13: Microscope view of the effect of bad adhesion on the first layers structures

Another problem encountered during the lithography process was the bad adhesion between the first layer and the substrate's glass surface. A first approach to solve this was to do a dehydration bake at 200^{o}C for 15 minutes. However, this was not sufficient

to prevent the smallest features of the first layer (about $10\mu m$) to drift, as observed in Fig. 3.13. Without the possibility to use standard substrate adhesion promoters (piranha etch, oxygen plasma treatment, etc.) we opted to deposit a very thin layer of SU-8 of ($\sim 5\mu m$), fully exposing it, which ultimately improved greatly the adhesion of the subsequent deposited layers.

3.4.2 Mold Fabrication

This process will be divided into various parts for easier reading and a general view of the process is presented in Fig. 3.14. The runsheet of the whole process can be found in the Appendix section B.

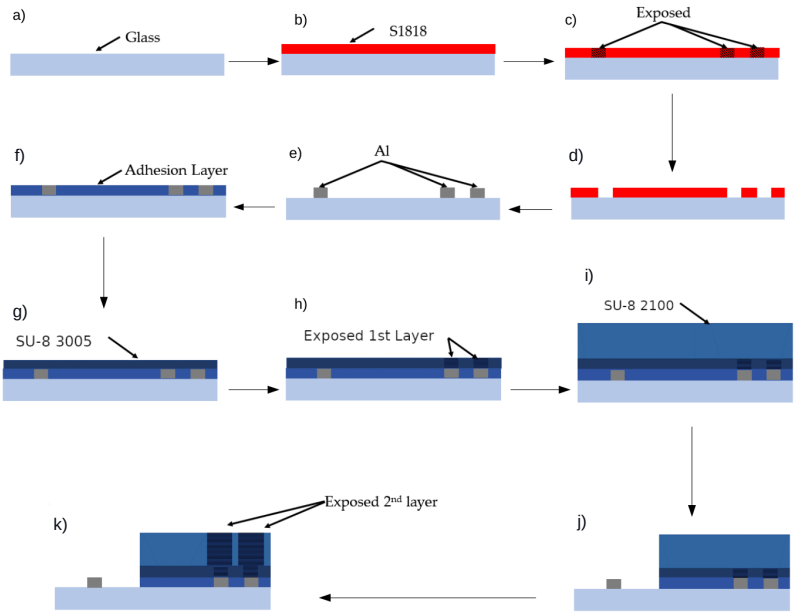

FIGURE 3.14: Schematic representation of the stomach design microfabrication process until the developing step. (a,b,c) alignment marks exposure and devolping; (e) Al thin film deposition defining the alignment marks onto the substrate; (f) Adhesion layer deposition; (g,h) first layer deposition and pattern exposure; (i,j,k) second layer deposition, removal of the photoresist around the sacrifice mark and pattern exposure.

3.4.2.1 Substrate preparation

The substrate chosen was standard glass. To start the process, the substrates were first cleaned by placing them in acetone in an ultra-sonic bath for five minutes. After that, the sample was placed for five more minutes in an ultra-sonic bath with isopropanol. Finally, the substrate was washed with deionized water and was dried with N_2. Then, the substrates were placed in a hot-plate (Electronic Micro Systems Model 1000-1 Precision Hot

Plate) with the cover on at 200°C for 15 minutes to prevent any leftover water molecules at the surface, thus improving adhesion of the photoresist to be spun.

3.4.2.2 Alignment marks

After the preparation step, the substrate was placed in a spinner machine (Fig. 3.15, (PWM50 Headway Research) fixed by vacuum, where an S1818 positive photoresist was deposited on top of it, after which it was spun at a velocity of 3000 rpm for 30 seconds with an acceleration of 1000 rpm/s. This is followed by a pre-bake at 115°C for 60 s, and then left to cool down at ambient temperature for 5 minutes.

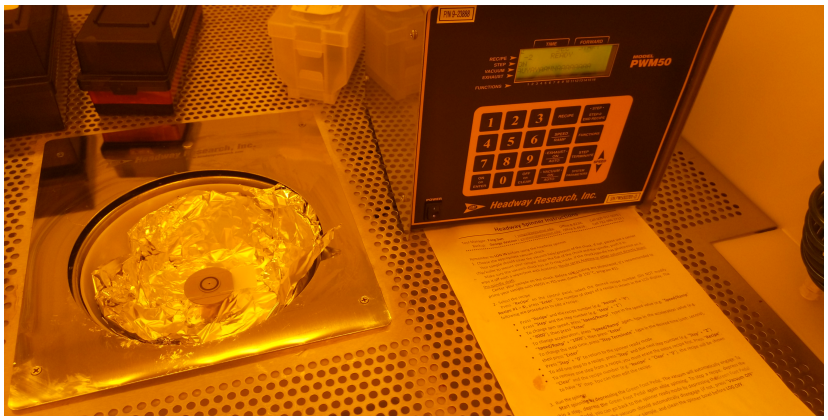

FIGURE 3.15: **Spinner Machine** Setup of the spinner machine used to coat the substrates with the photoresist

Next, the exposure of the alignment marks, Fig. 3.3 (d) onto the photoresist was done in the DWS machine with the setup shown previously in Fig. 3.5 and choosing the X and Y offsets in the machine's program to be inside the circle depicted in the runsheet of the process, choosing a power of 20 mW and a pixel pulse duration (PPD) of 22%. After exposure the photoresist was developed with 3 parts deionized water and one part developer (Microposit 351), and then placed in the IBD vacuum chamber where a thin layer of 100 nm of Aluminium was deposited.

3.4.2.3 Adhesion layer

After removing the sample from the IBD machine, the steps from section 3.4.2.1 were repeated to remove the photoresist layer left, followed by an identical dehydration bake. The substrate was then placed in the spinner machine and the SU-8 3005 photoresist was dispensed onto the sample and spun according to the parameters of Table. 3.1, producing a very thin layer of around 5 μm.

Spinner Parameters	v(rpm)	a(rpm/s)	t(s)
Step 1	200	500	20
Step 2	3000	500	45

TABLE 3.1: Adhesion layer spinner parameters

Subsequently, the sample was placed in a hot-plate to pre-bake at 65^{o}C for 1 minute followed by another bake at 95^{o}C for 5 minutes. Then, to fully expose the thin photoresist layer, a flood exposure is performed with a mask aligner tool for 30 s at an intensity $300mJ/cm^2$, followed by a post-exposure bake at 95^{o}C for 5 minutes, letting the sample rest at ambient temperature for 10 minutes.

3.4.2.4 First Layer

With the adhesion layer defined, we can now do the first layer of our design. Using again the SU-8 3005, the sample was placed in the spinner and spun with the parameters of Table. 3.2 to produce a 10μm thickness layer. Next, a pre-bake identical to the Adhesion

Spinner Parameters	v(rpm)	a(rpm/s)	t(s)
Step 1	200	500	20
Step 2	2400	500	45

TABLE 3.2: First layer spinner parameters

layer was done. The substrate was then left to cool down at ambient temperature for 10 minutes, before being placed in the DWS machine to expose the design of the first layer, Fig. 3.3 b), using the setup of Fig. 3.5 and searching, with the machine's camera, the starting point of the writing process, as seen in Fig. 3.4 b), setting the laser power to 40mW and the PPD to 40%. After finish exposing, the substrate was subjected to a very short PEB for 1 minute at 65^{o}C.

3.4.2.5 Second Layer

The final layer, which is around 10 times thicker than the first layer, was obtained using the SU-8 2100 photoresist with the spin parameters of Table. 3.3. After the photoresist was spun on top of the substrate, it was placed in the hotplate at the starting temperature of 65^{o}C with the lid on, programmed to the steps of Table. 3.4. After the pre-baking, which totalled around 1h40, and before exposure, the photoresist of the area around the origin mark had to be removed. This was done very carefully using cotton tips and the

Spinner Parameters	v(rpm)	a(rpm/s)	t(s)
Step 1	200	500	20
Step 2	1000	500	45

TABLE 3.3: Second layer spinner parameters

Hot-Plate Parameters	T(^{o}C)	Ramp(^{o}/min)	t(min)
Step 1	65	-	5
Step 2	95	10	45
Step 2	20	2	10

TABLE 3.4: Second layer pre-bake steps

cleanroom paper soaked in acetone to remove the photoresist, while holding the sample vertically to ensure that the acetone wouldn't reach the photoresist area to be exposed and also using very little acetone each time so as to not let a significant quantity of it evaporate and corrode the rest of the photoresist. The removed area was then washed with isopropanol first and then deionized water. Fig. 3.16 shows the final result.

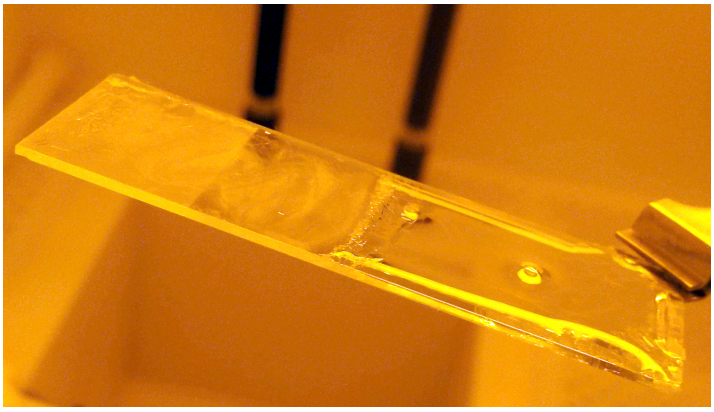

FIGURE 3.16: Substrate with the area around the WSP removed

After this the sample was placed again in the DWS machine, using the same setup discussed for the other layer. However, this time the steps described in section 3.4.1 must be followed to prevent any damage to the laser head before exposing the design of Fig. 3.3 c). With the exposure complete, the sample was placed again in a hot-plate with the lid on to perform the PEB. Its parameters were the same as in Table. 3.3, with the exception of the time of step 2 which was changed to 35 minutes. Finally, the sample was developed by placing it in a glass recipient with a SU-8 developer in the ultrasonic cleaner machine, for 13 minutes. The final result of the lithography process is shown in Fig. 3.17.

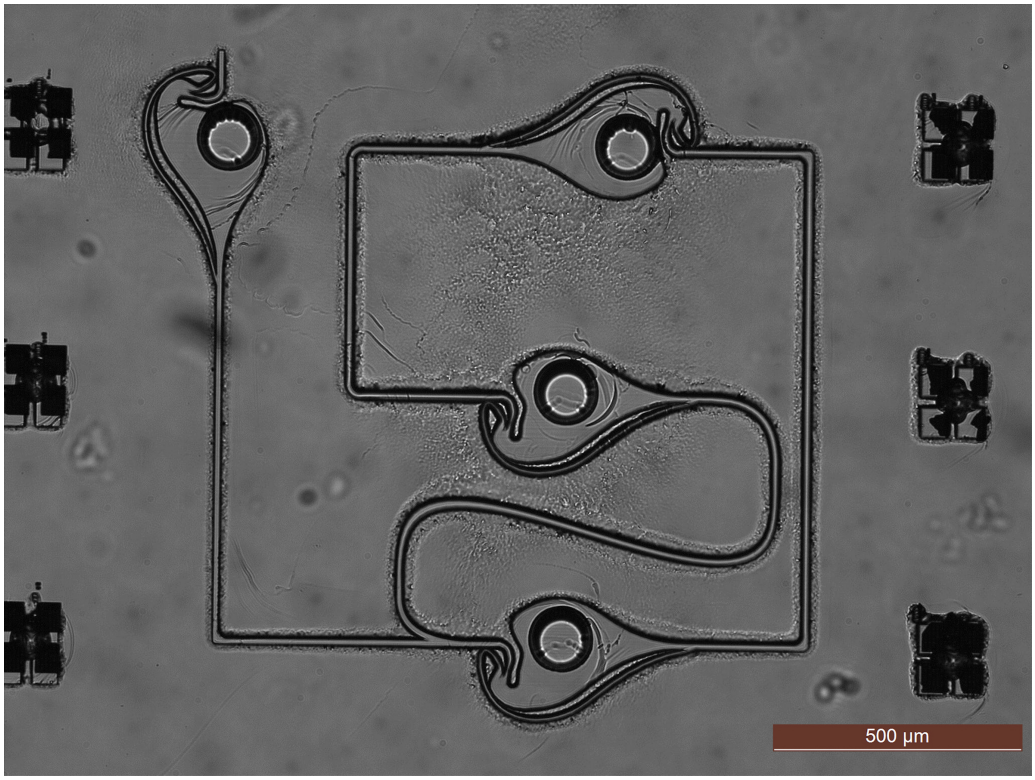

FIGURE 3.17: Microscope view of the result of the complete lithography process for the stomach design

To note that the dark circles surrounding the pillar structures of layer two are originated from the microscope's light shining into this structures, thus casting a shadow over the substrate.

3.4.3 PDMS Casting

The sample seen in Fig. 3.17 has the purpose to serve as a mold to produce various replicas by casting PDMS on it. In this work we used a SYLGARD 182 Silicone Elastomer kit, supplied in two parts consisting of the PDMS base and the curing agent components (Dimethyl, Methylhydrogen Siloxane). To obtain our PDMS we mixed these two compounds in a ratio of 10:1, respectively, with the aid of a spatula. Next, to remove air bubbles, we placed the mixture in a vacuum chamber for three hours. Having our PDMS bubble-free, we are ready to spin-coat it in top of our sample. To achieve this we used a home-made spinner at a spinning speed of 750 rpm for the stomach design and 1000 rpm for the chamber design, for 30 seconds. These parameters enabled us to achieve a PDMS thickness of roughly 77 μm, which is less than the thickness of the pillars from the second layer (100 μm). It is very important that the PDMS thickness to smaller than that of the

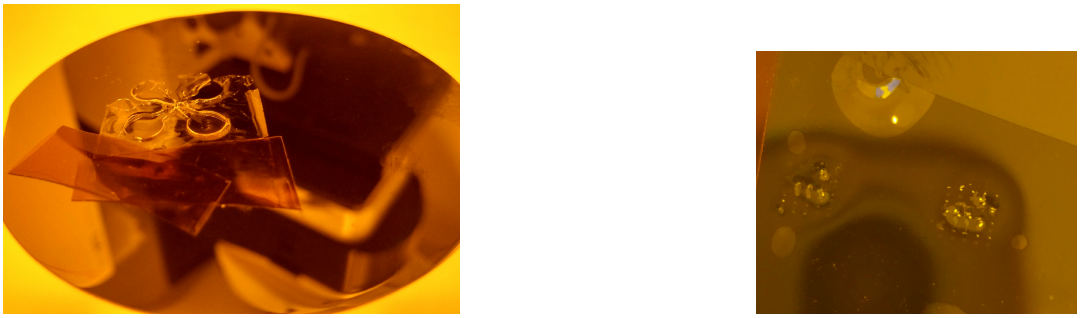

(A) μEF chamber (B) Stomach design

FIGURE 3.18: **Photographs of the PDMS casted structures.** μEF chamber is seen in (a), noting it's large proportions in comparison to the two structures of the stomach design in (b) (in the picture we can see the same design pattern side by side)

pillars, because these pillars will serve as the channels to deposit the cells to study. Their small diameter prevents the use of manual perforation without damaging the remaining structures. Thus, there is the need for them to be open at the end of the PDMS coatings.*

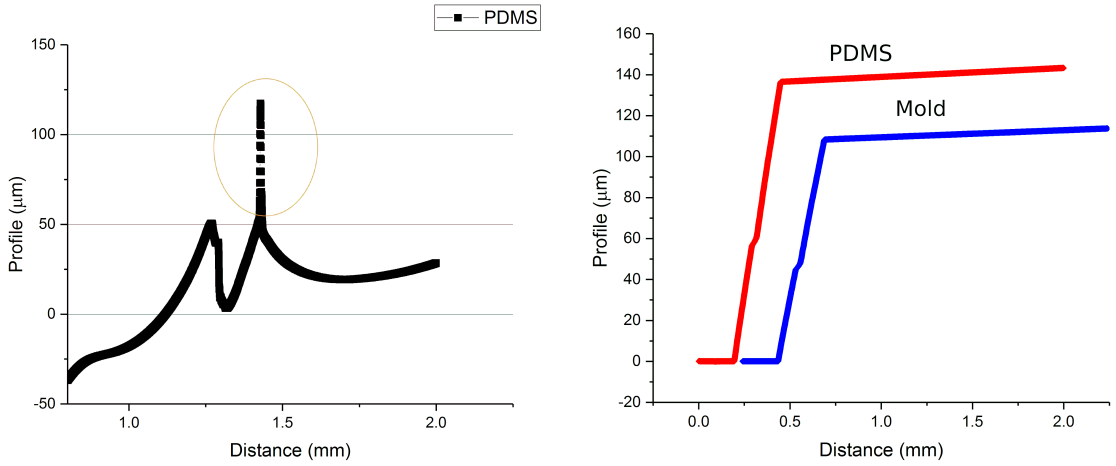

(A) The red circle represents the effect of the profilometer tip getting stuck at the pillars walls.

(B) Red curve represents the mold thickness and the blue one the PDMS thickness.

FIGURE 3.19: **Curves plotted from the data acquired with the profilometer** μEF chamber (a), stomach design in (b)

After the spin-coating process, we placed the substrate with the polymer in an oven for two hours at 80^o to cure it. Finally, we removed, carefully, the casted PDMS and placed it in a clean glass substrate. In Fig. 3.18, the casted structures for both designs are shown on top of a Silicium wafer (for better visibility). After casting, we analysed the PDMS and the mold structures in a profilometer to see if the desired thickness was obtained. For the

*In contrast to the pillars of the uEF Chamber which have a large enough diameter to be penetrated by the needles to inject the cells.

μEF chamber we were expecting a thickness of ($\sim 100\mu m$) which had to be larger than the thicknesses of the mold.

Thus, by comparing the thickness of the PDMS and the mold in the profilometer, seen in Fig. 3.19 (a), we confirmed that a sufficient PDMS coating was achieved. For the stomach design the analysis of the PDMS structure was more difficult.
The reason, is that, if successfully done, the pillars of layer 2 have to be open. This is problematic for the profilometer tip because it gets stuck on the thin walls of the pillars and also because of its size, it cannot descend completely to the pillars bottom. Thus, to confirm if the PDMS coating for this structures was correct, we diminished the tip's force. This allowed us to obtain the graph shown in Fig. 3.19, where the height of the pillars is read but its center is presented as a depression (resulting from lowering the tip force). As such, we confirmed, for both structures, that the PDMS parameters were sufficient to apply the proper coating for each design.

Chapter 4

PEDOT:PSS-mushroom microelectrodes

4.1 Fabrication of PEDOT:PSS microelectrode mushrooms

As previously discussed in section 2.5, Poly(3,4-ethylenedioxythiophene) doped with polystyrene sulfonate (PEDOT:PSS) is widely used as a coating on microelectrode arrays in order to reduce their impedance for both in vitro and in vivo electrophysiology. However, there hasn't been any publication on combining the advantageous morphology of the mushroom-shaped microelectrodes with the conductive polymer, PEDOT:PSS. Therefore, in this work we decided not to coat, but to see if it was possible to grow mushroom-shaped microelectrodes, made entirely of PEDOT:PSS in gold substrates.

4.1.1 Lithography optimization

To study the growth of PEDOT:PSS mushrooms, an array of homogeneous holes with 2 μm in diameter and a 20 μm inter-spacing was imprinted on gold coated substrates. The size of the array was 2x2 mm and the desired thickness of the photoresist used (S1818) was of 2 μm. In this section we will describe the optimization of the lithographic processes necessary to obtain the described arrays.

4.1.2 Spin Coating

Before coating the sample surface with photoresist, it is necessary to clean it. To clean the Cr/Au coated substrate, first the substrate was placed in acetone in an ultra-sonic

bath for five minutes. After that, the sample was placed for five more minutes in an ultra sonic bath with isopropanol. Finally, the substrate was washed with deionized water and was dried with N_2. Then it was placed in a hot-plate at 200^oC for 15 minutes to perform a dehydration bake to improve the adhesion of the photoresist to the substrate surface. Afterwards, the sample was placed in the spinner machine to coat the surface with the S1818 photoresist, after which it is then placed in a hot-plate to perform the soft bake at 115^oC for 1 minute. The spin-coating speed is proportional to the final thickness of the coated layer. As such, various speed-coatings were performed and then the thickness was examined with the profilometer. The optimal spin-coating values were then determined to be those of Table.4.1, by examining if the micro-pores were open in the microscope light.

Spinner Parameters	v(rpm)	a(rpm/s)	t(s)
Step 1	1000	500	30

TABLE 4.1: Adhesion layer spinner parameters

4.1.3 Exposure energy dosage

As stated in section 3.4.1, M. Cerquido [112] had already performed the optimization of the exposure energy dosage for arrays practically identical to ours (with the difference that in [112] the inter-spacing was of 10 μm). Therefore, the parameters to use in the Direct Write Sytem (DWS) machine were already know. Nevertheless, energy and PPD test series were performed to confirm if the previously used parameters were still valid. The parameters chosen were of 12 mW at 18% PPD. Using the aforementioned parameters and then developing for 1 minute, we obtained the desired arrays seen in Fig. 4.1

4.1.4 EDOT:PSS aqueous solution synthesis

EDOT:PSS aqueous solution was made by adding EDOT (97% 3,4-Ethylenedioxythiophene, Sigma-Aldrich) and PSS (Poly(styrenesulfonate), Sigma-Aldrich) to 100 ml of deionized water. Different EDOT:PSS ratios were used in order to find the one with best electrical conductivity. The ratios of EDOT:PSS used were the following: 1:1, 1:5, 1:11. The various solutions were prepared in a glass container and were agitated for 48 h with a magnetic agitator until homogeneous. Although at 16 h the 1:1 solution was already visibly homogeneous, the 1:5 solution took another 16 hours, whilst the 1:11 solution took the full

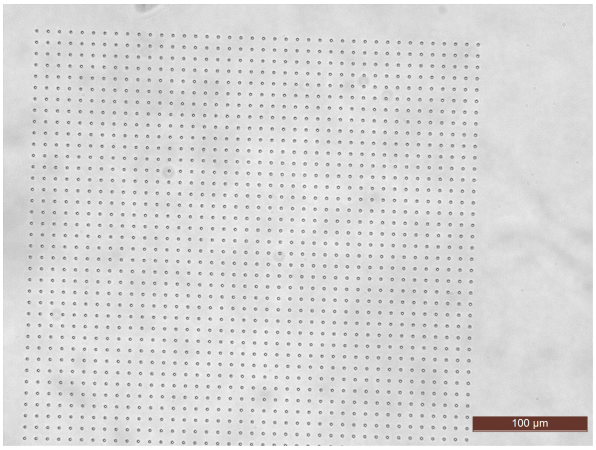

FIGURE 4.1: Optical microscope images of the transferred patterns produced in S1818

48 hours to reach a homogeneous state. The produced solution varied in colour from transparent to light-yellow, from the least to most concentrated.

4.2 EDOT:PSS polymerization and electrodeposition

As described in section 2.5.1, EDOT:PSS can be polymerized to form PEDOT:PSS through electrochemical polymerization which will, at the same time, deposit the conductive polymer onto the working electrode (in our case, the gold substrate). Electrochemical polymerization is the preferred technique for the synthesis of conducting polymers for coatings on biomedical devices, since it is reproducibly controlled, provides the highest conductivities, and deposits the polymer only on specified areas [100]. These specified areas, are the areas were the conductive substrate is exposed to the electrolyte solution, thus (in our case) the PEDOT:PSS particles will only grow on the micro-holes in the array. The polymerization and electrochemical deposition process were done in an electrochemical cell with a three-electrode configuration, as seen in Fig. 4.2. The counter electrode was a Platinum (Pt) mesh, the reference electrode was Ag/AgCl and the working electrode, where the PEDOT:PSS was deposited, was a gold substrate. The positioning of the three electrodes is very important and should be kept to the minimum possible distance. This ensures that the reference electrode obtains the exact measurement of the potential at the interface of the working electrode. The bigger the separation between the electrodes, the more resistance (uncompensated resistance) between them will be, thus inducing noise on the signal of the cyclic voltammetry (CV) [100]. Therefore, throughout all the polymerization experiments, the configuration seen in Fig. 4.2 was kept the same.

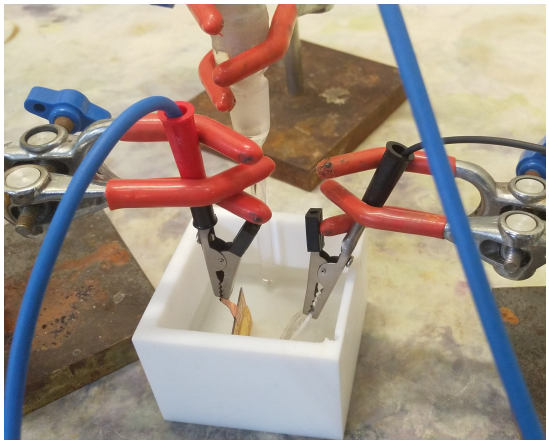

FIGURE 4.2: The electrodeposition set-up in a cell.

4.2.1 Voltammetry and deposition studies

In this work, the polymerization of EDOT:PSS was done through the potentiostatic mode (constant potential). As discussed in section 2.5.1, EDOT is polymerized through the application of an anodic (oxidative) potential, thus becoming conductive. However, this potential in relation to the Ag/AgCl reference electrode is very sparse in current literature. Coupling this with the fact that different EDOT:PSS ratios affect the conductivity of the polymer, a voltammetry study had to be done. The setup used was the one of Fig. 4.2, where we tested the three solutions made (section 4.1.4). The CV graphs obtained are displayed in Fig. 4.3. The most evident difference between the three graphs is their shape, particular the one from solution 1 (1:1) which differs the most from the other two. This difference is due to the different scan rate (the intention was to use a scan rate of 100 mV/s) used for the first solution, which is much lower than the one used for the other two, indicating a resistive behaviour due to the large polarization resistance at fast scan rates (originating the broad curves in the CVs of solutions 2 and 3).

Analysing the graphs from Fig. 4.3 we can observe two oxidation peaks (more clearly seen in the CVs of solution 2 and 3) at around 0.7 and 1.0 V. It is also possible to observe a crossover of the reverse cathodic scan over the anodic scan in the cycles of solution 1 and 2, giving rise to what has been called "nucleation loop" [115]. In particular, we observe a rise of the current of the reverse scan than that of the forward, in the region near the potential switching, until it drops again to the level of the CV curve of the forward scan. The possible explanation for this kind of CVs profiles as be interpreted as due to polymer nucleation effects [115], or to the homogeneous reactions between an oligomeric

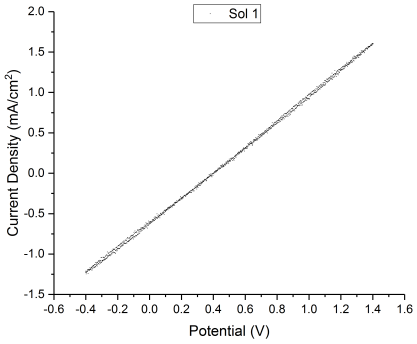

(A) Solution 1 (1:1) with a scan rate of 20mV/s

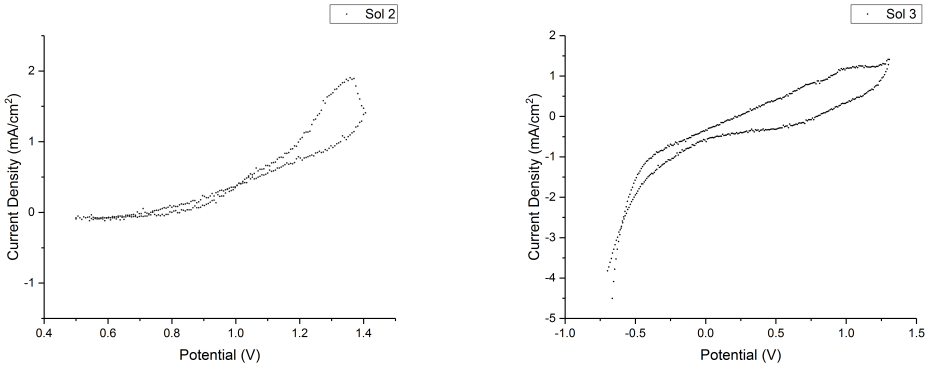

(B) Solution 2 (1:5) with a scan rate of 100mV/s (C) Solution 3 (1:11) with a scan rate of 100mV/s

FIGURE 4.3: Cyclic Voltammetry curves for the three solutions of PEDOT:PSS.

follow-up product (PEDOT) and the starting monomer (EDOT) [116]. However, more recently, it has been attributed to the low concentration of the EDOT monomer [117], which makes sense when comparing the graphs of Fig. 4.3, where the one of solution 3 is missing this feature and is also the one with the largest concentration of the EDOT monomer. To choose the most adequate potential for the polymerization of the EDOT monomers, we made another CV study focusing only on the forward curve. The reason is that, because of the nature of the electrochemical study, the polymerization of the EDOT and it is deposition occur at roughly the same time. As such, this will influence the profile of the CV curves. We can observe this effect in Fig. 4.4 where two consecutive scans were made to the same solution, increasing both anodic and cathodic current intensities. This effect can be explained by considering the growth at the electrode surface of an electroactive polymer film, whose thickness increases regularly with the number of cycles [118], and also to the water decomposition in the electrolyte during the electropolymerization process.

New voltammetry study (Fig. 4.5) was done with a scan rate of 30 mV/s and their current density adjusted to a logarithmic scale. This helped to smooth the curves and better

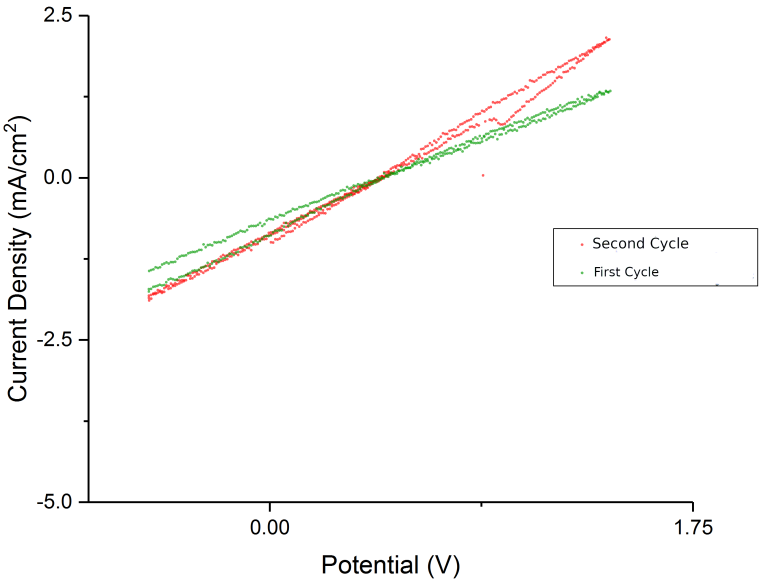

FIGURE 4.4: Influence of the number of scans in the profile of the CV curves for solution 1 (1:1)

observe the reaction rates through the inclination of these. By comparing with various CVs from the available literature, we decided to polymerize the EDOT:PSS at 0.7 V for the first solution and at 0.8 V the other two. Knowing the potentials at which the oxidation

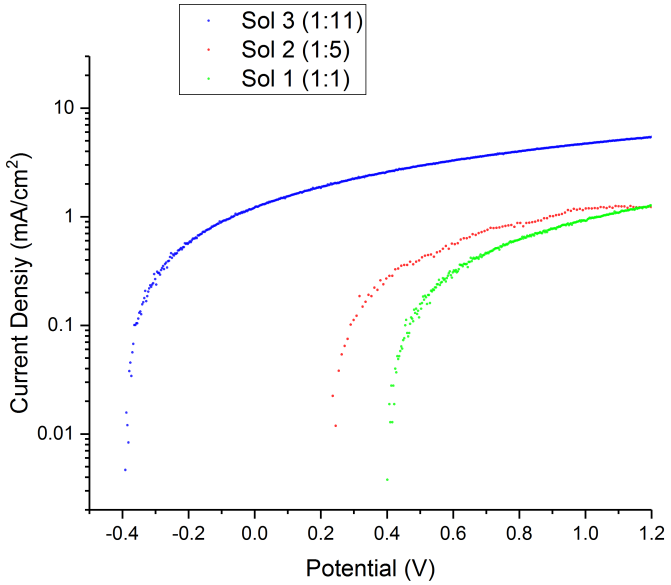

FIGURE 4.5: CV curves for the three different solutions at a scan rate of 30 mV/s

takes place, we then proceeded to test the deposition of PEDOT:PSS thin films on gold

substrates through the potentiostatic method with the configuration seen in Fig. 4.2. The three solutions were tested, performing an electrochemical deposition of 10 minutes each. This enabled us to observe the behaviour of the polymer deposited in the electrode for the different solutions. From these curves we concluded that the polymerization duration is roughly equal between the solutions. However, the quantity of deposited PEDOT varies greatly. The deposition curves* show a higher plateau current for the solution with the biggest concentration of EDOT, as in Fig. 4.7 a). This means that, for the same electrodeposition time, the solution with lowest concentration will produce a thinner film, as can be seen in Fig. 4.6.

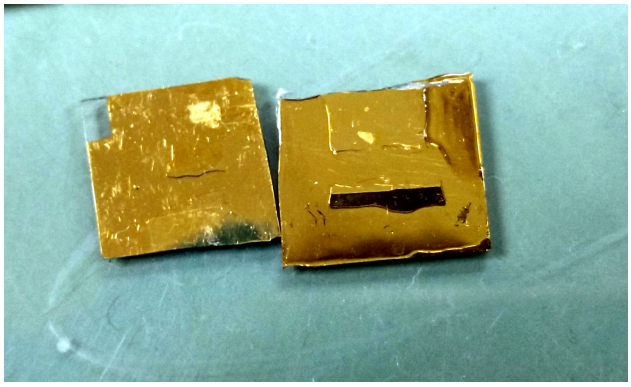

FIGURE 4.6: **Comparison of thin film growth of PEDOT:PSS films.** A 10 minute electrodeposition was done for solution 1 (left) and solution 3 (right).

We also tested various deposition potentials for solution 3 (1:11), from the potential of the first oxidation to the second oxidation peak. The obtained curves are presented in Fig. 4.7 b), showing an increase of the plateau currents with increasing polymerization potentials. This result has also been previously reported [118]. It is also possible to observe in these curves the three phases described in the literature [118]: nucleation, coupling, growth and doping.

Additionally, these curves show a significant amount of noise, probably due to oxygen oxidation. One way to reduce this would be to conduct all electrodepositions under N_2 atmosphere to de-aerate the solutions.

*The deposition curves for solution 2 (1:5) is practically indistinguishable from solution 3 (1:11), therefore it was omitted in the graphs to provide a better visualization

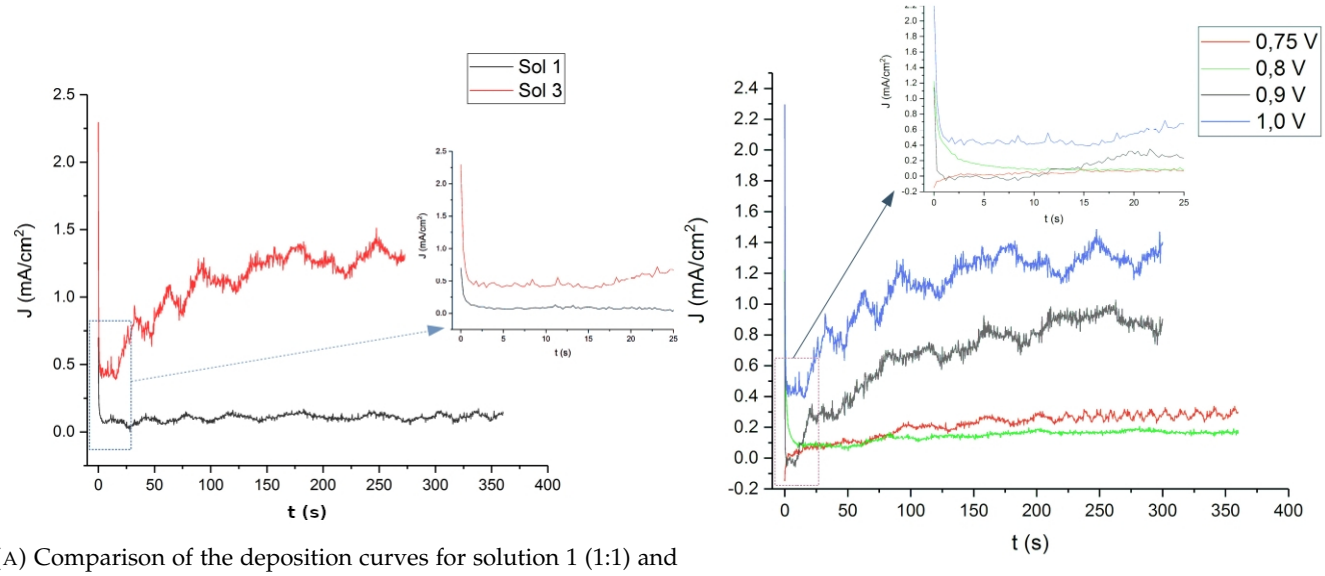

(A) Comparison of the deposition curves for solution 1 (1:1) and 3 (1:11)

(B) Deposition curves for solution 3 at different potentials

FIGURE 4.7: Deposition curves.

4.3 Electrodeposition in micro-pores

4.3.1 Produced samples

Electrodeposition in the micro-pores of the arrays lithographed in the gold substrates were carried on for the three solutions. The deposition process was done in the same cell configuration of Fig. 4.2. All deposition were made in potentiostatic mode at 0.8 V for 4 minutes. The produced samples were analysed by a SEM (scanning electron microscopy) equipment, enabling the visualization of the successfully created PEDOT:PSS-mushroom electrodes, as seen in Fig. 4.8.

Comparing the three samples, we see that, for the solution with the highest concentration of EDOT, [Fig. 4.8 c)], an overgrowth occurred where the larger structures seen are due to the fastened growth of the polymer once it leaves the micro-pore area. In contrary, for solution 1 an undergrowth is observed, producing mushroom-like structure with a depression in its center, indicating that polymer growth in micro-pores starts around the perimeter walls and the core of the structure follows afterwards (this phenomena will be discussed bellow). As such, the deposition time for solution 1 was insufficient while that for solution 3 was too large. However, for solution 2, the deposition time was perfect to create a homogeneous array of mushroom-electrodes. Fig. 4.8 also shows the variability in the produced cap diameters for each sample. Fig. 4.8 a) shows the produced micro-electrodes for solution 1, having a cap diameter between 3.3 and 4.1μm, with an average

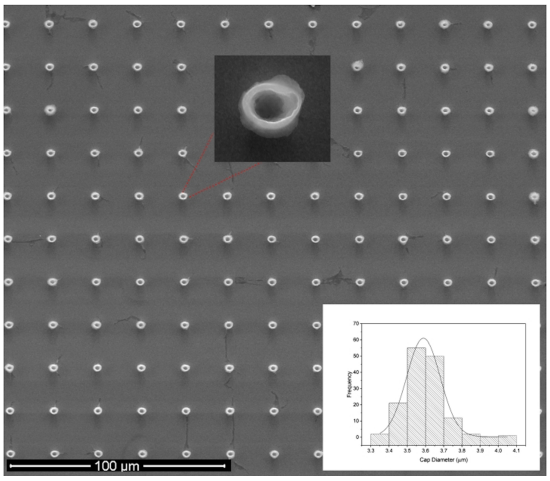

(A) Solution 1 (1:1)

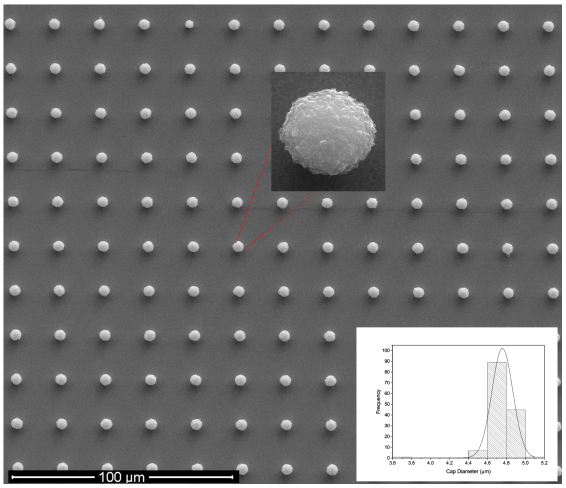

(B) Solution 2 (1:5)

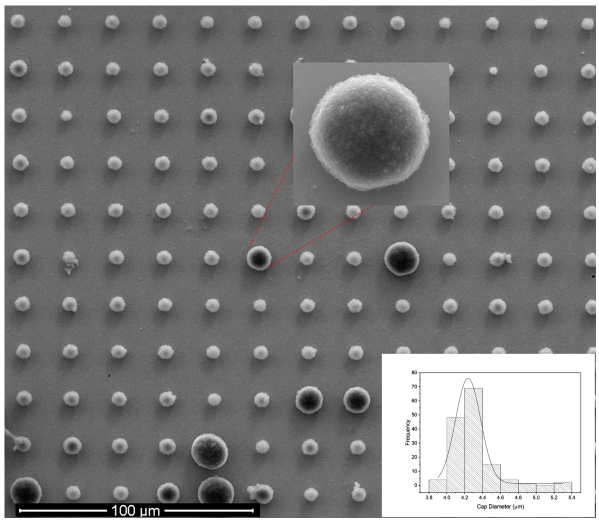

(C) Solution 3 (1:11)

FIGURE 4.8: **SEM planar view of the grown PEDOT-PSS-mushrooms in the gold substrates for the three different solutions.** The inserts show the size distribution of the cap diameter. Scale bar of 100μm

value of $4.758 \pm 0.001 \mu m$. Fig. 4.8 b) shows the results for solution 2. For this sample, the microelectrodes have caps diameters between 3.6 and 5.2μm, with an average value of $3.588 \pm 0.002 \mu m$. Finally, in Fig. 4.8 c), we have the results for the the structures grown with solution 3 which vary in cap diameter between 3.8 and 5.4μm with an average size of $4.238 \pm 0.003 \mu m$. In the figures insets it is also possible to observe a zoomed view of the electrodes, which have a characteristic flower-like appearance attributed to the many fine polymer sheets that constitute this structures. To further characterize the features of the produced samples, a 90^o view was acquired through SEM. The comparison of the grown structures is seen in Fig. 4.9.

This view permits us to analyse the dimensions of the mushroom stalk and cap which

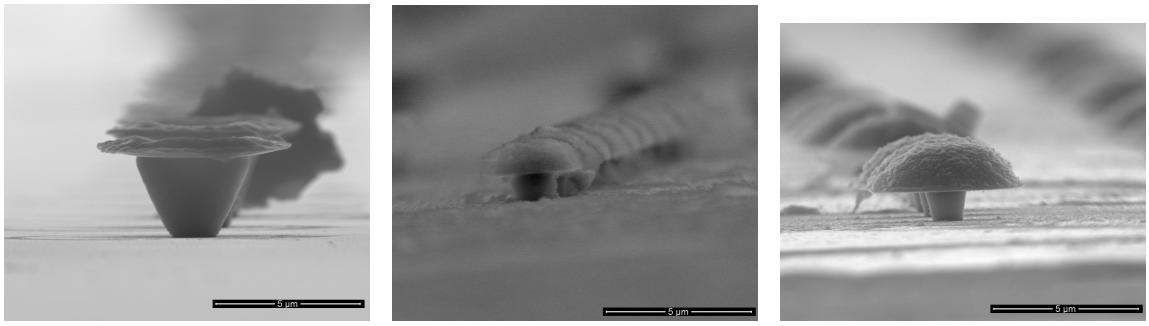

(A) Solution 1 (1:1) (B) Solution 2 (1:5) (C) Solution 3

FIGURE 4.9: **Profile view of the PEDOT:PSS-mushroom electrodes for the three different solutions, with equal deposition time and applied potential.** Scale bar of $5\mu m$

are summarized in Table. 4.2, for the cap diameter (Cd), stalk diameter (Sd) and the total mushroom height (Mh), which includes the stalk and cap height. It is relevant to note that the fuzzy patterned observed around the structures is caused by charge accumulation in the sample due to the non-conductive glass substrate. From the information of Table. 4.2,

Concentrations	**Cd (μm)**	**Sd (μm)**	**Mh (μm)**
1:1	4.758	1.856	3.053
1:5	3.588	2.276	4.126
1:11	4.238	2.105	5.209
1:11*	3.521	2.059	4.175

TABLE 4.2: **Size of the features from the different electrodes.** To note that this are the average sizes

we are then able to obtain the deposition rate for the three produced samples, which are: 846 nm/min, 1044 nm/min and 1340nm/min for solutions 1, 2 and 3, respectively. As expected, the cap diameter is directionally correlated to the EDOT concentration and this can be seen in Fig. 4.9 were a conjoint increase of the cap diameter to the polymer concentration is observed. With the intent of producing an homogeneous array of mushrooms from solution 3, we electrodeposited a new sample but this time for 3 minutes. The resulting structure can be seen in Fig. 4.10 side by side with the longer deposited sample. Analysing the image of the new electrodes we see that these have an average cap diameter of $3.521 \pm 0.003\mu m$, very similar to the ones produced with solution 2 with a deposition time of 4 minutes. Thus, we were able to produce two arrays of mushroom-shaped PEDOT:PSS electrodes with solution 2 and 3 for different deposition times and volcano-shaped PEDOT:PSS electrodes for solution 1.

*Electrodeposited for 3 minutes

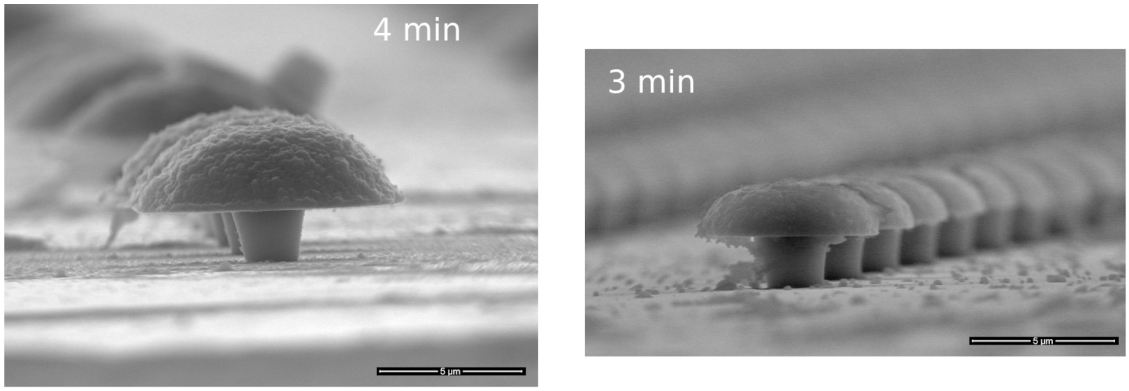

FIGURE 4.10: **Profile view comparison of PEDOT:PSS grown mushroom-electrodes with solution 3 for different times.** The results for 4 minutes (left) and 3 minutes (right) of deposition. Scale bar of $5\mu m$

4.3.1.1 Impedance spectroscopy study

To analyse the evolution of the PEDOT:PSS-mushroom electrodes resistance and capacitance with frequency, we performed impedance measurements with the setup seen in Fig. 4.11. To perform these measurements we used an anodization cell to only allow for the mushroom arrays area to be exposed, and then we emerged them into a PBS (phosphate buffered saline) solution of 1 mL. In these measurements we used a LabvieW routine, where the frequency and the number of points, is chosen.

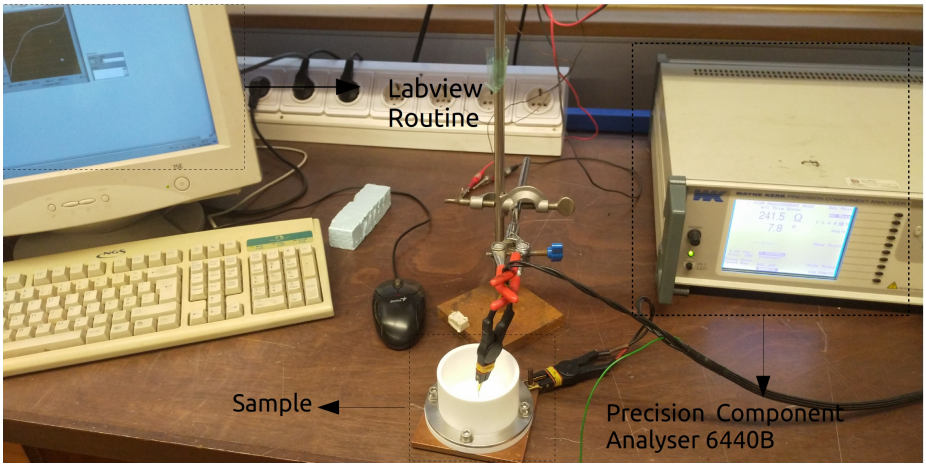

FIGURE 4.11: Impedance measurement setup

The device used to perform the measurements was a Precision Component Analyzer 6440B, from Wayne Kerr Electronics and the chosen model was of a parallel RC. The data returned from this measurements gave the magnitude and phase of the impedance, which can be then decomposed into a real part corresponding to a resistance and an imaginary

part corresponding to a reactance, which includes the capacitive or inductive parts. Because the chosen model was that of a parallel RC, the imaginary part corresponds to a capacitor, while the real part is the resistance of the set PBS/microelectrodes. In this study we measured the performance of the electrodes from the most concentrated solution (1:11) to the least one (1:1). Furthermore, to have a way to equate the performance of these newly produced electrodes, we analysed also a sample with gold-mushroom electrodes. In Fig. 4.12, it is then possible to compare the resistance and capacitance behaviour between the two different samples of PEDOT:PSS-mushroom and the gold-mushrooms. Fig. 4.12 a) * indicates that the resistance value of the produced PEDOT:PSS-mushrooms is significantly lower in comparison to the golden ones. For high frequencies (in the Mhz), the resistance values tend to 100-150 Ω for the PEDOT:PSS and to 250 Ω for gold. In the region of interest for neurological studies (100-1000Hz) the resistance values vary between 150-250 Ω for the PEDOT:PSS and between 350-500 Ω for the gold. In Fig. 4.12 b) we observe the capacitance values of the set PBS/microelectrodes. The graph shows that for frequencies above kHz there is a sharp decline in the capacitance value, leading to a convergence of all the measurements to the same value. Analysing the values for frequencies below kHz, we observe once again a better performance of the PEDOT:PSS mushrooms over the gold ones, specially in the 100-1000 Hz zone, essential to neuronal signal acquiring. In this range, the capacitance varies between 3-50 nF for the PEDOT:PSS and between 1-25 nF for the Au. This study allowed us to prove that the mushrooms grown with the conductive polymer have a lower resistance and higher capacitance than the gold ones, specially in the range of 100-1000Hz.

Finally, with this measurement we were able to see which PEDOT to PSS ratio yielded the best results in terms of resistance and capacitance, which was the electrodes grown with solution 1. This can be explained by the excess PSS acting as an insulating barrier, hindering the charge transport within the film [119].

4.3.1.2 Polymer growth

Our work has shown that it is indeed possible to grow mushroom-shaped electrodes of PEDOT:PSS. However, the size of the features (the cap's diameter, more specifically) produced may not be the ideal for neuron coupling. As shown by Ojovan *et al* [40], caps larger than 2.5 μm may prevent engulfment by the small mammalian neurons. Taking

*Similarly to the deposition curves, the results of solution 2 and 3 were practically indistinguishable. As such, we choose to omit the results of solution 2 to provide a better visualization.

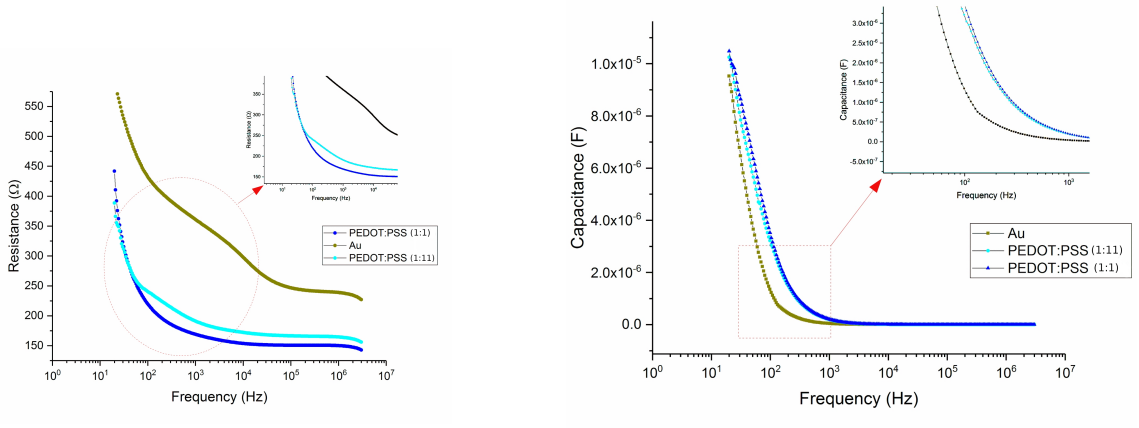

(A) Resistance (B) Capacitance

FIGURE 4.12: Impedance studies for the PEDOT:PSS-mushroom and gold electrodes

into consideration that the cap's diameter of the electrodes varies between 3 to 5 μm, this can affect the coupling coefficient. Nevertheless, this can be prevented by using a different configuration type of MEA. The islet type configuration, used by Mateus *et al* [36] for GMμEs, where each electrode path terminated in an array of 3x3 electrodes instead of just one, has demonstrated that this topography greatly increases the cell-electrode contact surface, thus enhancing the coupling coefficient.

This work may also have shed a new perspective on how polymer films grow inside confined environments. By observing the produced samples of solution 1, seen in Fig. 4.8 a) and Fig. 4.9 a), we were surprised to find a volcano like structure instead of a flat top. If the polymer growth inside the microtubes is uniform, then a flat top should by produced when the deposition time is not enough to grow the full cap. However, to produce a cap with only its edges and a depression in the center, leads us to infer that the growth is not uniform. In fact, to achieve such a structure, the polymer must grow first around the walls of the microtubes and then in its nucleus. This was further confirmed by the deposition of an array of 10 μm holes in diameter that was situated in the same substrate of the array used with solution 1. The outcome of this deposition (with solution 1, for 4 minutes at 0.8 V), is shown in Fig. 4.13. This PEDOT:PSS structure has a pie aspect, and in this case it is clear to observe that, due to insufficient deposition time for such a large diameter, only the walls of the structure were grown leaving a hollow center. This hints at the possibility that the growth mechanism is governed by two stages; diffusion and charge transfer. This would mean that, in the initial deposition step the number of electrodeposited oligomers

(PEDOT) is probably low and this process is controlled by diffusion of the monomers from the bulk solution. This initial slow deposition may cause the deposited oligomers to aggregate together to minimize energy and doing so in a ring-like form around the micro-tube walls. The reason of this configuration is perhaps due to the polymer being constituted of long chains of oligomers. After this initial phase, the growth process is controlled

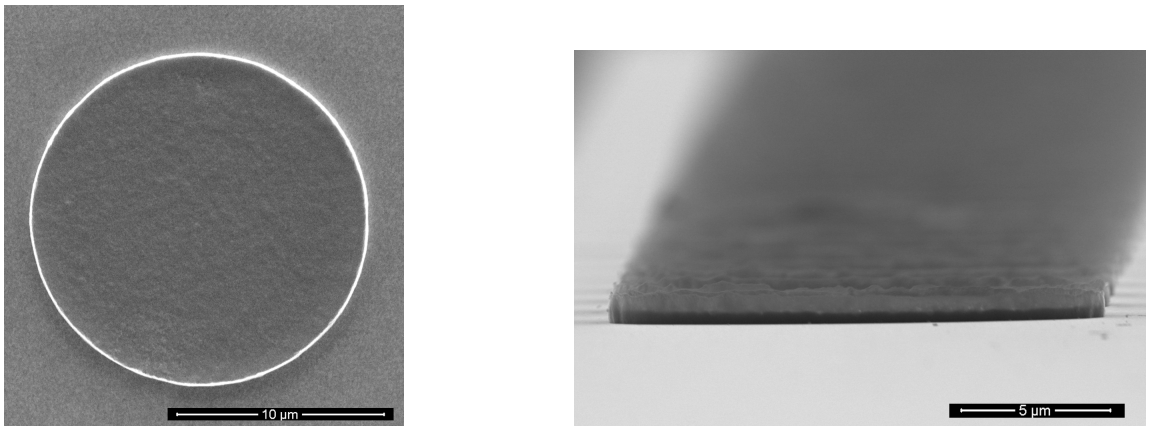

(A) Top view (B) Profile view

FIGURE 4.13: SEM images of the structures grown with solution 1 on 10 μm diameter holes.

by a charge transfer process which would lead to an instantaneous nucleation, explaining the quick formation of the whole nucleus of the structures. This mechanism of growth could induce a volcano structure, as discussed in [120]. The monomer concentration can also have an effect on the growth mechanism, as noted by Gao et al [121], which discovered that a higher monomer concentration led to less uniform tubular structures with thicker walls, whilst a solution with lower monomer concentration led to a more uniform structure with thinner walls. After our work, we discovered that, using a galvanostatic or potentiodynamic mode for electrodeposition results in electrode coating with a more uniform morphology than those grown in a potentiostatic way. This is due to a non-uniform current distribution on the electrodes and is more pronounced when operating in potentiostatic mode [105, 122]. However, as noted by Bartsch *et al* [103], a rougher surface may be better for neuron coupling, thus making the potentiostatic method the best option. As a final remark, the volcano-shaped electrode seen in Fig. 4.8 a) and Fig. 4.9 a) may indeed present advantages over the mushroom-shaped electrodes. In a recent paper, Desbiolles *et al* [123], fabricated nano-volcano electrodes which were able to gain intracellular access for long periods of time, thus enabling the recording of intracellular signals.

Chapter 5

Electrical simulations

In this chapter we will present a brief description of electrical simulations performed on the influence of the mushroom-shaped electrode's parameters in relation to the acquired signal from the neuronal cells and the coupling coefficient (CC), which is the ratio between the electrical signal measured by the electrodes and the signal that passes inside a neuron.

The simulations were done with the open source software *Ngspice 31.0*, which allowed us to simulate the behaviour of an electrical circuit. In our program we simulated a neuron coupled to a mushroom-shaped electrode. For the neuron modelling we utilized the code, kindly provided by Giuseppe Massobrio, the scheme of which is show in Fig. 5.1 a). As previously explained in Section 2.1.1.2, the Hodgkin and Huxley (HH) formalism is translated into an electric circuit made up of linear capacitors and non-linear time-invariant resistive elements. However, in their code Massobrio *et al* [15], redefined the HH model such that the potassium activation parameter and the sodium activation and inactivation parameters are proportional to a state voltage-variable of a linear capacitor. This enables a reformulation of the linear time-varying conductance currents to be replaced by sub-circuits in *Ngspice*. The electrode coupling to the neuron is depicted in Fig.5.1 b). The circuit is divided in four main blocks: Protein-Glycocayx electric double layer (EDL), Cleft effects, μelectrode-electrolyte interface and finally the mushroom-μelectrode. We will now provide a brief explanation of these sub-circuits, as a more detailed account is presented in Section 2.1.1.2. The Protein-Glycocayx EDL models the EDL originated at the side of the neuronal membrane, the cleft effects represents the geometric surface area of the μelectrode as well as the resistance generated by the solution within the gap between the surface of the μelectrode, the μelectrode-electrolyte interface models the EDL generated at the μelectrode side which is dependent on the device characteristics. Finally

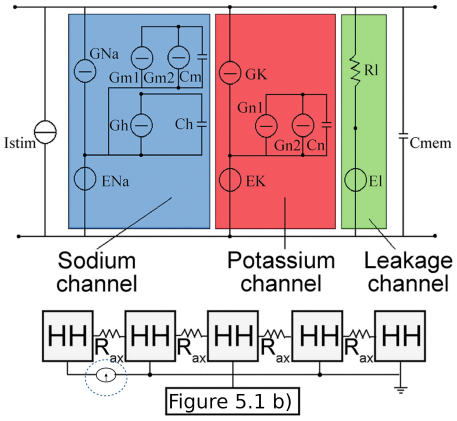

(A) Top: *Ngspice* implementation of a single compartment HH model circuit. Bottom: schematic representation of the compartmental approach. Adapted from [15].

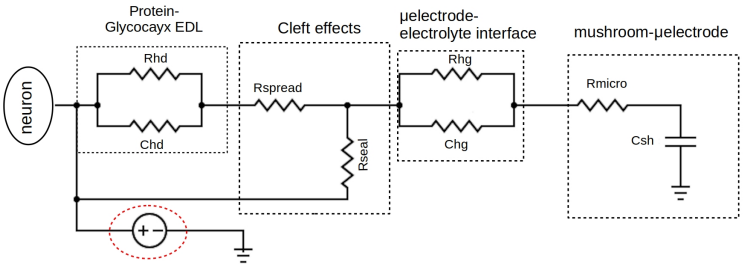

(B) Schematic of a neuron coupled to a mushroom-shaped microelectrode.

FIGURE 5.1: **Schematic drawings of the analog electrical circuits used.** The *Ngspice* implementation of the HH model circuit (a), which is coupled to the microelectrode (b)

the mushroom-μelectrode models the μelectrode resistances in respect to its area and the parasitic shunt resistance.

The simulations reviewed in Section 2.3.5 focused on the impact that the seal resistance or the neuron coupling had on the CC and none explored the possibility of studying the effects of altering the resistance or the capacitance of the μelectrode itself. The big advantages of this equivalent circuit model is that it permits to evaluate and improve the features of microtransducers in recording the neuronal electrical activity, before its fabrication. As such, we used this circuit to validate if the CC value would benefit from substituting the gold-mushroom electrode by a PEDOT:PSS one. For these effect we searched the current literature for a range of experimental values of μelectrodes coated with PEDOT:PSS [107, 124–128] and found that the resistance of this devices ranged from 300 K Ω to 1000 M Ω and the capacitance varied between 10-90 nF*. To test the effects of varying

*These measurements were performed at 1 kHz

the resistance and capacitance of μelectrode, we first simulated a voltage calibration pulse delivered to the bathing solution, seen in Fig.5.1 surrounded by the red circle, with an amplitude of 1 mV with a duration of 20 ms (in this simulation, the pulsed current source is not present). All the other parameters, except the μelectrode resistance (Rhg) and capacitance (Chg), are taken from Ref [15] and can be found in the Appendix section D. The signal acquired by the μelectrode is presented in Fig. 5.2 in comparison to the voltage pulse. From these simulations we found that lowering Rhg enhances the acquired signal and also that the signals simulated for the Rhg range of the PEDOT:PSS resistances provide a signal with less attenuation than the one simulated with the Rhg of the gold-mushroom electrode (1500 GΩ), as can be observed in Fig. 5.2 a). From the sweep of the Chg value we concluded that this parameter plays an important role in modulating the time constant of the square signal acquired by the μelectrode, where higher capacitance values provided a faster rise time as seen in Fig. 5.2 b). This analysis showed that a lower impedance and higher capacitance (which are the characteristics of PEDOT:PSS μelectrodes) provided a better signal quality and then we studied how this affected the neuronal signal acquisition. For this effect, we removed the voltage source and introduced a pulsed current source of 1 nA [blue circle in Fig. 5.1 a)] into the neuron compartment with a frequency of 100 Hz and a duration of 1 ms. The intention of the parameters used in this current source was to mimic membrane oscillation potentials, which are of uttermost importance for *in vitro* drug screening for the development of personalized medicine and have not yet been recorded experimentally by gMμEs. As such, we simulated three PEDOT:PSS μelectrodes and compared their performance to the gold μelectrode. The parameters of these devices and corresponding CC value are summarized in Table.5.1. For the PEDOT:PSS devices we used a combination of the parameters within the range of those experimentally reported in the literature. The current injection into the neuron compartment evoked an action

Mushroom-shaped μelectrode device	**Resistance**	**Capacitance**	**Coupling Coefficient**
Gold	1500 GΩ	5 pF	0.055
PEDOT:PSS 1	100 MΩ	500 pF	0.111
PEDOT:PSS 2	5000 kΩ	1 nF	0.172
PEDOT:PSS 3	1000 kΩ	10 nF	0.272

TABLE 5.1: Different simulated μelectrode devices with the parameters used and the corresponding CC values obtained from the simulations

potential of $\sim$ 180mV, which was recorded at the neuron-Protein-Glycocayx interface,

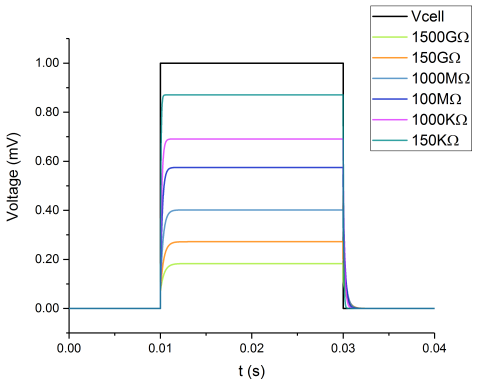

(A) Impedance parameter sweep.

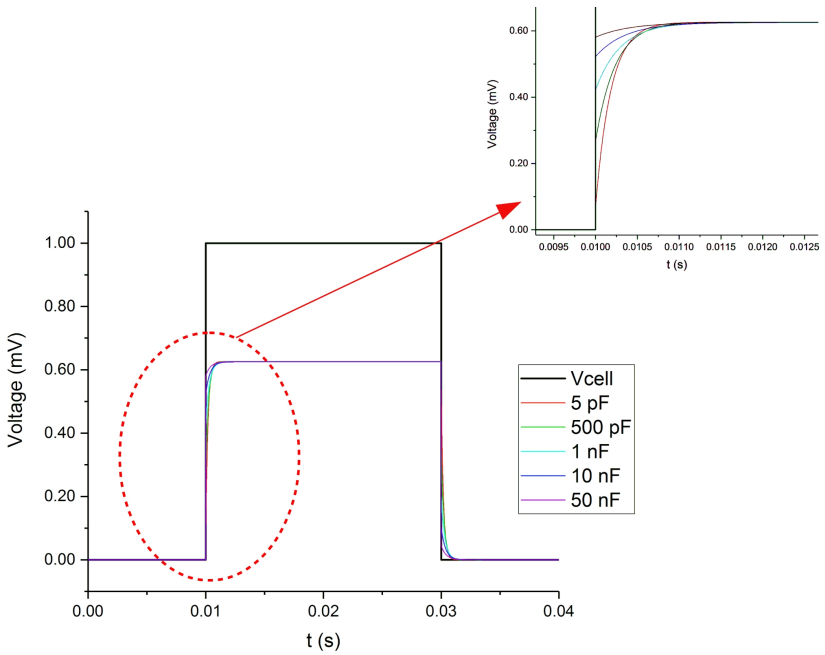

(B) Capacitance parameter sweep. The inset shows a zoomed view of the rise region.

FIGURE 5.2: **μelectrode parameters influence in the acquired signal from a voltage pulse delivered to the bath solution** μelectrode impedance (a) and capacitance (b) comparisons.

seen in Fig. 5.3 as "Vintra". The signals acquired by the various simulated μelectrodes are shown in Fig. 5.3 and present the characteristic attenuation of "in-cell" recording. By analysing the various recorded signals, we see that, by using a μelectrode with lower impedance, the signal gets less attenuated and also, as previously discussed, by raising the capacitance, the shape of the signal approximates more to the shape of the intracellular recorded action potential (AP). This can be clearly seen in the zoomed view of Fig. 5.3 b).

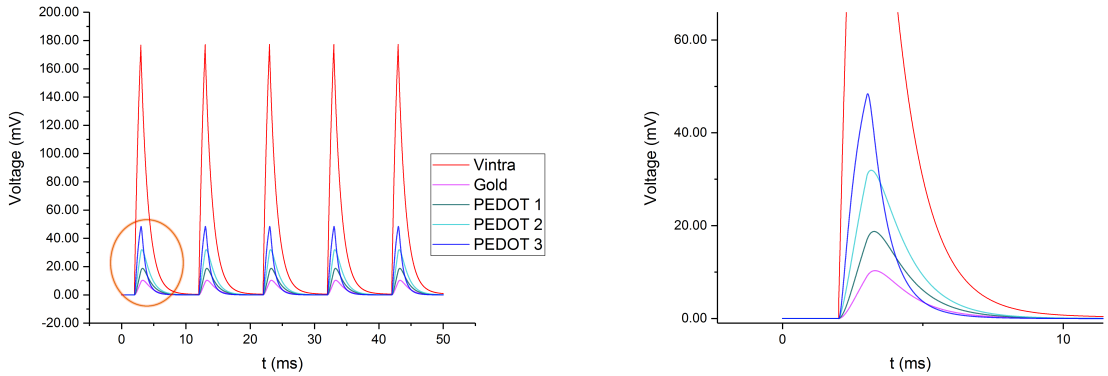

FIGURE 5.3: **Simulation of different μelectrodes and their influence on neuronal recordings.** The simulation was done for different PEDOT:PSS, with parameters from worse to best, in comparison to a gold-μelectrode (a); The zoomed view of the red circled region (b).

However, it is also very important to note that all the signals here indicate that the μelectrode is working in an Ohmic regime and thus is enabling "in-cell" recording modes, in contrast to the signals acquired by planar μelectrodes which approximate to a time derivative of the input signal (Section 2.3.5.4 provides an explanation of this phenomena). This means that, even the gMμE in theory should be able to record signals of 100 Hz. Unfortunately, until now, there has not been a successful experimental report of this feat, as discussed in section 2.3.7. Nevertheless, in theory, these devices indeed offer a better CC than the gMμEs, as shown in Fig. 5.3 and Table 5.1. It has also been show that PEDOT:PSS surfaces provide a better neuron coupling [97, 106, 124], which also contributes to a better CC value. As such, interfacing neurons with PEDOT:PSS-mushroom shaped μelectrodes could enable, for the first time, the recordings of synaptic and membrane oscillations without cell invasive techniques.

Chapter 6

Conclusion and future work

The rate at which all fields of science are developing is astounding, provoking, almost every day, moments of awe in one's life. Difficult problems being solved by brilliant solutions. Nevertheless, in some situations, the answer takes years to come. This was the case with how could one record neuronal signals intracellulary without evasive techniques. One of the answers to this problem, and the simplest in implementation by far, was to use gold-shaped microelectrodes instead of planar ones. This approach was successful in acquiring neuronal recordings of action potentials. Unfortunately, for membrane and synaptic oscillations these devices are not sufficient, because these signals get attenuated to the noise level of the amplifier. With the aim of overcoming this obstacle, we decided to combine the low impedance and high capacitance provided by the conducting polymer PEDOT:PSS with the mushroom-shaped electrodes, fabricating for the first time mushroom-shaped microelectrodes constituted entirely by PEDOT:PSS. In parallel, because the attenuation of the neuronal recordings is diminished by the use of microfluidic devices, we decided to also reproduce two types of these devices, with one of those never being reproduced with a Direct Write System (DWS) machine before. In respect to these two components, we demonstrated the experimental procedure and optimization steps to create these devices.

For the fabrication of the microfluidic devices, we first optimized the parameters for the alignment marks, done with a positive S1818 photoresist where the transferred patterned utilized a power of 20 mW with a PPD of 22%. Using an adhesion layer of SU-8 3005 with a thickness of 5 μm before the first and second layers proved successful in

preventing the structures to drift during bake times. The parameters for the first and second layers were then optimized to a spinner velocity of 2400 rpm and 1000 rpm and an exposure power of 40 mW at 40% and 60 mW at 40%, respectively. In the case of the stomach design, the lithography problem pertaining to the impossibility of seeing the WSP through the second layer in the DWS machine was overcome by using a sacrificial zone. These molds were then successfully replicated by casting PDMS at 750 rpm and 1000 rpm for the first and second layers, respectively.

In respect to the microelectrodes, a first experimental study was done to optimize the 2 μm dot sizes Direct Write system, which were obtained for 12 mW at 18% PPD. With these parameters, we then exposed microdot arrays of 2x2 mm where the PEDOT:PSS would be later grown. Afterwards, we made 3 different concentration solutions of EDOT:PSS and studied the best potential to electroplate the structures. This was determined to be at 0.7 V for the first solution with EDOT to PPS concentration of 1:1 and 0.8 for the other two (1:5 and 1:11). Next, we did deposition tests to determine the growth rate of the PEDOT:PSS films at the gold surface. Finally, the PEDOT:PSS-mushroom shaped microelectrodes were created by depositing at 0.8 V for 4 minutes for all the solutions in the potentiostatic mode. These structures were then analysed with SEM, making possible to characterize the microelectrodes features sizes. With these images we discovered that the deposition time for solution 3 (1:11) was too large and performed another deposition for 3 minutes which proved to be fitting. The successful depositions for the three different solutions had a cap diameter of 4.75, 3.58 and 3.52 μm and a total height of 3.05, 4.126 and 4.175 μm. We then tested the performance of the mushroom-shaped PEDOT:PSS microelectrodes of solution 1:1 and 1:11 against the gold-shaped ones in a PBS bath. The results of this experiment showed that the PEDOT:PSS microelectrodes have a lower impedance and higher capacitance in comparison to the gold microelectrode, which are crucial parameters for neuronal signal acquiring as proved in our simulations. Finally, we tested the performance of the mushroom-shaped PEDOT:PSS microelectrodes of solutions 1:1 and 1:11 against the gold-shaped ones in a PBS bath. The results of this experiment showed that the PEDOT:PSS microelectrodes have a lower impedance and higher capacitance in comparison to the gold microelectrode, which are crucial parameters for neuronal signal acquiring as proved in our simulations.

In relation to the fabrication process, we recommend substituting the deionized water environment of the EDOT:PSS solution to an organic solvent to decrease the time to reach homogeneity and enhance the electrical conductivity. We also advise do the depositions under N_2 atmosphere to prevent oxygen oxidation in the electrolyte bath. As future work, we propose the implementation of these microelectrodes in a MEA configuration to open the possibility of testing each electrode electrical response. The next step would be to interface these new MEAs with neuronal cells and also in the context of microfluidic devices, in order to evaluate if they are indeed successful at recording synaptic and membrane oscillations.

Appendix A

Appendix

Run Sheet
uEF Chamber Design

Process Start _____ **Process Finish** _____

Substrate: Glass (Silica)
Cleaning: 5 minutes acetone bath, 5 minutes isopropanol bath and then clean with deionized water.

STEP 1 **1st Lithography –** Alignment marks definition Date: ___/ ___/ ___

Machine: Direct Write uPG 101

1) Spin Coating and pre-bake

Photoresist: S1818
Thickness: 2 µm

Spinner parameters:
v = 3000rpm
a = 1000rpm/s
t = 30s

Pre-Bake at 115ºC for 60s
Cool down at ambient temperature for 5 minutes

2) Mask exposure (DWL)

Mask: uEF_Chamber_0.dxf
Machine: Upg101

Pixel Pulse Duration: 22%
Power: 20mW

Writing starting point (WSP): Should be inside the circle below

Inset here the corresponding Autocad layer for this lithography step:

2) Develop:

Proportion 3:1 (De-ionized water:developer) Developer: Microposit 351
Time: 60s

3) Al thin film deposition:

Machine: IBD (por mais especificações)

Target	**Pw (Torr)**	**Ar flux (sccm)**	**VD (V)**	**ID (A)**	**VB (V)**	**VA (V)**	**Rotation (rpm)**
Al							

4) Lift-off photorestist layer:

Acetone bath for 5 minutes in ultra-sound

STEP 2 **2nd Lithography –** Adhesion layer definition Date: ___/ ___/ ___

1) Dehidratation bake:

T=115º C ; t=10min

2) Spin Coating:

Thickness: 5 µm

Spinner Parameters	v(rpm)	a(rpm/s)	t(s)
Step 1	200	500	20
Step 2	3000	500	45

3) Pre-bake:

First bake: T=65º C; t=1min
Immediately followed by
Second bake: T=95ºC; t=5min

4) Flood Exposure:

Machine: Mask Aligner (Karl Suss) Energy: 300mJ/cm^2
Time: 30s

5) Post-Exposure Bake:

T=95ºC; t=5min
Rest at T_{amb} for 10 minutes

STEP 5 **3rd Lithography**: First layer definition Date:_/ _____/ _____

1) Spin Coating:

Thickness: 10 µm

Spinner Parameters	v(rpm)	a(rpm/s)	t(s)
Step 1	200	500	20
Step 2	2400	500	45

2) Pre-Bake:
First bake: T=65º C; t=1min
Immediately followed by
Second bake: T=95ºC; t=5min

3) Mask exposure (DWL)

Mask: uEF_Chamber_1.dxf
Machine: Upg101

Pixel Pulse Duration: 40% WSP: The X and Y coordinates of the lower edge rectangle seen below
Power: 40mW

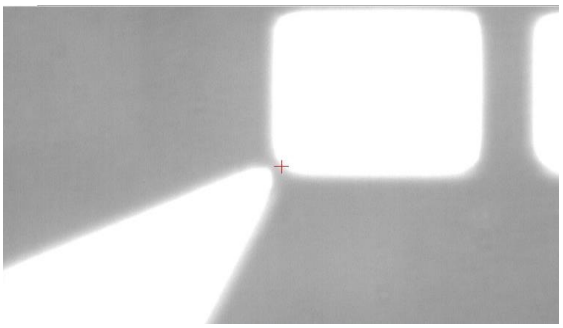

Inset here the corresponding Autocad layer for this lithography step:

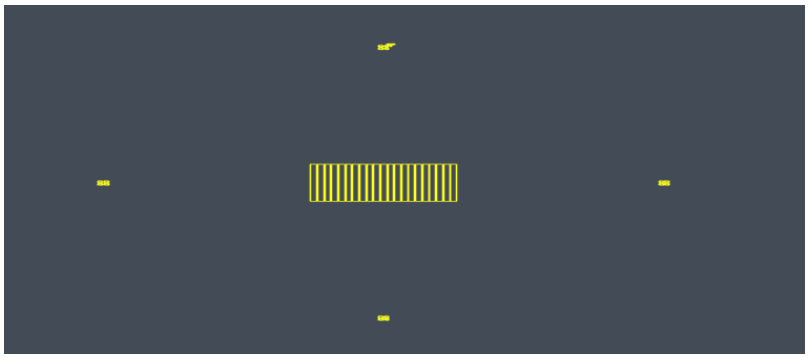

4) Post-Exposure Bake:

T=65ºC; t=1min

STEP 6 **4th Lithography:** Second layer definition Date: _____/ _____/ __

1) Spin Coating:

Thickness: 100 µm

Spinner Parameters	v(rpm)	a(rpm/s)	t(s)
Step 1	200	500	20
Step 2	_____	500	45

2) Pre-Baking:

Hot-Plate Parameters	T(ºC)	Ramp(ºC/min)	t(min)
Step 1	65	10	5
Step 2	95	10	45
Step 3	20	2	10

3) Mask exposure (DWL)

Mask: uEF_Chamber_2.dxf
Machine: Upg101

Pixel Pulse Duration: 40%
Power: 60mW

WSP: The same as in the previous step

Inset here the corresponding Autocad layer for this lithography step:

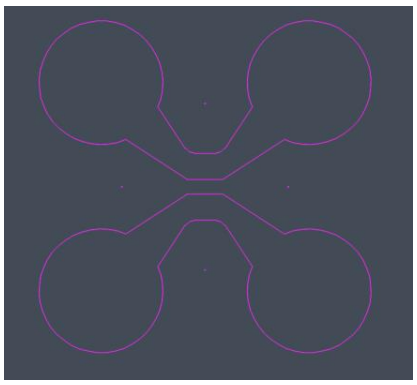

4) Post-Exposure Bake:

Hot-Plate Parameters	T(ºC)	Ramp(ºC/min)	t(min)
Step 1	65	10	1
Step 2	95	10	35
Step 3	20	2	10

5) Develop (Ultrasonic bath):

Developer: SU-8 developer
t=____min
Note: Be careful to always know where the photoresist side is!

Optical Inspection:

Sample	**Comments**

STEP 7 **PDMS** Date: ___/ ___/ ___

Thickness: 100 µm
Base Agent: Dimethyl
Curing Agent: Methylhydrogen Siloxane
Base to curing agent ratio: 10:1
Mix the two agents in a glass container, then leave in vacuum until all air bubles disappear

PDMS application:
Cover the desired area entirely
Speed: 1000 rpm Duration: 30 s

Curing bake: 80ºC for 3 hours.

Remove carefully with the help of Kapton tape.
Place in the desired substrate

Optical Inspection:

Sample	Comments

Date: _____/ _____/ ___

Appendix B

Appendix

Run Sheet
Stomach Design

Process Start _____ **Process Finish** _____

Substrate: Glass(Silica)
Cleaning: 5 minutes acetone bath, 5 minutes isopropanol bath and then clean with deionized water.

STEP 1 **1st Lithography –** Alignment marks definition Date: ___/ ___/ ___

Machine: Direct Write uPG 101

1) Spin Coating and pre-bake

Photoresist: S1818
Thickness: 2 µm

Spinner parameters:
v = 3000rpm
a = 1000rpm/s
t = 30s

Pre-Bake at 115ºC for 60s
Cool down at ambient temperature for 5 minutes

2) Mask exposure (DWL)

Mask: **Stomach_layer_0.dxf**
Machine: Upg101

Pixel Pulse Duration: 22%
Power: 20 mW

Writing starting point (WSP): Should be inside the circle below

Insert here the corresponding Autocad layer for this lithography step:

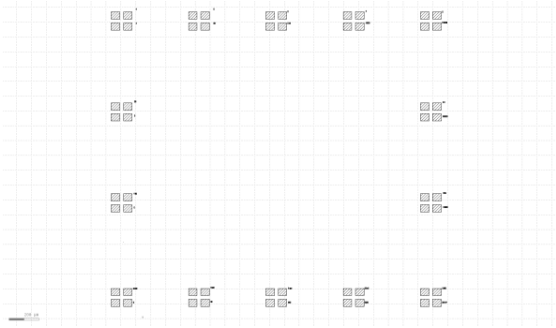

2) Develop:

Proportion 3:1 (De-ionized water:developer) Developer: Microposit 351
Time: 60s

3) Metal Deposition:

Al 100 nm

Machine: IBD

Target	Pw (Torr)	Ar flux (sccm)	VD (V)	ID (A)	VB (V)	VA (V)	Rotation (rpm)
Al							

4) Lift-off photorestist layer:

Acetone bath for 5 minutes in ultra-sound

STEP 2 **2nd Lithography –** Adhesion layer definition Date: ___/ ___/ ___

1) **Dehydration bake:**

   T=115º C ; t=10min

2) **Spin Coating:**
   Thickness: 5 µm

Spinner Parameters	v(rpm)	a(rpm/s)	t(s)
Step 1	200	500	20
Step 2	3000	500	45

3) Pre-bake:

First bake: T=65º C; t=1min
Immediately followed by
Second bake: T=95ºC; t=5min

4) Flood Exposure:

Machine: Mask Aligner (Karl Suss) Energy: 300mJ/cm^2
Time: 30s

5) Post-Exposure Bake:

T=95ºC; t=5min
Rest at T_{amb} for 10 minutes

STEP 5 **3rd Lithography**: First layer definition Date:_/ _____/ _____

1) Spin Coating:

Thickness: 10 µm

Spinner Parameters	v(rpm)	a(rpm/s)	t(s)
Step 1	200	500	20
Step 2	2400	500	45

2) Pre-Bake:
First bake: T=65º C; t=1min
Second bake: T=95ºC; t=5min

3) Mask exposure (DWL)

Mask: Stomach_layer_1.dxf
Machine: Upg101

Pixel Pulse Duration: 40% WSP: The X and Y coordinates of the lower edge rectangle seen below
Power: 40mW

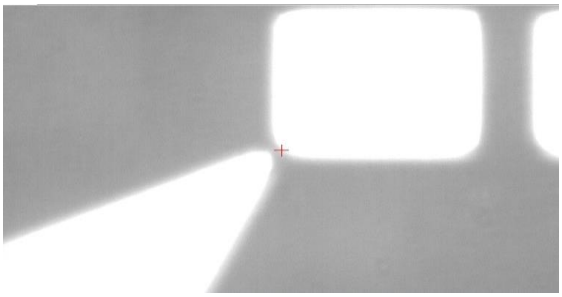

Insert here the corresponding Autocad layer for this lithography step:

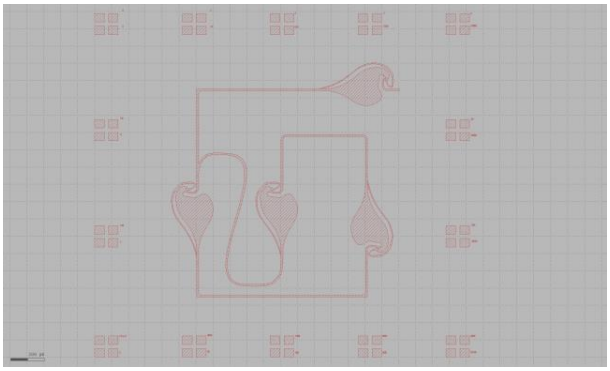

4) Post-Exposure Bake:

T=65ºC; t=1min

STEP 6 **4th Lithography:** Second layer definition Date: _____/ _____/ __

1) Spin Coating:

Thickness: 100 µm

Spinner Parameters	v(rpm)	a(rpm/s)	t(s)
Step 1	200	500	20
Step 2	_____	500	45

2) Pre-Baking:

Hot-Plate Parameters	T(ºC)	Ramp(ºC/min)	t(min)
Step 1	65	10	5
Step 2	95	10	45
Step 3	20	2	10

3) Photoresist Strip:

Use cotton tips and the cleanroom paper with acetone to remove the photoresist covering the area of the alignment mark The remove area must be enough so that the DWL head writer can lower down without touching any photoresis

Note: Be very careful with the acetone not to touch the photoresist area to be exposed

4) Mask exposure (DWL)

Mask: Stomach_layer_2.dxf
Machine: Upg101

Pixel Pulse Duration: 40%
Power: 60mW

WSP: The X and Y coordinates of the lower edge rectangle seen previously

Inset here the corresponding Autocad layer for this lithography step:

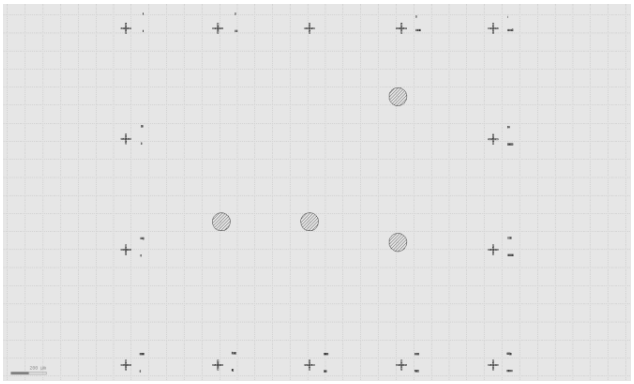

Note: Because of the removal of roughly half of the photoresist area from the substrate the normal procedure must be modified to not damage the writing head of the direct writing machine. The steps are (in sequential order)

- Center the stage
- Move the laser head to the area where the photoresist was removed
- Automatic Focus
- Search and enter the WSP coordinates
- De-Focus
- Move the laser head to the area where there is photoresist in the substrate
- Automatic Focus
- Write

5) Post-Exposure Bake:

Hot-Plate Parameters	T(ºC)	Ramp(ºC/min)	t(min)
Step 1	65	10	1
Step 2	95	10	35
Step 3	20	2	10

6) Develop (Ultrasonic bath):

Developer: SU-8 developer t=____min

Note: Be careful to always know where the photoresist side is!

Optical Inspection:

Sample	**Comments**

STEP 7 **PDMS** Date: ___/ ___/ ___

Thickness: 50 µm
Base Agent: Dimethyl
Curing Agent: Methylhydrogen Siloxane
Base to curing agent ratio: 10:1
Mix the two agents in a glass container, then leave in vacuum until all air bubles disappear

PDMS application:
Cover the desired area entirely
Speed: 750 rpm Duration: 30 s

Curing bake: 80ºC for 3 hours.

Remove carefully with the help of Kapton tape.
Place in the desired substrate

Optical Inspection:

Sample	Comments

Date: _____/ _____/ ___

Appendix C

Appendix

Run Sheet

PEDOT:PSS-Mushrrom Shaped Microelectrodes

Process Start _____ **Process Finish** _____

Substrate: Glass- Si/ Cr 3 nm/Au 30-40 nm
Cleaning: 5 minutes acetone bath, 5 minutes isopropanol bath and then clean with deionized water.

STEP 1 **1st Lithography –** Array definition Date: ___/ ___/ ___

Machine: Direct Write uPG 101

1) Spin Coating and pre-bake

Photoresist: S1818
Thickness: 2 µm

Spinner parameters:
v = 2500rpm
a = 1000rpm/s
t = 35s

Pre-Bake at 115ºC for 60s
Cool down at ambient temperature for 5 minutes

2) Mask exposure (DWL)

Mask: **Stomach_layer_0.dxf**
Machine: Upg101

Pixel Pulse Duration: 22%

Power: 20 mW

Writing starting point (WSP): Should be in the center of the sample, use the DWL software for searching the center

Insert here the corresponding Autocad layer for this lithography step:

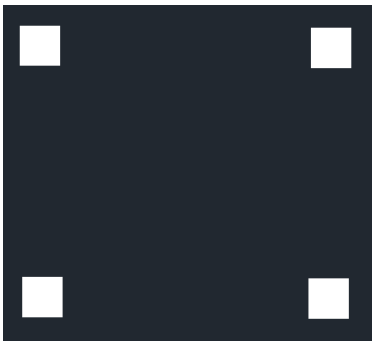

2) Develop:

Proportion 3:1 (De-ionized water:developer) Developer: Microposit 351
Time: 60s

Note: See if all pores are open with the microscope

Optical Inspection:

Sample	Comments

STEP 2 **EDOT:PSS solution preparation** Date: ___/ ___/ ___

1) Quantities:

EDOT: 375 µL
PSS: 4.79 mL
Deionized water: 100 mL

2) Mixing:
Fill a glass container with the Deionized water and add the EDOT and PSS
Place the glass in a magnetic agitator at 300 rpm
Wait at least 24h, remove when the solution has reached homogeneity

STEP 5 **EDOT:PSS polymerization and deposition** Date:__/ _____/ _____

1) SETUP:

Use the thee electrode setup at the Alumina lab ,
Reference electrode: Ag\AgCl
Counter Electrode: Pt mesh
Use the Labview program “Deposition S1”
Note: Be carefull to keep the distance between electrodes at minimum possible
Place the electrical cables at the current source accordingly !

Deposition Parameter	Potentia l (V)	Time (min)
Electrode	0.8	4

Post Deposition:
Wash with deionized water and observe the sample at the microscope to see if the deposition was successful.

Optical Inspection:

Sample	**Comments**

If the deposition is successful, remove the photoresist layer with acetone and wash with deionized water.

Appendix D

Appendix

	r_{soma} (µm)	r_{axon} (µm)	l_{axon} (µm)	A_{Neuron} (µm^2)	E_{Na} (mV)	E_K (mV)	E_L (mV)	$\bar{g}_{Na}$ (mS/cm^2)	$\bar{g}_K$ (mS/cm^2)	$\bar{g}_L$ (mS/cm^2)	C_{mem} (µF/cm^2)
neuron model	50	5	500	$47.1 \cdot 10^3$	115	-12	10.6	120	36	0.3	1

	r_{stalk} (µm)	h_{stalk} (µm)	r_{head} (µm)	$A_{GMµE}$ (µm^2)
GMµE	0.5	1.0	1.0	10.21

	d_j (nm)	ρ_s (Ω·m)	ρ_{Au} (nΩ·m)	ρ_{glyco} (MΩ·m)	ε_{glyco}	ε_s	ε_{lys}	t_{glyco} (nm)	γ
GMµE	5.0	0.7	22.7	1.6	81.0	78.5	3.0	100.0	1

	R_{hd} (GΩ)	C_{hd} (pF)	R_{spread} (kΩ)	R_{seal} (MΩ)	R_{hg} (GΩ)	C_{hg} (pF)	R_{micro} (Ω)	C_{sh} (pF)
GMµE	15.67	0.073	55.21	40.16	$1.5 \cdot 10^3$	5.0	$18.06 \cdot 10^{-3}$	$1.37 \cdot 10^{-3}$

Bibliography

[1] Human Physiology/The Nervous System - Wikibooks, open books for an open world. [Online]. Available: https://en.wikibooks.org/wiki/Human_Physiology/The_Nervous_System

[2] J. Ross, *Crash Course: Nervous System.* Mosby, oCLC: 896191000.

[3] F. Bahner, E. K. Weiss, G. Birke, N. Maier, D. Schmitz, U. Rudolph, M. Frotscher, R. D. Traub, M. Both, and A. Draguhn, "Cellular correlate of assembly formation in oscillating hippocampal networks in vitro," vol. 108, no. 35, pp. E607–E616. [Online]. Available: http://www.pnas.org/cgi/doi/10.1073/pnas.1103546108

[4] G. Gouy, "On the Formation of Electrical Charges at the Surface of an Electrolyte," vol. 9, pp. 457–469.

[5] E. Hückel and P. Debye, "The theory of electrolytes: I. lowering of freezing point and related phenomena," vol. 24, pp. 185–206.

[6] D. Sterratt, B. Graham, A. Gillies, and D. Willshaw. Principles of Computational Modelling in Neuroscience by David Sterratt. [Online]. Available: /core/books/principles-of-computational-modelling-in-neuroscience/9E360450B94A386051003D763A287CF0

[7] B. Hille, *Ion Channels of Excitable Membranes*, 3rd ed. Sinauer, oCLC: 248289849.

[8] A. L. Hodgkin and A. F. Huxley, "The dual effect of membrane potential on sodium conductance in the giant axon of *Loligo*," vol. 116, no. 4, pp. 497–506. [Online]. Available: https://onlinelibrary.wiley.com/doi/abs/10.1113/jphysiol.1952.sp004719

[9] ——, "The components of membrane conductance in the giant axon of *Loligo*," vol. 116, no. 4, pp. 473–496. [Online]. Available: https://onlinelibrary.wiley.com/doi/abs/10.1113/jphysiol.1952.sp004718

[10] J. C. Skou, "The influence of some cations on an adenosine triphosphatase from peripheral nerves," vol. 23, pp. 394–401. [Online]. Available: https://linkinghub.elsevier.com/retrieve/pii/0006300257903438

[11] P. Dayan and L. F. Abbott, *Theoretical Neuroscience: Computational and Mathematical Modeling of Neural Systems*, ser. Computational Neuroscience. Massachusetts Institute of Technology Press.

[12] A. L. Hodgkin and A. F. Huxley, "A quantitative description of membrane current and its application to conduction and excitation in nerve," vol. 117, no. 4, pp. 500–544. [Online]. Available: https://onlinelibrary.wiley.com/doi/abs/10.1113/jphysiol.1952.sp004764

[13] A. L. Hodgkin, A. F. Huxley, and B. Katz, "Measurement of current-voltage relations in the membrane of the giant axon of *Loligo*," vol. 116, no. 4, pp. 424–448. [Online]. Available: https://onlinelibrary.wiley.com/doi/abs/10.1113/jphysiol.1952.sp004716

[14] A. Mauro, "Anomalous Impedance, A Phenomenological Property of Time-Variant Resistance: An Analytic Review," vol. 1, no. 4, pp. 353–372. [Online]. Available: http://www.sciencedirect.com/science/article/pii/S000634956186894X

[15] G. Massobrio, S. Martinoia, and P. Massobrio, "Equivalent Circuit of the Neuro-Electronic Junction for Signal Recordings From Planar and Engulfed Micro-Nano-Electrodes," vol. 12, no. 1, pp. 3–12. [Online]. Available: http://ieeexplore.ieee.org/document/8058481/

[16] C. Anastassiou, G. Buzsáki, and C. Koch, *Biophysics of Extracellular Spikes*. CRC Press, pp. 15–36. [Online]. Available: http://www.crcnetbase.com/doi/10.1201/b14756-4

[17] G. Buzsáki, C. A. Anastassiou, and C. Koch, "The origin of extracellular fields and currents–EEG, ECoG, LFP and spikes," vol. 13, no. 6, pp. 407–420.

[18] M. W. Reimann, C. A. Anastassiou, R. Perin, S. L. Hill, H. Markram, and C. Koch, "A biophysically detailed model of neocortical local field potentials predicts the critical role of active membrane currents," vol. 79, no. 2, pp. 375–390.

[19] P. L. Nunez and R. Srinivasan, *Electric Fields of the Brain: The Neurophysics of EEG*, second edition ed. Oxford University Press.

[20] D. A. Henze, Z. Borhegyi, J. Csicsvari, A. Mamiya, K. D. Harris, and G. Buzsáki, "Intracellular Features Predicted by Extracellular Recordings in the Hippocampus In Vivo," vol. 84, no. 1, pp. 390–400. [Online]. Available: http://www.physiology.org/doi/10.1152/jn.2000.84.1.390

[21] A. Belitski, A. Gretton, C. Magri, Y. Murayama, M. A. Montemurro, N. K. Logothetis, and S. Panzeri, "Low-frequency local field potentials and spikes in primary visual cortex convey independent visual information," vol. 28, no. 22, pp. 5696–5709.

[22] R. Quian Quiroga and S. Panzeri, "Extracting information from neuronal populations: Information theory and decoding approaches," vol. 10, no. 3, pp. 173–185.

[23] B. Sakmann and E. Neher, "Patch clamp techniques for studying ionic channels in excitable membranes," vol. 46, pp. 455–472.

[24] M. E. Spira and A. Hai, "Multi-electrode array technologies for neuroscience and cardiology," vol. 8, no. 2, pp. 83–94. [Online]. Available: http://www.nature.com/articles/nnano.2012.265

[25] R. Horn and A. Marty, "Muscarinic activation of ionic currents measured by a new whole-cell recording method," vol. 92, no. 2, pp. 145–159.

[26] M. E. Spira, S.-H. Huang, N. Shmoel, and H. Erez, "Multisite Intracellular Recordings by MEA," in *In Vitro Neuronal Networks*, M. Chiappalone, V. Pasquale, and M. Frega, Eds. Springer International Publishing, vol. 22, pp. 125–153. [Online]. Available: http://link.springer.com/10.1007/978-3-030-11135-9_5

[27] N. Fertig, R. H. Blick, and J. C. Behrends, "Whole Cell Patch Clamp Recording Performed on a Planar Glass Chip," vol. 82, no. 6, pp. 3056–3062. [Online]. Available: https://linkinghub.elsevier.com/retrieve/pii/S0006349502756464

[28] B. Tian, T. Cohen-Karni, Q. Qing, X. Duan, P. Xie, and C. Lieber, "Three-Dimensional, Flexible Nanoscale Field-Effect Transistors as Localized Bioprobes," vol. 329, pp. 830–4.

[29] M. Dipalo, H. Amin, L. Lovato, F. Moia, V. Caprettini, G. C. Messina, F. Tantussi, L. Berdondini, and F. De Angelis, "Intracellular and Extracellular Recording of Spontaneous Action Potentials in Mammalian Neurons and Cardiac Cells with 3D Plasmonic Nanoelectrodes," vol. 17, no. 6, pp. 3932–3939. [Online]. Available: http://pubs.acs.org/doi/10.1021/acs.nanolett.7b01523

[30] Z. C. Lin, C. Xie, Y. Osakada, Y. Cui, and B. Cui, "Iridium oxide nanotube electrodes for sensitive and prolonged intracellular measurement of action potentials," vol. 5, no. 1, p. 3206. [Online]. Available: http://www.nature.com/articles/ncomms4206

[31] J. Abbott, T. Ye, D. Ham, and H. Park, "Optimizing Nanoelectrode Arrays for Scalable Intracellular Electrophysiology," vol. 51, no. 3, pp. 600–608.

[32] M. E. J. Obien, K. Deligkaris, T. Bullmann, D. J. Bakkum, and U. Frey, "Revealing neuronal function through microelectrode array recordings," vol. 8. [Online]. Available: http://journal.frontiersin.org/article/10.3389/fnins.2014.00423/abstract

[33] F. Franke, D. Jäckel, J. Dragas, J. Müller, M. Radivojevic, D. Bakkum, and A. Hierlemann, "High-density microelectrode array recordings and real-time spike sorting for closed-loop experiments: An emerging technology to study neural plasticity," vol. 6. [Online]. Available: http://journal.frontiersin.org/article/10.3389/fncir.2012.00105/abstract

[34] K. Warwick, "Neuroengineering and neuroprosthetics," vol. 2, p. 239821281881749.

[35] D. Decker, R. Hempelmann, H. Natter, M. Pirrung, H. Rabe, K. H. Schäfer, and M. Saumer, "3D Nanostructured Multielectrode Arrays: Fabrication, Electrochemical Characterization, and Evaluation of Cell-Electrode Adhesion," vol. 4, no. 2, p. 1800436. [Online]. Available: http://doi.wiley.com/10.1002/admt.201800436

[36] J. C. Mateus, C. D. F. Lopes, M. Cerquido, L. Leitão, D. Leitão, S. Cardoso, J. Ventura, and P. Aguiar, "Improved *in vitro* electrophysiology using 3D-structured microelectrode arrays with a micro-mushrooms islets

architecture capable of promoting topotaxis," vol. 16, no. 3, p. 036012. [Online]. Available: http://stacks.iop.org/1741-2552/16/i=3/a=036012?key=crossref.a1bcf8238ad3183f8ae8dc73fac9089a

[37] A. Blau, "Cell adhesion promotion strategies for signal transduction enhancement in microelectrode array in vitro electrophysiology: An introductory overview and critical discussion," vol. 18, no. 5, pp. 481–492. [Online]. Available: https://linkinghub.elsevier.com/retrieve/pii/S1359029413000976

[38] M. E. Spira, D. Kamber, A. Dormann, A. Cohen, C. Bartic, G. Borghs, J. Langedijk, S. Yitzchaik, K. Shabthai, and J. Shappir, "Improved Neuronal Adhesion to the Surface of Electronic Device by Engulfment of Protruding Micro-Nails Fabricated on the Chip Surface," in *TRANSDUCERS 2007 - 2007 International Solid-State Sensors, Actuators and Microsystems Conference*. IEEE, pp. 1247–1250. [Online]. Available: http://ieeexplore.ieee.org/document/4300363/

[39] M. E. Spira, N. Shmoel, S.-H. M. Huang, and H. Erez, "Multisite Attenuated Intracellular Recordings by Extracellular Multielectrode Arrays, a Perspective," vol. 12, p. 212. [Online]. Available: http://journal.frontiersin.org/article/10.3389/fnins.2018.00212/full

[40] S. M. Ojovan, N. Rabieh, N. Shmoel, H. Erez, E. Maydan, A. Cohen, and M. E. Spira, "A feasibility study of multi-site,intracellular recordings from mammalian neurons by extracellular gold mushroom-shaped microelectrodes," vol. 5, no. 1, p. 14100. [Online]. Available: http://www.nature.com/articles/srep14100

[41] J. Abbott, T. Ye, L. Qin, M. Jorgolli, R. S. Gertner, D. Ham, and H. Park, "CMOS nanoelectrode array for all-electrical intracellular electrophysiological imaging," vol. 12, no. 5, pp. 460–466. [Online]. Available: http://www.nature.com/articles/nnano.2017.3

[42] A. Hai, A. Dormann, J. Shappir, S. Yitzchaik, C. Bartic, G. Borghs, J. P. M. Langedijk, and M. E. Spira, "Spine-shaped gold protrusions improve the adherence and electrical coupling of neurons with the surface of micro-electronic devices," vol. 6, no. 41, pp. 1153–1165. [Online]. Available: http://www.royalsocietypublishing.org/doi/10.1098/rsif.2009.0087

[43] M. Cerquido, M. Proenca, C. Dias, D. Leitao, S. Cardoso, P. Freitas, P. Aguiar, and J. Ventura, "Tailoring the cap's morphology of electrodeposited gold micro-mushrooms," vol. 445, pp. 512–518. [Online]. Available: https://linkinghub.elsevier.com/retrieve/pii/S0169433218308444

[44] S. Weidlich, K. J. Krause, J. Schnitker, B. Wolfrum, and A. Offenhäusser, "MEAs and 3D nanoelectrodes: Electrodeposition as tool for a precisely controlled nanofabrication," vol. 28, no. 9, p. 095302. [Online]. Available: http://stacks.iop.org/0957-4484/28/i=9/a=095302?key=crossref.970fa9655d266a5479ee0385d0d8f8b7

[45] U. Egert and T. Meyer, "Heart on a Chip — Extracellular Multielectrode Recordings from Cardiac Myocytes in Vitro," in *Practical Methods in Cardiovascular Research*, S. Dhein, F. W. Mohr, and M. Delmar, Eds. Springer-Verlag, pp. 432–453. [Online]. Available: http://link.springer.com/10.1007/3-540-26574-0_22

[46] F. Santoro, J. Schnitker, G. Panaitov, and A. Offenhäusser, "On Chip Guidance and Recording of Cardiomyocytes with 3D Mushroom-Shaped Electrodes," vol. 13, no. 11, pp. 5379–5384. [Online]. Available: http://pubs.acs.org/doi/10.1021/nl402901y

[47] S. Weydert, S. Girardin, X. Cui, S. Zürcher, T. Peter, R. Wirz, O. Sterner, F. Stauffer, M. J. Aebersold, S. Tanner, G. Thompson-Steckel, C. Forró, S. Tosatti, and J. Vörös, "A Versatile Protein and Cell Patterning Method Suitable for Long-Term Neural Cultures," vol. 35, no. 8, pp. 2966–2975. [Online]. Available: http://pubs.acs.org/doi/10.1021/acs.langmuir.8b03730

[48] G. Panaitov, S. Thiery, B. Hofmann, and A. Offenhäusser, "Fabrication of gold micro-spine structures for improvement of cell/device adhesion," vol. 88, no. 8, pp. 1840–1844. [Online]. Available: https://linkinghub.elsevier.com/retrieve/pii/S0167931710005629

[49] J. Tønnesen and U. V. Nägerl, "Dendritic Spines as Tunable Regulators of Synaptic Signals," vol. 7. [Online]. Available: http://journal.frontiersin.org/Article/10.3389/fpsyt.2016.00101/abstract

[50] A. Hai, J. Shappir, and M. E. Spira, "Long-Term, Multisite, Parallel, In-Cell Recording and Stimulation by an Array of Extracellular Microelectrodes," vol. 104,

no. 1, pp. 559–568. [Online]. Available: http://www.physiology.org/doi/10.1152/jn.00265.2010

[51] N. Shmoel, N. Rabieh, S. M. Ojovan, H. Erez, E. Maydan, and M. E. Spira, "Multisite electrophysiological recordings by self-assembled loose-patch-like junctions between cultured hippocampal neurons and mushroom-shaped microelectrodes," vol. 6, no. 1, p. 27110. [Online]. Available: http://www.nature.com/articles/srep27110

[52] W. M. Siu and R. S. C. Cobbold, "Basic properties of the electrolyte—SiO2—Si system: Physical and theoretical aspects," vol. 26, no. 11, pp. 1805–1815.

[53] P. Massobrio, G. Massobrio, and S. Martinoia, "Interfacing Cultured Neurons to Microtransducers Arrays: A Review of the Neuro-Electronic Junction Models," vol. 10. [Online]. Available: https://www.frontiersin.org/articles/10.3389/fnins.2016.00282/full

[54] A. Fendyur, N. Mazurski, J. Shappir, and M. E. Spira, "Formation of Essential Ultrastructural Interface between Cultured Hippocampal Cells and Gold Mushroom-Shaped MEA- Toward ?IN-CELL? Recordings from Vertebrate Neurons," vol. 4. [Online]. Available: http://journal.frontiersin.org/article/10.3389/fneng.2011.00014/abstract

[55] V. Thakore, P. Molnar, and J. J. Hickman, "An Optimization-Based Study of Equivalent Circuit Models for Representing Recordings at the Neuron–Electrode Interface," vol. 59, no. 8, pp. 2338–2347. [Online]. Available: http://ieeexplore.ieee.org/document/6214589/

[56] A. Hai, J. Shappir, and M. E. Spira, "In-cell recordings by extracellular microelectrodes," vol. 7, no. 3, pp. 200–202. [Online]. Available: http://www.nature.com/articles/nmeth.1420

[57] E. T. McAdams, J. Jossinet, R. Subramanian, and R. G. E. McCauley, "Characterization of gold electrodes in phosphate buffered saline solution by impedance and noise measurements for biological applications," vol. 1, pp. 4594–4597.

[58] V. M. Mirsky, M. Riepl, and O. S. Wolfbeis, "Capacitive monitoring of protein immobilization and antigen-antibody reactions on monomolecular alkylthiol films on gold electrodes," vol. 12, no. 9-10, pp. 977–989.

[59] A. Cohen, J. Shappir, S. Yitzchaik, and M. E. Spira, "Reversible transition of extracellular field potential recordings to intracellular recordings of action potentials generated by neurons grown on transistors," vol. 23, no. 6, pp. 811–819.

[60] A. Hai, D. Kamber, G. Malkinson, H. Erez, N. Mazurski, J. Shappir, and M. E. Spira, "Changing gears from chemical adhesion of cells to flat substrata toward engulfment of micro-protrusions by active mechanisms," vol. 6, no. 6, p. 066009. [Online]. Available: http://stacks.iop.org/1741-2552/6/i=6/a=066009?key=crossref.c7a81639db50fb4155f4ecd7d28abdf0

[61] H.-Y. Lou, W. Zhao, Y. Zeng, and B. Cui, "The Role of Membrane Curvature in Nanoscale Topography-Induced Intracellular Signaling," vol. 51, no. 5, pp. 1046–1053. [Online]. Available: http://pubs.acs.org/doi/10.1021/acs.accounts.7b00594

[62] C. Miller, "Ionic channels of excitable membranes. Second edition: By Bertil Hille. Sunderland, Massachusetts: Sinauer. (1991). 607 pp. $46.95," vol. 69, no. 4, p. 579. [Online]. Available: https://www.cell.com/cell/abstract/0092-8674(92)90220-7

[63] W. Zhao, L. Hanson, H.-Y. Lou, M. Akamatsu, P. D. Chowdary, F. Santoro, J. R. Marks, A. Grassart, D. G. Drubin, Y. Cui, and B. Cui, "Nanoscale manipulation of membrane curvature for probing endocytosis in live cells," vol. 12, no. 8, pp. 750–756. [Online]. Available: https://www.nature.com/articles/nnano.2017.98

[64] K. Weir, O. Blanquie, W. Kilb, H. J. Luhmann, and A. Sinning, "Comparison of spike parameters from optically identified GABAergic and glutamatergic neurons in sparse cortical cultures," vol. 8. [Online]. Available: http://journal.frontiersin.org/article/10.3389/fncel.2014.00460/abstract

[65] R. P. Feynman, "There's Plenty of Room at the Bottom: An Invitation to Enter a New Field of Physics," in *Handbook of Nanoscience, Engineering, and Technology*, W. A. Goddard, D. Brenner, S. E. Lyshevski, and G. J. Iafrate, Eds. CRC Press, pp. 3–12. [Online]. Available: http://resolver.caltech.edu/CaltechAUTHORS:20141219-151712733

[66] R. G. Harrison, M. J. Greenman, F. P. Mall, and C. M. Jackson, "Observations of the living developing nerve fiber," vol. 1, no. 5, pp. 116–128. [Online]. Available: http://doi.wiley.com/10.1002/ar.1090010503

[67] S. C. Terry, J. H. Jerman, and J. J. Angell. A gas chromatographic air analyzer fabricated on a silicon wafer. [Online]. Available: /paper/A-gas-chromatographic-air-analyzer-fabricated-on-a-Terry-Jerman/a0b5b05ba6925f4f8c3898a646fa5999bf89fe09

[68] G. M. Whitesides, "The origins and the future of microfluidics," vol. 442, no. 7101, pp. 368–373. [Online]. Available: http://www.nature.com/articles/nature05058

[69] "Microfluidics for Biological Applications." [Online]. Available: https://www.springer.com/gp/book/9780387094793

[70] B. Xiong, K. Ren, Y. Shu, Y. Chen, B. Shen, and H. Wu, "Recent developments in microfluidics for cell studies," vol. 26, no. 31, pp. 5525–5532.

[71] A. Folch and M. Toner, "Microengineering of cellular interactions," vol. 2, pp. 227–256.

[72] D. B. Weibel, W. R. DiLuzio, and G. M. Whitesides, "Microfabrication meets microbiology," vol. 5, no. 3, pp. 209–218. [Online]. Available: https://www.nature.com/articles/nrmicro1616

[73] J. Friend and L. Yeo, "Fabrication of microfluidic devices using polydimethylsiloxane," vol. 4, no. 2, p. 026502. [Online]. Available: http://aip.scitation.org/doi/10.1063/1.3259624

[74] G. M. Walker, H. C. Zeringue, and D. J. Beebe, "Microenvironment design considerations for cellular scale studies," vol. 4, no. 2, p. 91. [Online]. Available: http://xlink.rsc.org/?DOI=b311214d

[75] J. Gordon, S. Amini, and M. K. White, "General overview of neuronal cell culture," vol. 1078, pp. 1–8.

[76] A. D. Jadhav, L. Wei, and P. Shi, "Compartmentalized Platforms for Neuro-Pharmacological Research," vol. 14, no. 1, pp. 72–86.

[77] A. M. Taylor, S. W. Rhee, C. H. Tu, D. H. Cribbs, C. W. Cotman, and N. L. Jeon, "Microfluidic Multicompartment Device for Neuroscience Research," vol. 19, no. 5, pp. 1551–1556. [Online]. Available: https://doi.org/10.1021/la026417v

[78] J. W. Park, B. Vahidi, A. M. Taylor, S. W. Rhee, and N. L. Jeon, "Microfluidic culture platform for neuroscience research," vol. 1, no. 4, pp. 2128–2136.

[79] J. J. FitzGerald*, S. P. Lacour, S. B. McMahon, and J. W. Fawcett, "Microchannel Electrodes for Recording and Stimulation: In Vitro Evaluation," vol. 56, no. 5, pp. 1524–1534.

[80] J. FitzGerald, S. Lacour, S. McMahon, and J. Fawcett, "Microchannels as Axonal Amplifiers," vol. 55, no. 3, pp. 1136–1146. [Online]. Available: http://ieeexplore.ieee.org/document/4360145/

[81] L. Wang, M. Riss, J. Buitrago, and E. Claverol-Tinturé, "Biophysics of microchannel-enabled neuron-electrode interfaces," vol. 9, p. 026010.

[82] L. Pan, S. Alagapan, E. Franca, T. DeMarse, G. J. Brewer, and B. C. Wheeler, "Large extracellular spikes recordable from axons in microtunnels," vol. 22, no. 3, pp. 453–459.

[83] R. Habibey, S. Latifi, H. Mousavi, M. Pesce, E. Arab-Tehrany, and A. Blau, "A multielectrode array microchannel platform reveals both transient and slow changes in axonal conduction velocity," vol. 7, no. 1, p. 8558. [Online]. Available: http://www.nature.com/articles/s41598-017-09033-3

[84] M. K. Lewandowska, M. Radivojević, D. Jäckel, J. Müller, and A. R. Hierlemann, "Cortical Axons, Isolated in Channels, Display Activity-Dependent Signal Modulation as a Result of Targeted Stimulation," vol. 10. [Online]. Available: http://journal.frontiersin.org/Article/10.3389/fnins.2016.00083/abstract

[85] K. Shimba, K. Sakai, T. Isomura, K. Kotani, and Y. Jimbo, "Axonal conduction slowing induced by spontaneous bursting activity in cortical neurons cultured in a microtunnel device," vol. 7, no. 1, pp. 64–72. [Online]. Available: https://academic.oup.com/ib/article/7/1/64-72/5198275

[86] N. Hong, S. Joo, and Y. Nam, "Characterization of Axonal Spikes in Cultured Neuronal Networks Using Microelectrode Arrays and Microchannel Devices," vol. 64, no. 2, pp. 492–498.

[87] O. Sporns and R. Kötter, "Motifs in Brain Networks," vol. 2, no. 11, p. e369. [Online]. Available: https://journals.plos.org/plosbiology/article?id=10.1371/journal.pbio.0020369

[88] C. Forró, G. Thompson-Steckel, S. Weaver, S. Weydert, S. Ihle, H. Dermutz, M. J. Aebersold, R. Pilz, L. Demkó, and J. Vörös, "Modular microstructure design to build neuronal networks of defined functional connectivity," vol. 122, pp. 75–87. [Online]. Available: https://linkinghub.elsevier.com/retrieve/pii/S0956566318306845

[89] W. Dauer and S. Przedborski, "Parkinson's Disease," vol. 39, no. 6, pp. 889–909. [Online]. Available: https://linkinghub.elsevier.com/retrieve/pii/S0896627303005683

[90] K. Zhang, Y. Osakada, M. Vrljic, L. Chen, H. V. Mudrakola, and B. Cui, "Single-molecule imaging of NGF axonal transport in microfluidic devices," vol. 10, no. 19, p. 2566. [Online]. Available: http://xlink.rsc.org/?DOI=c003385e

[91] M. S. Cohen, C. B. Orth, H. J. Kim, N. L. Jeon, and S. R. Jaffrey, "Neurotrophin-mediated dendrite-to-nucleus signaling revealed by microfluidic compartmentalization of dendrites," vol. 108, no. 27, pp. 11 246–11 251. [Online]. Available: http://www.pnas.org/cgi/doi/10.1073/pnas.1012401108

[92] W. Xie, K. Zhang, and B. Cui, "Functional characterization and axonal transport of quantum dot labeled BDNF," vol. 4, no. 8, p. 953. [Online]. Available: https://academic.oup.com/ib/article/4/8/953-960/5204457

[93] A. Virlogeux, E. Moutaux, W. Christaller, A. Genoux, J. Bruyère, E. Fino, B. Charlot, M. Cazorla, and F. Saudou, "Reconstituting Corticostriatal Network on-a-Chip Reveals the Contribution of the Presynaptic Compartment to Huntington's Disease," vol. 22, no. 1, pp. 110–122.

[94] X. Zhao, X.-Q. Chen, E. Han, Y. Hu, P. Paik, Z. Ding, J. Overman, A. L. Lau, S. H. Shahmoradian, W. Chiu, L. M. Thompson, C. Wu, and W. C. Mobley, "TRiC subunits enhance BDNF axonal transport and rescue striatal atrophy in Huntington's disease," vol. 113, no. 38, pp. E5655–5664.

[95] L. Li, L. Ren, W. Liu, J.-C. Wang, Y. Wang, Q. Tu, J. Xu, R. Liu, Y. Zhang, M.-S. Yuan, T. Li, and J. Wang, "Spatiotemporally Controlled and Multifactor Involved Assay of Neuronal Compartment Regeneration after Chemical Injury in

an Integrated Microfluidics," vol. 84, no. 15, pp. 6444–6453. [Online]. Available: http://pubs.acs.org/doi/10.1021/ac3013708

[96] Y.-t. Kim, K. Karthikeyan, S. Chirvi, and D. P. Davé, "Neuro-optical microfluidic platform to study injury and regeneration of single axons," vol. 9, no. 17, p. 2576. [Online]. Available: http://xlink.rsc.org/?DOI=b903720a

[97] K. A. Ludwig, J. D. Uram, J. Yang, D. C. Martin, and D. R. Kipke, "Chronic neural recordings using silicon microelectrode arrays electrochemically deposited with a poly(3,4-ethylenedioxythiophene) (PEDOT) film," vol. 3, no. 1, pp. 59–70. [Online]. Available: http://stacks.iop.org/1741-2552/3/i=1/a=007?key=crossref.594ccd20aeae6f412cfea06fab310388

[98] S. M. Wellman, J. R. Eles, K. A. Ludwig, J. P. Seymour, N. J. Michelson, W. E. McFadden, A. L. Vazquez, and T. D. Y. Kozai, "A Materials Roadmap to Functional Neural Interface Design," vol. 28, no. 12, p. 1701269. [Online]. Available: http://doi.wiley.com/10.1002/adfm.201701269

[99] P. C. Hütter, A. Fian, K. Gatterer, and B. Stadlober, "Efficiency of the Switching Process in Organic Electrochemical Transistors," vol. 8, no. 22, pp. 14 071–14 076. [Online]. Available: https://pubs.acs.org/doi/10.1021/acsami.6b02698

[100] M. Geoghegan and G. Hadziioannou, *Polymer Electronics*, 1st ed., ser. Oxford Master Series in Condensed Matter Physics. Oxford Univ. Press, no. 22, oCLC: 855552030.

[101] A. M. Nardes, R. A. J. Janssen, and M. Kemerink, "A Morphological Model for the Solvent-Enhanced Conductivity of PEDOT:PSS Thin Films," vol. 18, no. 6, pp. 865–871. [Online]. Available: https://onlinelibrary.wiley.com/doi/abs/10.1002/adfm.200700796

[102] D. Han, G. Yang, J. Song, L. Niu, and A. Ivaska, "Morphology of electrodeposited poly(3,4-ethylenedioxythiophene)/poly(4-styrene sulfonate) films," vol. 602, no. 1, pp. 24–28. [Online]. Available: https://linkinghub.elsevier.com/retrieve/pii/S0022072806006759

[103] H. Bartsch, R. Peipmann, M. Klett, D. Brauer, A. Schober, and J. Müller, "PEDOT Coated Thick Film Electrodes for In Situ Detection of Cell Adhesion in Cell Cultures," vol. 8, no. 4, p. 105. [Online]. Available: http://www.mdpi.com/2079-6374/8/4/105

[104] Z. Aqrawe, J. Montgomery, J. Travas-Sejdic, and D. Svirskis, "Conducting polymers for neuronal microelectrode array recording and stimulation," vol. 257, pp. 753–765. [Online]. Available: https://linkinghub.elsevier.com/retrieve/pii/S0925400517321548

[105] X. Cui and D. C. Martin, "Fuzzy gold electrodes for lowering impedance and improving adhesion with electrodeposited conducting polymer films," vol. 103, no. 3, pp. 384–394. [Online]. Available: http://www.sciencedirect.com/science/article/pii/S0924424702004272

[106] J. Rivnay, P. Leleux, M. Ferro, M. Sessolo, A. Williamson, D. A. Koutsouras, D. Khodagholy, M. Ramuz, X. Strakosas, R. M. Owens, C. Benar, J.-M. Badier, C. Bernard, and G. G. Malliaras, "High-performance transistors for bioelectronics through tuning of channel thickness," vol. 1, no. 4, p. e1400251.

[107] Z. Aqrawe, B. Wright, N. Patel, Y. Vyas, J. Malmstrom, J. M. Montgomery, D. Williams, J. Travas-Sejdic, and D. Svirskis, "The influence of macropores on PEDOT/PSS microelectrode coatings for neuronal recording and stimulation," vol. 281, pp. 549–560. [Online]. Available: https://linkinghub.elsevier.com/retrieve/pii/S092540051831877X

[108] H. S. Mandal, G. L. Knaack, H. Charkhkar, D. G. McHail, J. S. Kastee, T. C. Dumas, N. Peixoto, J. F. Rubinson, and J. J. Pancrazio, "Improving the performance of poly(3,4-ethylenedioxythiophene) for brain–machine interface applications," vol. 10, no. 6, pp. 2446–2454. [Online]. Available: https://linkinghub.elsevier.com/retrieve/pii/S1742706114000816

[109] A. Mata, A. J. Fleischman, and S. Roy, "Fabrication of multi-layer SU-8 microstructures," vol. 16, no. 2, pp. 276–284. [Online]. Available: http://stacks.iop.org/0960-1317/16/i=2/a=012?key=crossref.181d3eebbc9f3f90b46a285db2037b36

[110] B. Bohl, R. Steger, R. Zengerle, and P. Koltay, "Multi-layer SU-8 lift-off technology for microfluidic devices," vol. 15, no. 6, pp. 1125–1130. [Online]. Available: http://stacks.iop.org/0960-1317/15/i=6/a=002?key=crossref.904e2b32fad4d77ba8a80ece5164bad3

[111] A. D. Jadhav, L. Wei, and P. Shi, "Compartmentalized Platforms for Neuro-Pharmacological Research," vol. 14, no. 1, pp. 72–86. [Online]. Available: http://www.eurekaselect.com/openurl/content.php?genre=article&issn=1570-159X&volume=14&issue=1&spage=72

[112] M. C. C. Cerquido, "Fabrication of biocompatible gold mushrrooms-shaped microelectrodes for the recording of neuronal signals." [Online]. Available: https://repositorio-aberto.up.pt/handle/10216/101719

[113] I. Kayaku Advanced Materials, "SU-8 3005 Datasheet." [Online]. Available: https://kayakuam.com/wp-content/uploads/2019/09/SU-8-3000-Data-Sheet.pdf

[114] ——, "SU-8 2100 Datasheet." [Online]. Available: https://kayakuam.com/wp-content/uploads/2019/09/SU-82000DataSheet2100and2150Ver5.pdf

[115] P. Chandrasekhar, *Conducting Polymers, Fundamentals and Applications: A Practical Approach.* Springer, oCLC: 1066185006. [Online]. Available: http://public.eblib.com/choice/publicfullrecord.aspx?p=5587555

[116] J. Heinze, A. Rasche, M. Pagels, and B. Geschke, "On the origin of the so-called nucleation loop during electropolymerization of conducting polymers," vol. 111, no. 5, pp. 989–997.

[117] H. Zhu, M. Li, D. Wang, S. Zhou, and C. Peng, "Interfacial Synthesis of Free-Standing Asymmetrical PPY-PEDOT Copolymer Film with 3D Network Structure for Supercapacitors," vol. 164, no. 9, pp. A1820–A1825. [Online]. Available: http://jes.ecsdl.org/lookup/doi/10.1149/2.1401707jes

[118] N. Sakmeche, S. Aeiyach, J.-J. Aaron, M. Jouini, J. C. Lacroix, and P.-C. Lacaze, "Improvement of the Electrosynthesis and Physicochemical Properties of Poly(3,4-ethylenedioxythiophene) Using a Sodium Dodecyl Sulfate Micellar Aqueous Medium," vol. 15, no. 7, pp. 2566–2574. [Online]. Available: https://pubs.acs.org/doi/10.1021/la980909j

[119] Y.-Y. Lee, G. M. Choi, S.-M. Lim, J.-Y. Cho, I.-S. Choi, K. T. Nam, and Y.-C. Joo, "Growth Mechanism of Strain-Dependent Morphological Change in PEDOT:PSS Films," vol. 6, no. 1, p. 25332. [Online]. Available: http://www.nature.com/articles/srep25332

[120] "Frontmatter," in *Electrochemical Phase Formation and Growth*, E. Budevski, G. Staikov, and W. J. Lorenz, Eds. Wiley-VCH Verlag GmbH, pp. I–XI. [Online]. Available: http://doi.wiley.com/10.1002/9783527614936.fmatter

[121] W. Gao, S. Sattayasamitsathit, A. Uygun, A. Pei, A. Ponedal, and J. Wang, "Polymer-based tubular microbots: Role of composition and preparation," vol. 4, no. 7, p. 2447. [Online]. Available: http://xlink.rsc.org/?DOI=c2nr30138e

[122] V. Castagnola, C. Bayon, E. Descamps, and C. Bergaud, "Morphology and conductivity of PEDOT layers produced by different electrochemical routes," vol. 189, pp. 7–16. [Online]. Available: http://www.sciencedirect.com/science/article/pii/S0379677913006103

[123] B. X. E. Desbiolles, E. de Coulon, A. Bertsch, S. Rohr, and P. Renaud, "Intracellular Recording of Cardiomyocyte Action Potentials with Nanopatterned Volcano-Shaped Microelectrode Arrays," vol. 19, no. 9, pp. 6173–6181. [Online]. Available: https://doi.org/10.1021/acs.nanolett.9b02209

[124] S. Venkatraman, J. Hendricks, Z. A. King, A. J. Sereno, S. Richardson-Burns, D. Martin, and J. M. Carmena, "In Vitro and In Vivo Evaluation of PEDOT Microelectrodes for Neural Stimulation and Recording," vol. 19, no. 3, pp. 307–316. [Online]. Available: http://ieeexplore.ieee.org/document/5705581/

[125] M. R. Abidian, J. M. Corey, D. R. Kipke, and D. C. Martin, "Conducting-Polymer Nanotubes Improve Electrical Properties, Mechanical Adhesion, Neural Attachment, and Neurite Outgrowth of Neural Electrodes," vol. 6, no. 3, pp. 421–429. [Online]. Available: https://onlinelibrary.wiley.com/doi/abs/10.1002/smll.200901868

[126] N. Kurra, J. Park, and H. N. Alshareef, "A conducting polymer nucleation scheme for efficient solid-state supercapacitors on paper," vol. 2, no. 40, pp. 17 058–17 065. [Online]. Available: http://xlink.rsc.org/?DOI=C4TA03603D

[127] A. Abas, H. Sheng, Y. Ma, X. Zhang, Y. Wei, Q. Su, W. Lan, and E. Xie, "PEDOT:PSS coated CuO nanowire arrays grown on Cu foam for high-performance supercapacitor electrodes," vol. 30, no. 12, pp. 10 953–10 960. [Online]. Available: http://link.springer.com/10.1007/s10854-019-01469-9

[128] Y. Liu, B. Weng, J. M. Razal, Q. Xu, C. Zhao, Y. Hou, S. Seyedin, R. Jalili, G. G. Wallace, and J. Chen, "High-Performance Flexible All-Solid-State Supercapacitor from Large Free-Standing Graphene-PEDOT/PSS Films," vol. 5, no. 1, p. 17045. [Online]. Available: http://www.nature.com/articles/srep17045